Underwater Acoustic Propagation in the Philippine Sea: Intensity Fluctuations

Andrew W. White

A dissertation
submitted in partial fulfillment of the
requirements for the degree of

Doctor of Philosophy

University of Washington

2013

Reading Committee:

James A. Mercer, Chair

Rex K. Andrew

Ken C. Creager

John R. Booker

Randall J. LeVeque

Program Authorized to Offer Degree:
Earth and Space Sciences

University of Washington

Abstract

Underwater Acoustic Propagation in the Philippine Sea: Intensity Fluctuations

Andrew W. White

Chair of the Supervisory Committee:
Professor James A. Mercer
Department of Earth and Space Sciences

In the spring of 2009, broadband transmissions from a ship-suspended source with a 284 Hz center frequency were received on a moored and navigated vertical array of hydrophones over a range of 107 km in the Philippine Sea. During a 60-hour period over 19 000 transmissions were carried out. The observed wavefront arrival structure reveals four distinct purely refracted acoustic paths: one with a single upper turning point near 80 m depth, two with a pair of upper turning points at a depth of roughly 300 m, and one with three upper turning points at 420 m. Individual path intensity, defined as the absolute square of the center frequency Fourier component for that arrival, was estimated over the 60-hour duration and used to compute scintillation index and log-intensity variance. Monte Carlo parabolic equation simulations using internal-wave induced sound speed perturbations obeying the Garrett-Munk internal-wave energy spectrum were in agreement with measured data for the three deeper-turning paths but differed by as much as a factor of four for the near surface-interacting path. Estimates of the power spectral density and temporal autocorrelation function of intensity were attempted, but were complicated by gaps in the measured time-series. Deep fades in intensity were observed in the near surface-interacting path. Hypothesized causes for the deep fades were examined through further acoustic propagation modeling and analysis of various available oceanographic measurements.

TABLE OF CONTENTS

Page

Chapter 1

INTRODUCTION

Inhomogeneity of sound speed in the ocean medium is caused by variations in temperature, salinity, and pressure over a broad range of temporal and spatial scales. The variability in sound speed at a given location is generally small: only a few percent of the average value (Garrison, 2005). Sound speed in seawater increases with temperature, pressure, and salinity, and is more strongly a function of temperature and pressure than of salinity (Pickard and Emery, 1990). At mid-latitudes, the temperature decrease with depth is rapid near the surface, overwhelming the effect on the sound speed of approximately linearly-increasing pressure; at depths greater than about a kilometer, the temperature decrease is more gradual and the pressure effect dominates. The combination of these effects is responsible for the minimum in sound speed at around a kilometer in depth that is typical at mid-latitudes (Munk et al., 1995).

Dynamical variability in the ocean is ultimately a result of the influence of the sun, the earth, and the moon, and of the earth's rotation (Garrison, 2005). The sun provides energy inputs to the ocean through its gravitational effect and through heating the atmosphere and ocean by radiative flux. The moon's input is solely through the gravitational effect, and through the resulting tides. The rotation of Earth and differential heating from the sun are responsible for the circulation of the ocean. The atmosphere is heated more at the equator and mid-latitudes than at the poles (Apel, 1987), causing pressure differences and thus wind to blow across the ocean's surface. The associated wind stress probably accounts for most of the surface currents (Pond and Pickard, 1983); the rotation of the earth causes the water to flow in a direction slightly different to that of the wind. These wind-driven currents also interact with the land masses, resulting in gyre-scale circulations. Mesoscale motions dominate the ocean's circulation (Morrow and Le Traon, 2006). The energy input driving mesoscale motions is thought to be mostly derived from mean flow

instabilities (Stammer and Wunsch, 1999). Tides are motions of the water driven by gravitational forces; the resulting flow of water over bathymetric features displaces surfaces of constant density (isopycnals), which rebound, converting some of this tidal energy to internal tides (Egbert and Ray, 2000). Low-pressure areas from storms can excite motions on inertial timescales (e.g. Alford (2003)). Conversion of energy from tides, internal tides, inertial motions, and wind- or storm-driven currents contribute to the generation of internal waves—and although internal waves can obviously have local sources, in the context of this thesis they are modeled as a diffuse "background" of internal motions that pervade most of the world's oceans.

Some other types of variability in the ocean include regional differences in water properties and seasonal changes. Regional differences result in fronts when two water masses come into contact, or in changes in water properties at a given location when coherent mesoscale structures trap and transport parcels of distinct water masses past that location. Seasonal changes include, for example, heating or cooling of the upper few hundred meters of the ocean or increased evaporation or precipitation, causing the character of profiles of water properties to change, or for mixed layers up to hundreds of meters deep to form near the surface (Sutton et al., 1997). Another example of seasonal changes near polar regions is the presence or absence of sea-ice. Seasonal changes can have profound effects on acoustic propagation (Sutton et al., 1993): creating or eliminating acoustic paths, changing boundary conditions, and moving the positions of shadow (places or times that sound energy doesn't reach) and convergence (places that acoustic paths come together) zones.

Among fields of study that involve sound in the ocean, there exist two that are intimately related, but have quite different aims: acoustical oceanography and ocean acoustics. Acoustical oceanography aims to infer about the properties or processes of the ocean by using sound as a tool. An example of this is ocean acoustic tomography

(Munk et al., 1995), in which the travel time of sound following particular paths is inverted for the water's temperature or current velocities, e.g. Howe et al. (1987). Some more examples that fall under the guise of using sound as a tool (though not specifically under acoustical oceanography) in the ocean are the use of hydrophones to remotely detect and monitor rainfall at sea (Nystuen, 2001), monitoring marine-terminating glaciers (Pettit et al., 2012), and detection, tracking, and monitoring of marine mammals. The aim of ocean acoustics is to understand how the ocean's properties and processes affect the propagation of sound. As sound waves propagate through the water, fluctuations in their phase and intensity are induced by variability in the properties of the water and its motions. An understanding of the causes and nature of these fluctuations is at least helpful, if not essential, in all of the applications listed above, as well as for detection and tracking of man-made sources of sound, such as surface ships and submarines, for military or defense purposes. This thesis falls under the category of ocean acoustics.

The effects on the propagation of acoustic waves of the various ocean processes become important in different circumstances, due to the processes' ranges of temporal and spatial scales. The tides and internal tides have timescales as long as a month, as well as the diurnal, semidiurnal, and harmonic timescales (Zhao et al., 2012). Internal waves have frequencies from the inertial to the buoyancy frequency; the inertial frequency depends on latitude and the buoyancy frequency depends on the stratification. The inertial period is on the order of tens of hours and the buoyancy frequency is on the order of tens of minutes. Mesoscale has spatial scales of roughly 100 km and timescales of about 100 d—though maximum propagation speeds are typically only about $3\,\mathrm{km\,d^{-1}}$ (Fu et al., 2010). The speed of sound in the ocean is approximately $1.5\,\mathrm{km\,s^{-1}}$ (Apel, 1987); the medium is thus essentially "frozen" as the acoustic waves pass through it. There are processes with faster timescales, such as molecular relax-

ation, that effectively cause attenuation of acoustic waves (Urick, 1975). Also a factor is whether a given acoustic path is purely-refracting (i.e. one that does not reflect from the surface or bottom), or surface- and/or bottom-reflecting. Surface-reflecting paths are affected variously, depending on acoustic frequency (wavelength), grazing angle, and surface roughness. The ocean's surface is perturbed by waves from small-scale capillary waves (wavelengths less than about 2 cm) up to the tides (a maximum scale of half the earth's circumference). Wind speed is the most important factor in determining the surface roughness and the prevalence and characteristics of near-surface bubble clouds. Surface roughness and bubble clouds cause scattering, refraction, and absorption of sound (Ainslie, 2010).

This thesis deals with low-frequency acoustic waves (frequencies less than 1 kHz) following wholly-refracted paths, and paths possibly grazing the surface at a maximum angle of only one, or a few degrees in the average smoothed sound-speed profile that was measured during the experiment. The duration and sampling rate (for pulsed signals, think of this as the frequency with which the acoustic waves interrogate the medium) of a hypothetical experiment, in addition to the range between source and receiver, will determine the processes that are important for the acoustic propagation. In the experiment discussed in this thesis, path lengths are about 100 km, sampling was every 7.2 s, and the duration was about 60 h. The mesoscales won't be expected to change much over this duration, but may be important in determining the gross sound-speed structure over the propagation range. Internal-tide timescales of diurnal length and shorter must be considered; these cause perturbations to the sound-speed structure on scales of up to around a couple hundred km horizontally (Zhao et al., 2012), and down to about 10 m wavelengths in the vertical (these are also the scales of internal waves: internal tides are actually internal waves). Internal waves are expected to provide most of the acoustic intensity fluctuations in this context.

Refraction in the horizontal directions is an important consideration in some problems in ocean acoustics, e.g. those involving ranges of megameters or propagation through mesoscale eddies, or any situation with sufficiently strong horizontal sound-speed gradients (Mercer and Booker, 1983). For the purposes of this introduction, it will suffice to consider only refraction in the vertical. If the sound speed is assumed to be homogeneous in the horizontal (or range) direction, it is referred to as "range-independent". Although a range-independent assumption is almost never thought to capture all of the features of the sound-speed field, it greatly simplifies many calculations and if appropriately chosen, is an excellent starting point for developing insight into the propagation of acoustic signals in a given region.

The shape of the typical mid-latitude vertical sound speed profile causes sound that is radiated at small angles to the horizontal to refract away from the shallow and deep parts of the ocean in a cyclical pattern (Munk et al., 1995). For a sound source that radiates omni-directionally, sound leaving that source at different angles to the horizontal propagates along distinct paths. A hydrophone located at a given depth and range may receive the radiated sound along multiple paths, at multiple times. In general, sound traveling along the different paths takes a different amount of time to traverse that path from source to receiver. This fact was discovered with the 1940's depth-charge experiments of Ewing and Worzel (1948). Low-frequency acoustic waves may travel through the ocean over large distances without suffering a large reduction in intensity: for example, sound from 200- and 300-pound charges deployed near Perth, Australia were detected on a hydrophone in Bermuda during an experiment in 1960 (Bryan et al., 1963). Depth-dependence of the arrival pattern was observed experimentally with the SLICE89 experiment (Duda et al., 1992), among others. An example prediction of paths for a sound source at the sound speed minimum (here at 1 km depth) is shown in figure 1.1. (Note that throughout this thesis the generic

terms “source” and “receiver” will refer to the idealized “acoustic transmitter” and “hydrophone” used in real-world experiments.)

The travel time and intensity of arrivals (as a couple of example observables of the acoustic field) along the different paths are to some extent predictable; a vertical sound speed profile obtained from a historical climatological database may be used as a deterministic input to an acoustic propagation model to get an idea of the arrival pattern to be expected for a given experimental location and source/receiver geometry. See figure 1.2 for an example of a predicted temporal arrival pattern at a vertical array of receivers. The extent to which the acoustic field is *not* predictable in a deterministic sense, very generally, is the topic of this thesis, and may be classified as wave propagation in random media. The practical inability to know the exact sound-speed field at all places and times (at least insomuch as the propagation is affected) is the reason that the problem is treated as being a stochastic one. The challenge goes from, “How can one, with the available equipment, measure the sound-speed field everywhere necessary throughout the duration of the experiment, and thereby predict in a deterministic sense, the acoustic field?”, and instead becomes, “What can one predict about the statistics of the acoustic field, given limited information about the sound-speed field?”.

The predictions in figures 1.1 and 1.2 were made using ray theory, which has an infinite-frequency approximation (Jensen, 1994). In this approximation, there is no prediction of the acoustic field near a ray, but only on the ray. There are ways to calculate the field near rays, but the speed of modern computers often allows use of more computationally-intensive full-wave methods, which calculate the acoustic field everywhere in the medium. Without a diffractive correction, ray theory would predict that there is a fifth arrival at the receiver at 2100 m depth in the example in figure 1.2—but not at 2300 m depth. A full-wave calculation would predict an arrival at

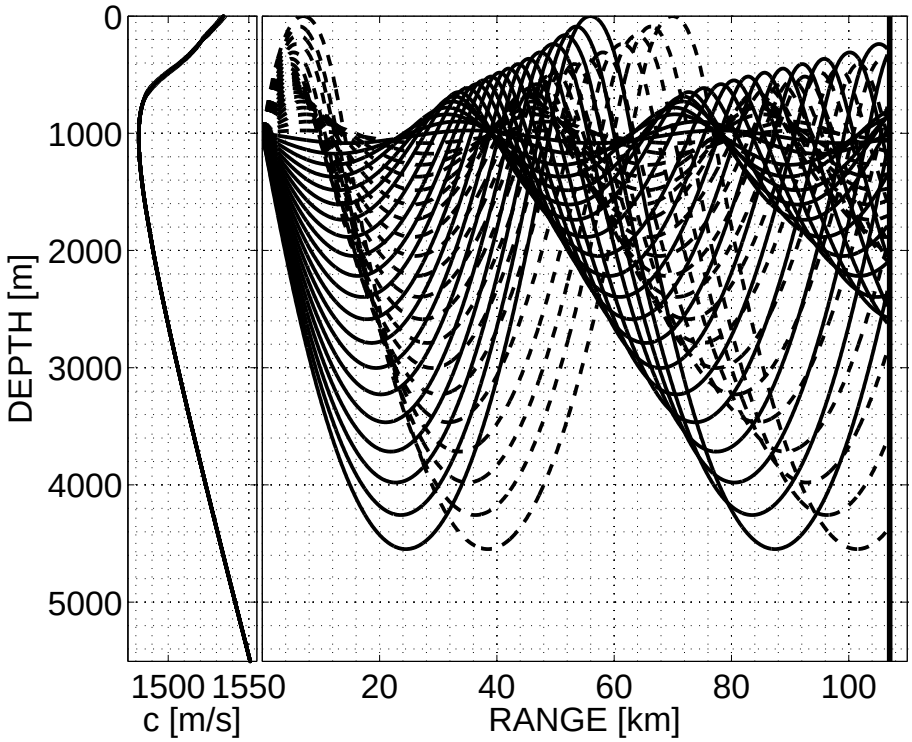

Figure 1.1: The left-hand plot in the figure shows an example sound speed profile from the Philippine Sea. The right-hand plot shows the predicted paths that sound leaving a source that is located at 1000 m depth would take for angles to the horizontal between $\pm 15^{\circ}$. Notice that the vertical axis is greatly exaggerated; the units in the vertical are the same as for the sound speed profile at left, m, while the horizontal units are km. Paths for sound leaving the source at positive (negative) grazing angles are plotted as solid (dashed) curves for clarity of presentation. The vertical line at 107 km represents the range from the source of an example vertical array of hydrophones. It is apparent that at a given range, particular paths will intersect the vertical array at particular depths. Paths which touch the ocean surface or bottom (about 5500 m depth) are omitted—and only a few paths between $\pm 15^{\circ}$ are shown for clarity. The nomenclature used to indicate acoustic paths throughout this thesis combines the direction $+/-$, above/below the horizontal, that the energy left the source, followed by the number of upper and lower turns before reaching the receiving array. As an example, the steepest downward-going path (solid curve) would be identified as ID-3 in the series of arrivals at a receiver at 2300 m depth.

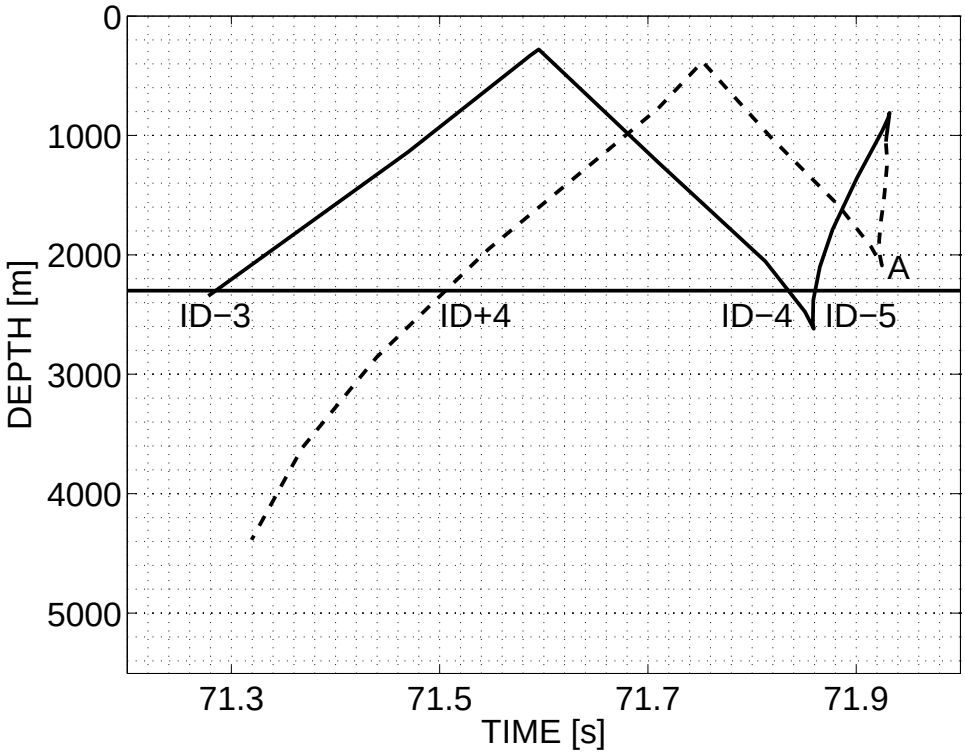

Figure 1.2: Shown here is a prediction of the pattern in time and depth (also known as a "timefront") at the range of the receiving array shown in figure 1.1, of acoustic arrivals along the paths that are also shown (with identical line-styles) in that figure. The horizontal black line represents a hypothetical receiver at 2300 m depth. If the source transmits a continuous signal, acoustic energy will arrive continuously at this receiver along four paths. If instead the source is impulsive, the energy will arrive at the times when branches of the timefront intersect the black line. The first arrival (with this geometry and profile) will be of steeper, downward-from-the-source energy, followed by upward-from-the-source energy, and finally by two more closely-spaced-in-time arrivals that left the source downward. The identifying labels for these paths are ID-3, ID+4, ID-4, and ID-5, respectively. Notice that a receiver at 2100 m depth would have one additional arrival (labeled 'A') that is not predicted to be received at 2300 m depth.

2300 m depth, but may predict it to be of such low intensity as to not be detectable. In this case, if a fifth arrival were to be detectable experimentally at 2300 m depth, it would be labeled a "shadow-zone arrival" (Dushaw, 1999). Shadow-zone arrivals have been detected on Navy SOSUS hydrophones and on vertical arrays of hydrophones in several experiments (Uffelen et al., 2009).

The concepts that are necessary to understand shadow-zone arrivals have been introduced above in the context of a ray model, since it provides an easy-to-visualize framework for propagation. An alternative picture may be drawn in the context of normal-mode theory (Porter and Reiss, 1984), in which the solution to the (Helmholtz, or single-frequency) wave equation is assumed to be separable, and to be a product of vertical and horizontal functions. The vertical solutions are normal modes, with a different set of modes for each acoustic frequency under consideration. The mode number gives the number of local maxima in depth and each mode has a different phase speed. Any particular portion in time of the timefront may be expressed as a sum over a subset of these modes. Deep shadow-zone arrivals would then be caused by scattering into higher modes (which have significant amplitude at very shallow and very deep depths) than those modes making up that part of the timefront.

Van Uffelen (2009) found that full-wave simulations of acoustic propagation through an ocean model consisting of a smooth sound-speed profile perturbed by internal-wave displacements of the sound-speed field predicted the penetration of energy into the shadow-zone for 500 km and 1000 km paths. It is not well-known at what ranges, and to what extent, penetration of acoustic energy into geometric shadow zones (Uffelen et al., 2010) should be expected for a given experimental geometry; e.g. is the effect cumulative? Most of the contribution to acoustic scattering is thought to occur at upper-turning-points (UTP) (Flatté et al., 1979), where the path is horizontal and therefore high correlations in the lateral inhomogeneity of sound speed (which

is greatest in the upper ocean) align with the direction of propagation, maximizing their effect. It is also unknown how intensity fluctuations develop with the number of turning points or depend on turning-point depth. At long range, acoustic paths pass through the upper ocean many times before reaching a receiving hydrophone; the physical mechanisms responsible for particular features of acoustic intensity fluctuations may be obscured by multiple scattering events.

Well-separated acoustic paths; e.g. paths that are coincident in the azimuthal direction, but with UTP at ranges further apart than a correlation length would not, in the ray-based understanding, "touch" the same internal-wave induced sound-speed perturbations—and therefore their fluctuations should not be correlated. Relating to this idea, there have been advances in the theoretical understanding: for example, it has been suggested that there exist "regions of influence" that describe where sound speed fluctuations will have an effect on acoustic energy following particular paths from source to receiver, e.g. travel-time sensitivity kernels (TSK) (Skarsoulis and Cornuelle, 2004) and differential regions of influence (DRI) (Spiesberger, 2006). In what is perhaps a confirmation of these ideas, Spiesberger (2011) observed correlation in acoustic phase between arrivals following different paths to the receiver over a 3709 km path.

Another observation of unexpected correlation was mentioned in Andrew et al. (2005), in which it was noted that intensity records that sampled every 4 h for a period of 24 h once every 4 d for paths of several megameters failed tests for randomness, unless the records were sub-sampled so as to insure an inter-sample spacing of 8 h or more. A long-time correlation pattern was suspected but not directly observable given the original gappy sampling protocol in that particular experiment. The intensity record for one of the acoustic paths in the experiment discussed in this thesis shows obvious temporal correlations over several hours, while the other paths do not.

The Applied Physics Laboratory of the University of Washington (APL-UW) conducted a pilot study/engineering test in the Philippine Sea during April and May of 2009 (PhilSea09), in preparation for a full experiment to be conducted the following year. The full experiment was to include a test of the application of ocean acoustic tomography to the Philippine Sea (Worcester et al., 2012). The purpose of both of the APL-UW efforts was to study scattering of acoustic signals in the Philippine Sea. The 107 km-range was chosen in 2009 so that acoustic paths with one or a few UTP could be studied. This data set provides measurements of acoustic paths that pass through the upper ocean once, twice, or three times. The same phase correlations seen in the 3709 km path should appear in these measurements, if the ideas about "regions of influence" are correct. It is unknown whether similar correlations in intensity between paths are to be expected.

Until recently, most of the low-frequency (< 1 kHz), long-range (> 500 km) acoustic propagation experiments have been conducted in the Central and Eastern Pacific Ocean. In comparison to the Philippine Sea, these previously studied parts of the Pacific are more oceanographically benign. One reason for choosing a benign region, in the case of some of these scattering experiments, is that they have been conducted jointly with tomographic experiments—and there are regimes in which it is suspected that some of the assumptions made in tomographic inversion become invalid e.g. Mercer and Booker (1983). Acoustic frequency (along with geometry) should determine, in general, the relative importance of spatial scales that influence acoustic fluctuations, thus potentially emphasizing different sources of sound-speed variability in the ocean. It follows that the character of the local oceanography may be an important consideration in understanding acoustic fluctuations.

Mesoscale variability in the Philippine Sea is much higher than in the Central and Eastern Pacific Ocean, as evident from plots of the variance of sea-surface height

(SSH) (Kobashi and Kawamura, 2001). Maps of SSH measurements obtained by satellite altimetry are available from the AVISO database (Aviso and support from Cnes, 2012) every 7 days. Figure 1.3 shows the SSH anomaly on April 29, 2009 (year-day 119) in the region of the experiment. More evidence of mesoscale eddies, and their effect on the sound-speed profile will be examined and presented in chapter 4. Alford et al. (2011) measured baroclinic energy, energy fluxes, and turbulent dissipation in the Luzon Strait, and found these quantities to be "among the strongest ever measured"; PhilSea09 was conducted approximately 510 km to the East of the Luzon Strait. The effects of these internal tides on the sound-speed profile and currents is evident in measurements that are presented in chapters 2 and 4.

The main purpose of the work presented here is not specifically to address the unknowns presented above, but rather to answer the following question: Will Monte-Carlo simulations involving only diffuse internal waves predict acoustic intensity fluctuations in the oceanographically energetic Philippine Sea? This thesis is organized into three chapters plus this introduction: the first chapter is a paper that was accepted by the Journal of the Acoustical Society of America, re-formatted for inclusion in this thesis; the second chapter consists of work intended for a second paper; and the third chapter explores several hypotheses for long-timescale deep fades in intensity that were observed in one of the acoustic paths of the PhilSea09 experiment. Each chapter contains a more focused introduction that is appropriate for the work discussed therein.

The Garrett-Munk (GM) spectrum (Munk, 1981) is an empirically-derived model for the diffuse internal waves. A simulator that produces realizations of range-depth (2D) snapshots of internal-wave vertical displacements (Henyey and Reynolds, 2013) is used in full-wave Monte Carlo propagation studies presented in this thesis. In chapter 2, 226 independent realizations of internal-wave vertical displacements are

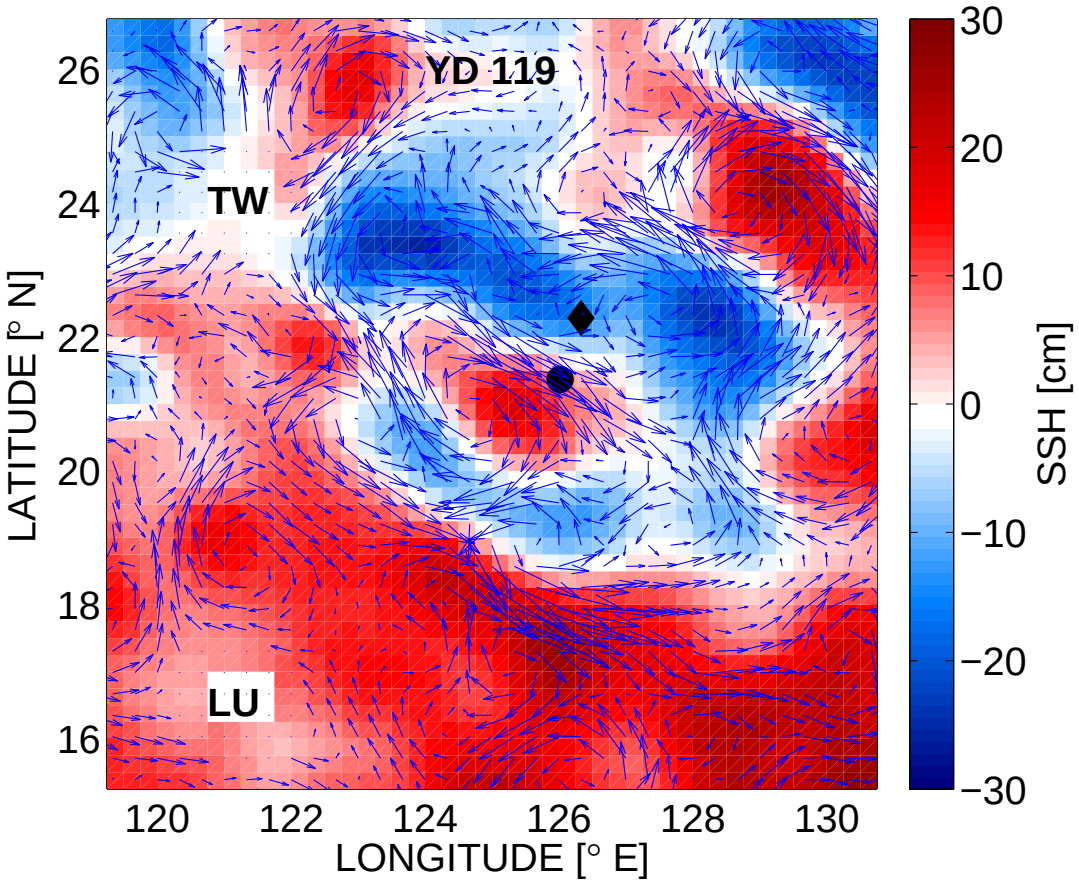

Figure 1.3: Sea surface height anomaly on 29 April 2009, from AVISO. The color scale is ±30 cm. Current vectors are computed assuming geostrophic balance. The black circle is the location of the moored vertical line-array of hydrophones during PhilSea09 and the black diamond is the location of the R/V *Melville* during acoustic transmissions from the ship-suspended transmitter discussed in this thesis. The labels "TW" and "LU" refer to the islands of Taiwan and Luzon, respectively.

used to perturb a range-independent sound-speed profile; broadband propagation of the acoustic field from a point-source through each of these 2D snapshots of perturbed sound-speed to 107 km range is computed. From the resulting timefronts, predictions of the time-independent statistics of acoustic intensity are made and compared with measurements from experiment. In chapter 3, an internal-wave displacement field is evolved in time at regular intervals. Propagation is calculated at each time-interval, yielding a time-evolving acoustic field from which time-series of intensity are created. Time-series of measured acoustic intensity are shown and compared qualitatively to the simulated time-series. Predictions of time-dependent measures of the acoustic intensity fluctuations, such as the power spectral density and temporal correlation function, are computed (the actual predictions are presented in appendix D). In chapter 4, environmental measurements that were taken during PhilSea09, along with environmental measurements from following years, and satellite measurements of SSH are explored in detail. Acoustic modeling involving an ocean with a surface mixed-layer using normal modes is discussed in relation to the observed deep fades. Finally, a simple plane-wave model of the local internal-tides is constructed and used to study horizontal and temporal correlations in internal-tide vertical displacements in the context of the experiment. Conclusions and a suggested direction for future work are given in chapter 5. A description of the internal-wave simulator used in this work appears in appendix C.

1.1 Preliminaries: Signals

1.1.1 Description of an m-sequence

Due to the importance and uniqueness of the actual acoustic signal that was used in the PhilSea09 pilot study/engineering test, a description is provided here. Details about how this signal is processed in order to realize the desired gain in signal to noise ratio (SNR) are provided in appendix A. A study of how Doppler effects caused by source or receiver motion can affect the achieved gain are presented in appendix B.

In performing an ocean acoustics experiment, we would prefer that the signal at the receiver be at a level at least 10 dB above the ambient noise in the frequency band of the transmitted signal. The attenuation coefficient for low-frequency sound propagating through seawater is small—about $0.008\,\mathrm{dB\,km^{-1}}$ at 284 Hz (estimated from a plot in Urick (1975)). This amounts to less than a decibel at 107 km. Spreading loss must also be taken into account, however, and one method to decrease the required source level is to increase the length (and therefore the energy) of the transmitted signal.

A continuous periodic signal called an "m-sequence", or Maximal Length Sequence (Birdsall and Metzger, 1986; Birdsall, 1995), was used for acoustic transmissions during PhilSea09. The term "m-sequence" will be used somewhat loosely here; the term will refer to a discrete digital sequence, but is also used to refer to the transmitted continuous analog signal that the sequence modulates. The discrete m-sequence is essentially a pseudo-random series of 1's and 0's. The series of 1's and 0's modulate the phase of a sine wave carrier signal of frequency f_0. At each transition from 1 to 0 or vice versa, the phase of the signal shifts forward or backward by the angle $\phi_0 = \arctan\sqrt{L}$, where L is the number of bits in the sequence. This is known as binary phase-shift keying, or BPSK.

The m-sequence (continuous form) that was used is uniquely described by a few parameters: the law, the number of bits, and the number of carrier cycles per digit. The law is the set of starting values of the linear-feedback shift registers that are used to construct the discrete sequence; the product of the number of cycles per digit and the number of bits (digits) in the m-sequence gives the duration of the sequence in cycles. The number of cycles per digit effectively maps the discrete digital sequence onto the continuous analog signal.

The signal for PhilSea09 consisted of 2046 cycles (1023 bits at 2 cycles per bit) of a $f_0 = 284.166\,666\,\text{Hz}$ carrier. This specific frequency was chosen in an attempt to maximize the output power of the transmitter while still maintaining an integral number of m-sequences per hour. Compression of this signal may be thought of as a replica-correlation that folds the energy of a single m-sequence into a bit of duration 7.7 ms (the reciprocal of the 130 Hz-bandwidth of the transmitted signal used in PhilSea09). This should result in a gain of $10 \log_{10}(1023) \approx 30\,\text{dB}$ in SNR.

Part I

INTENSITY FLUCTUATIONS

En el aire conmovido
mueve la luna sus brazos,
y enseña ...

Federico García Lorca

Romance De La Luna, Luna

Chapter 2

TIME-INDEPENDENT MEASURES

2.1 Introduction

Most of the contribution to acoustic scattering is thought to occur at upper-turning-points (UTP) (Flatté et al., 1979), where the path is horizontal and therefore high correlations in the lateral inhomogeneity of sound speed (which is greatest in the upper ocean) align with the direction of propagation, maximizing their effect. However, it is unknown how intensity fluctuations develop with the number of turning points or depend on turning-point depth. Also unknown is at what ranges, and to what extent, penetration of acoustic energy into geometric shadow zones ("shadow-zone arrivals" (Dushaw, 1999; Van Uffelen, 2009; Uffelen et al., 2010)) should be expected for a given experimental geometry; e.g. is the effect cumulative? Acoustic frequency should determine, in general, the relative importance of spatial scales that influence intensity fluctuations, thus potentially emphasizing different sources of sound-speed variability in the ocean. Whether all of these answers depend on the character of the local oceanography may also be an important consideration. At long range, acoustic paths pass through the upper ocean many times before reaching a receiving hydrophone; the physical mechanisms responsible for particular features of acoustic intensity fluctuations may be obscured by multiple scattering events.

A common measure of acoustic scattering is the fluctuation of intensity. Intensity fluctuations have been measured in many previous short-range experiments, e.g. Ewart (1976); Worcester (1979); Ewart and Reynolds (1984); Reynolds et al. (1985), though most short-range experiments involved transmission of frequencies in the kHz range. An exception was the ATOC Engineering Test (AET), described in Worcester et al. (1999). AET was one of only two short-range ($< 500\,\mathrm{km}$) low-frequency ($< 1\,\mathrm{kHz}$) scattering experiments that have been conducted to date (the other being some of the stations in the Long-range Ocean Acoustic Propagation EXperiment (LOAPEX) (Mercer et al., 2009)). One portion of AET involved transmissions at an

acoustic frequency of 75 Hz over 87 km paths in the Eastern North Pacific Ocean with only one or two UTP. In an analysis of the AET measurements, the scintillation index was reported to be an order of magnitude larger for the path with two UTP than for a path that had only one (Colosi et al., 2009).

In May of 2009, a pilot study/engineering test (PhilSea09) was conducted in the Philippine Sea. For an overview of efforts conducted in the Philippine Sea during 2009-2011 by the North Pacific Acoustic Laboratory (NPAL) (Worcester and Spindel, 2005), see Worcester et al. (2012). The experiment design for PhilSea09 was meant to provide high evolution-time resolution time-series of low-frequency broadband transmissions over a short range, involving paths with one or a few interactions with the upper ocean. Phase-coded m-sequences (Birdsall and Metzger, 1986; Birdsall, 1995) with a 284 Hz center frequency were transmitted from an acoustic projector that was suspended from the R/V *Melville* to a depth near the local sound-speed minimum of the deep sound channel. The transmissions were made at a nominal range of 107 km to a distributed vertical line-array of hydrophones (DVLA) (Worcester et al., 2009) that was deployed as a part of the broader, multi-institution experimental efforts. These measurements are unique in that they provide an unprecedented evolution-time resolution, making it possible to see intensity evolve at 7.2 s intervals. Two of the paths in PhilSea09 were quite similar to the paths in AET. Unlike the AET experiment, transmissions were made nearly continuously (except for some necessary gaps in time, which will be discussed later), and were made in the oceanographically highly-energetic Philippine Sea—while AET (along with many other low-frequency experiments) was undertaken in the Eastern North Pacific Ocean.

Maps of the variance of sea-surface height for timescales of 65 d to 220 d (Kobashi and Kawamura, 2001) suggest that mesoscale activity in the Philippine Sea should be far more prevalent than in the comparatively quiescent propagation environment of

the Eastern North Pacific Ocean. This difference might lead one to expect that range-dependence of the sound-speed field would be a necessary feature of successful ocean models used for acoustic propagation studies in the region. Alford et al. (2011) measured baroclinic energy, energy fluxes, and turbulent dissipation in the Luzon Strait, and found these quantities to be "among the strongest ever measured"; PhilSea09 was conducted approximately 510 km to the East of the Luzon Strait, which would lead one to expect some deterministic temporal dependence of the sound-speed field on tidal timescales.

The purpose of this work is two-fold: first, we report measurements of fluctuations in acoustic intensity made in 2009 in the Philippine Sea, including experimental goals and methods; second, we compare these measurements to Monte Carlo Parabolic Equation (MCPE) simulations. Time-series of acoustic intensity are analyzed to get estimates of measures of fluctuations; these estimates are then compared to a MCPE model with random perturbations of a range-independent background sound speed.

MCPE is a method of modeling acoustic fluctuations that are induced by variability in the ocean. MCPE simulations have been used by Colosi et al. (1994); Wolfson and Spiesberger (1999); Xu (2007); Van Uffelen (2009), among others. Ocean variability as it pertains to ocean acoustics includes, but is not limited to, displacements due to ocean internal tides, vertical displacements from a background of diffuse internal waves, mesoscale eddy propagation, and spice (buoyancy-compensated water masses with sound speed that is different than surrounding water masses). This particular implementation of the MCPE method includes only diffuse internal waves. The parabolic equation contains the relevant physics for propagation; the MCPE method provides an evaluation of the simulated propagation environment, which is composed of a background sound-speed plus perturbations. The perturbations are modeled as being due to ocean internal waves as described by the Garrett-Munk (GM) spectrum

(Munk, 1981). We do not assert that the GM spectrum is necessarily the optimal model for diffuse internal waves (various corrections or alternative descriptions have been proposed, e.g. Levine (2002); Pinkel (1984)), but only that it is a reasonable starting-point in attempts to understand acoustic fluctuations. The goal for the comparison to MCPE simulations is to test whether the non-diffuse-internal-wave aspects of the local oceanography cause overwhelming differences in the character of intensity fluctuations, thus precluding inter-regional comparison to experiments conducted in the Eastern North Pacific Ocean—where predictions of MCPE using a GM internal-wave description have largely been successful. As an example, Xu (2007) conducted broadband simulations that predict the order-of-magnitude difference in scintillation index for the two paths in the AET experiment.

The organization of this paper is as follows: section 2.2 gives a description of the experimental methods, along with the acoustic and environmental observations made. Section 2.3 examines the MCPE model. This section contains an analysis of temperature, salinity, and pressure measurements collected by instruments on the DVLA, for the purpose of adjusting the GM model displacements to a value appropriate for the region. MCPE results for the adjusted model are presented along with the measured acoustic fluctuations in section 2.4. Section 2.5 includes a discussion of the comparison, and section 2.6 provides conclusions and a direction for further study. Appendix 2.8 describes the convergence tests that determined the maximum internal-wave mode number to be included in the ocean model and the appropriate PE range-step.

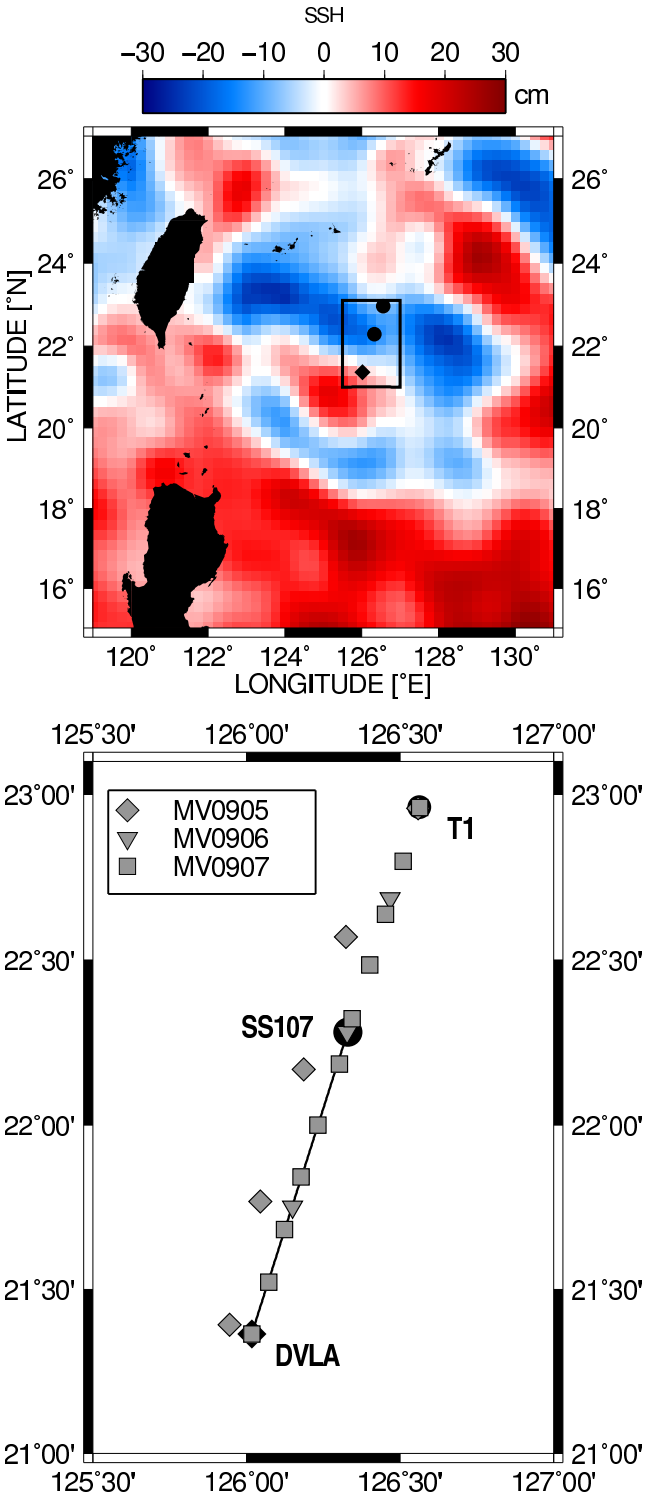

Figure 2.1: Experimental plan for the PhilSea09 experiment. The top panel shows the region, including the islands of Taiwan and Luzon at 121° E Longitude, 24° and 17° N Latitude, respectively. The color scale shows the sea-surface height for YD 119 of 2009 from the AVISO (Aviso and support from Cnes, 2012) database. The bottom panel shows the region bounded by the rectangle in the top panel. Sets MV0905, MV0906, and MV0907 denote CTD casts made on three consecutive 2009 cruises. The surveyed locations of the transmitter at station SS107 and the DVLA were 22.282 500° N, 126.329 445° E and 21.364 963° N, 126.017 090° E, respectively. The label "T1" refers to an acoustic transceiver mooring also deployed as part of PhilSea09, but is only shown here for context and will not be discussed in this work.

2.2 Experiment

2.2.1 Overview

A map of the region of the experiment, including the location of the DVLA and the R/V *Melville*'s position during acoustic transmissions, appears in figure 2.1. The location of the ship during acoustic transmissions was designated "SS107" due to its nominal range from the DVLA. The ship's position was determined by a C-Nav GPS receiver, which was described previously in Mercer et al. (2009). The C-Nav's antenna was located on the R/V *Melville*'s A-frame, directly above the deployment sheave used to support the acoustic projector, which was suspended over the stern.

The projector was lowered to a depth of 1000 m. The depth of the sound speed minimum was later determined from smoothed, averaged conductivity, temperature, depth (CTD) cast data to be 1040 m. Measurements taken from a pressure gauge attached to the projector were used to track its depth during transmissions. These measurements, along with other diagnostic measurements, such as the temperature of the power transformer in the transmitter package, and the transmitted acoustic level, were sent up the suspending cable through an optical fiber. At SS107, two acoustic transponders were deployed along the geodesic connecting the projector and the DVLA for the purpose of tracking the projector's position during transmissions. An acoustic pinger was located on the transmitter package and interrogated the bottom-deployed transponders, forming a long-baseline transponder net.

The over-the-side transmitter package (Andrew, 2009) was assembled and deployed over the stern of the R/V *Melville* by the Applied Physics Laboratory at the University of Washington (APL/UW). The package consisted of an experimental double-ported doubly resonant electro-acoustic transducer, designated MP200/TR1446, designed by ImageAcoustics Inc and manufactured by Massa Products, Inc., a match-

ing auto-transformer/tuner manufactured by Coiltron, Inc., a tracking pinger, auxiliary sensors, and battery power for the sensors.

The MP200/TR1446 was operated between its two resonances, both quite sharp at about 210 Hz and 320 Hz, in an attempt to provide a "broadband" device. A model of the complete system transfer function is shown in figure 2.2. It was desired to attempt to utilize the full "broadband" bandwidth of the device, and therefore a $Q = 2$ drive signal was designed that had a 1023-bit m-sequence (Munk et al., 1995), a carrier frequency of 284 Hz, and 2 cycles of the carrier for each bit of the sequence. This signal had an approximate bandwidth of 142 Hz, from about 212 Hz to 356 Hz, a band which roughly incorporates both resonant peaks. Since the system response was far from flat over this band, an equalization filter was designed to compensate for the dual-peaked response. This filter was applied to the drive signal prior to transmission, and hence is called the "pre-equalizer". The transfer function of the pre-equalizer is shown in figure 2.2. Without equalization, the system distortion introduced significant "ringing" after the pulse-compressed pulse of the m-sequence. The theoretical performance of the pre-equalizer eliminated the ringing in pre-cruise models.

After the cruise, inspection of the waveforms received on a package monitor hydrophone and on the DVLA hydrophones indicated that the pre-equalizer was not accurately compensating for the system transfer function. Therefore, a further "post-equalizer" filter was designed, based on Wiener filter theory, and applied on the received data. The response of the post-equalizer is also shown in Fig. 2.2. The final result on pulse compression using both pre- and post-equalization is shown in the bottom panel of Fig. 2.2: the post-equalizer completed the task of adjusting the received signal Fourier content (i.e., phase and magnitude) into a reasonable facsimile of the Fourier characteristics of an m-sequence with a 130 Hz bandwidth and pulse

resolution of 7.7 ms. The RMS source level, measured in the water with the transmitter package monitor hydrophone, was roughly 183 dB re 1 μPa @ 1 m. The vertical beam-width of the MP200/TR1446 was 120°; the transducer is omni-directional in azimuth.

Acoustic signals were transmitted from SS107 for approximately 60 h, compared to the local inertial period of 32 h. Thus our observations include nearly two periods of the slowest internal waves (which, admittedly is not enough time to study the statistics of acoustic fluctuations due to these slowest waves), but 90 cycles of waves at 6 cycles per h (this was the surface-extrapolated buoyancy frequency in the region of the experiment). Our observations are not of sufficient duration to study the statistics of slower ocean processes, such as mesoscale eddies.

The acoustic signals were m-sequences with a duration of 7.2 s, and were transmitted nearly continuously from SS107. The planned transmission schedule included gaps at the change of each hour to ensure that acoustic tracking of the DVLA's position would not be affected. Further gaps in transmission were necessary to prevent overheating of the power amplifier. These data were post-equalized and then pulse-compressed in the standard way (Birdsall and Metzger, 1986; Birdsall, 1995). Some data were contaminated due to power amplifier glitches or due to sonar signals of unknown origin; these data were also removed.

The DVLA was located at 21.364 963° N, 126.017 090° E and is described in further detail in Worcester et al. (2012); we provide here only the details pertinent to our analysis. The DVLA was composed of both upper and lower sub-arrays, each consisting of 30 hydrophones. The upper sub-array spanned the deep sound channel axis, or sound speed minimum. This upper sub-array had hydrophones at depths of 651 m, 725 m, and then every 25 m from 800 m to 1400 m, followed by hydrophones at 1475 m, 1550 m, and 1625 m. Receptions made on the lower sub-array are not dis-

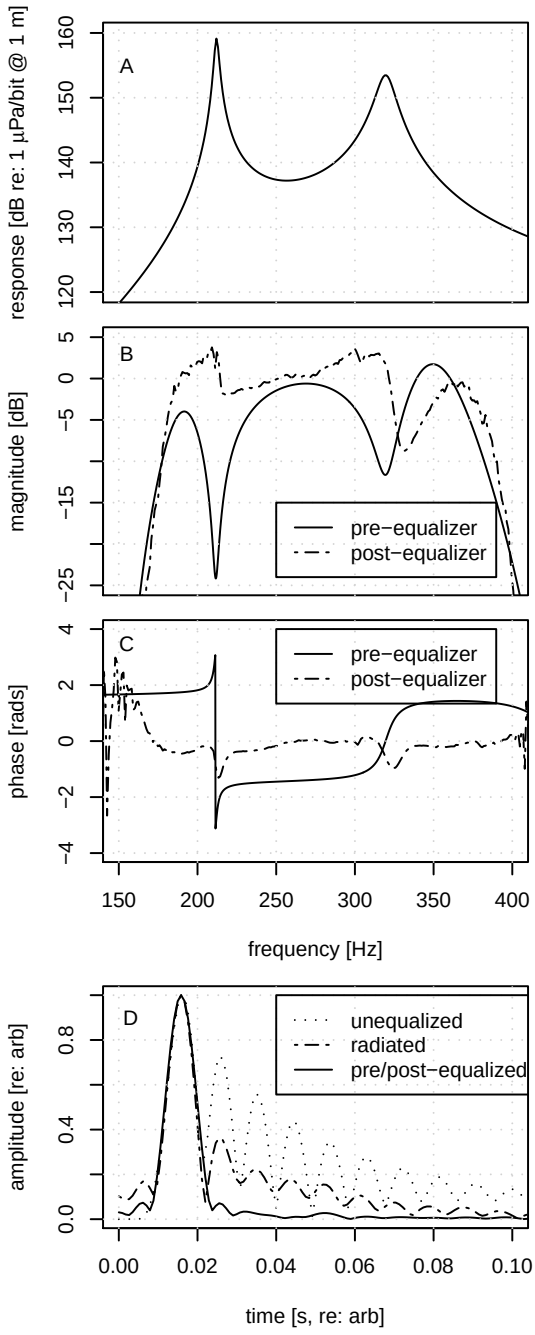

Figure 2.2: Transmission signal design, PhilSea09. Panel A: Theoretical system transfer function into the water, computed from equivalent circuit model. Panel B: Magnitude of the pre- and post-equalizer filters. Panel C: Phase of the pre-and post-equalizer filters. Panel D: Pulse-compressed m-sequences without any equalization, with pre-equalization after passing through the system (chiefly the MP200/TR1446 transducer) into the water ("radiated"), and receiver waveform after post-equalization.

cussed in this paper. The hydrophones were High Tech, Inc. model HTI-90-U. The sample rate of these hydrophones was set to a nominal value of 1953.125 samples per s, though the clock rate in individual hydrophones varied slightly. This clock-rate error was determined for individual hydrophones and an appropriate correction was applied.

Significant "blow-downs" of the DVLA occurred during the month of its deployment, presumably as a result of the strong local internal tides. These low-velocity blow-downs resulted in changes in hydrophone position of up to 90 m in the vertical and up to a few hundred meters in the horizontal. Intensities computed by ray-tracing (with the RAY program (Bowlin et al., 1992)) indicated that the effects of changes in hydrophone position were not large enough to be considered significant. The ship's position was maintained by a dynamic positioning system, but ship heave due to wave motion and currents resulted in motion of the acoustic projector. The effects of projector motion on intensity (a Doppler shift in the signal, which reduces the gain achieved by pulse-compression) were also found to not be significant.

2.2.2 Acoustic data

The RAY program, with the background vertical sound speed profile $\bar{c}(z)$ as input, was used to model the acoustic paths studied here; $\bar{c}(z)$ and several representative paths are shown in figure 2.3. The ID nomenclature used in the figure is a concise way of describing key features of a given acoustic path between a transmitter and receiver. The +/- sign refers to the sign of the angle made between the associated acoustic energy leaving the projector and the horizontal, while the number that follows refers to the number of upper and lower turning-points for that path between the transmitter and receiver. The paths shown reaching the upper sub-array of the DVLA are refracted-only in the sound-speed profile shown in the figure. There is a surface-

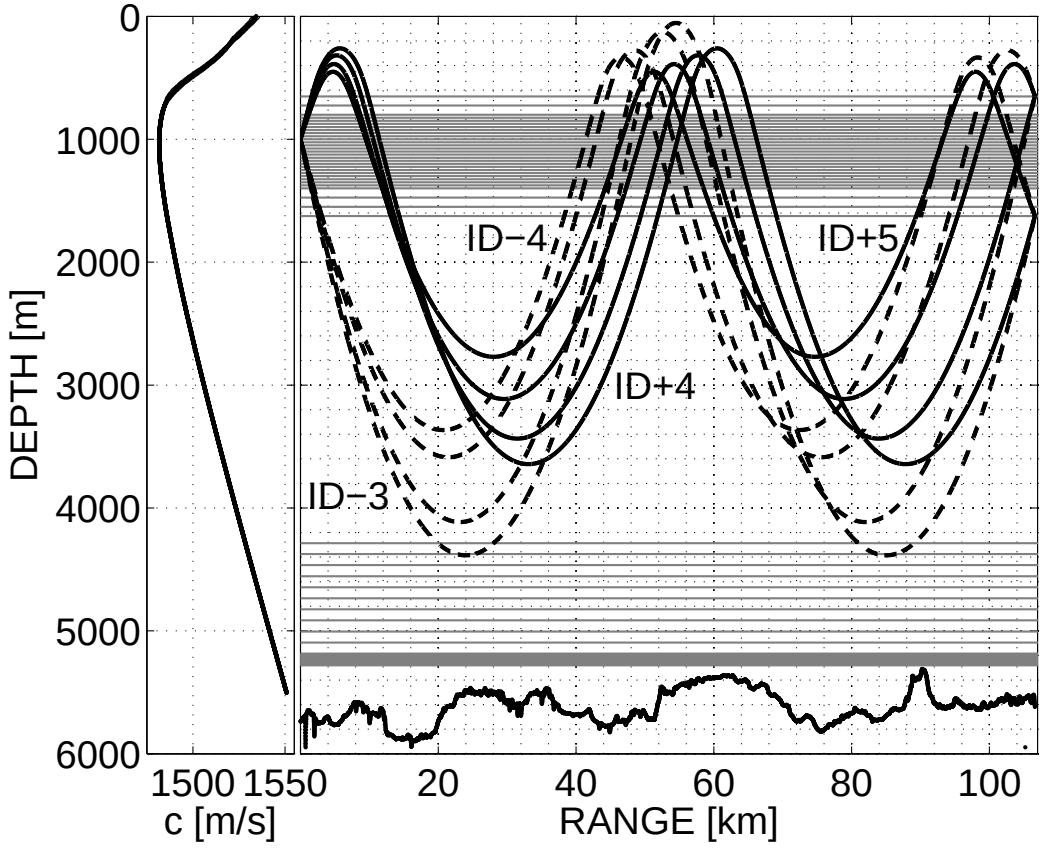

Figure 2.3: The vertical sound-speed profile used in this work is shown at left; at the right are the typical eigenrays studied. The gray horizontal lines represent the depths of hydrophones on the upper and lower sub-arrays on the DVLA, and the solid gray band near the bottom is a closely-spaced (5 m) group of hydrophones. We study receptions on all 30 hydrophones of the upper sub-array for the paths marked 'ID-3','ID+4', 'ID-4', and 'ID+5'. Only eigenrays reaching the shallowest and deepest hydrophones on the upper sub-array (651 m and 1625 m depth) are shown. Paths leaving the source at an upward angle are shown with solid curves; paths leaving the source at a downward angle are shown with dashed curves. The solid black curve at the bottom of the figure is the bathymetry that was measured along the propagation path with the R/V *Melville*'s multi-beam sonar.

bounce path that arrives 40 ms after the first arrival (ID-3) at the upper sub-array, but we neglect it here as the pulse-width of the processed receptions was 7.7 ms, so that we may window out this surface-bounce path in time.

Throughout this paper, we will refer to transmissions received on the upper sub-array at all receiver depths; in particular, we will study paths ID-3, ID+4, ID-4, and ID+5. These paths are separable in time, except that for a few depths near the center of the sub-array paths ID+4 and ID-4 may not be separated from each other, and at the bottom of the sub-array path ID+5 may not be separated from later arrivals. Upper turning depths for the four paths are given in table 2.1.

PATH	ID-3	ID+4	ID-4	ID+5
UTP DEPTH [m]	53-126	260-317	276-334	388-451
HYD. DEPTH [m]	1625-651	1625-651	651-1625	651-1625

Table 2.1: Upper turning point depths and associated receiver depths: for paths ID-3 and ID+4, the shallowest-turning eigenrays reach the deepest receiver of the sub-array; for paths ID-4 and ID+5, the shallowest-turning eigenrays reach the shallowest receiver of the sub-array.

Each arrival is tracked using the acoustic transponder navigation solution for the array position. We find the peak of the arrival envelope, window data in a 10 ms window and take the Fourier-transform; the absolute square of the 284 Hz component is computed as the single-frequency intensity.

An example set of 60 h time-series of acoustic log-intensity for the four paths that were recorded on the 900 m depth hydrophone is shown in figure 2.4. These are characteristic of the records for the great majority of hydrophones, and represent the first-order acoustic fluctuations modeled in this paper. An additional time-series of intensity for ID-3 from a hydrophone at 1550 m depth is also shown in the figure.

Readily apparent in the 1550 m ID-3 time-series are long-period deep fades. Similar fading does not appear in the records for ID+4, ID-4 and ID+5, nor is there any other obvious feature in these intensity records at times when fading is observed in ID-3. The fading in path ID-3 is most apparent at depths 1150 and deeper, and becomes more pronounced with increasing depth.

2.2.3 Environmental data

A total of 81 expendable bathythermograph (XBT) casts were made along the geodesic connecting the DVLA and SS107 positions. Mixed layer depths as deep as 80 m were measured to the northeast of SS107 in these casts; also apparent was strong range-dependence in the upper ocean. Satellite-based measurements of sea-surface height from the AVISO (Aviso and support from Cnes, 2012) database exhibit sea surface height anomalies with a sign consistent with the horizontal temperature variation measured by the XBT casts (shown in figure 2.5). These range-dependent variations could be explained by the presence of eddies.

A total of 21 conductivity-temperature-depth (CTD) casts were taken during PhilSea09 over a period of time lasting from April 02 to May 12, along or near the geodesic connecting the DVLA and SS107. The positions of the CTD casts are shown in figure 2.1. Data from 19 of these casts were smoothed and averaged to create the range-independent "background" profiles of sound speed $\bar{c}(z)$, buoyancy frequency $N(z)$, and the vertical gradient of potential sound speed $\mathrm{d}\bar{c}_{Pot.}/\mathrm{d}z$ used in MCPE and RAY modeling described in sections 2.2.2 and 2.3.

In addition to profile-type environmental data, time-series of temperature, salinity, and pressure were collected throughout April and May with instruments attached to the DVLA (Colosi et al., 2013). Data from these 12 pumped microCAT CTD instruments were analyzed to provide an estimate of GM strength subsequently used

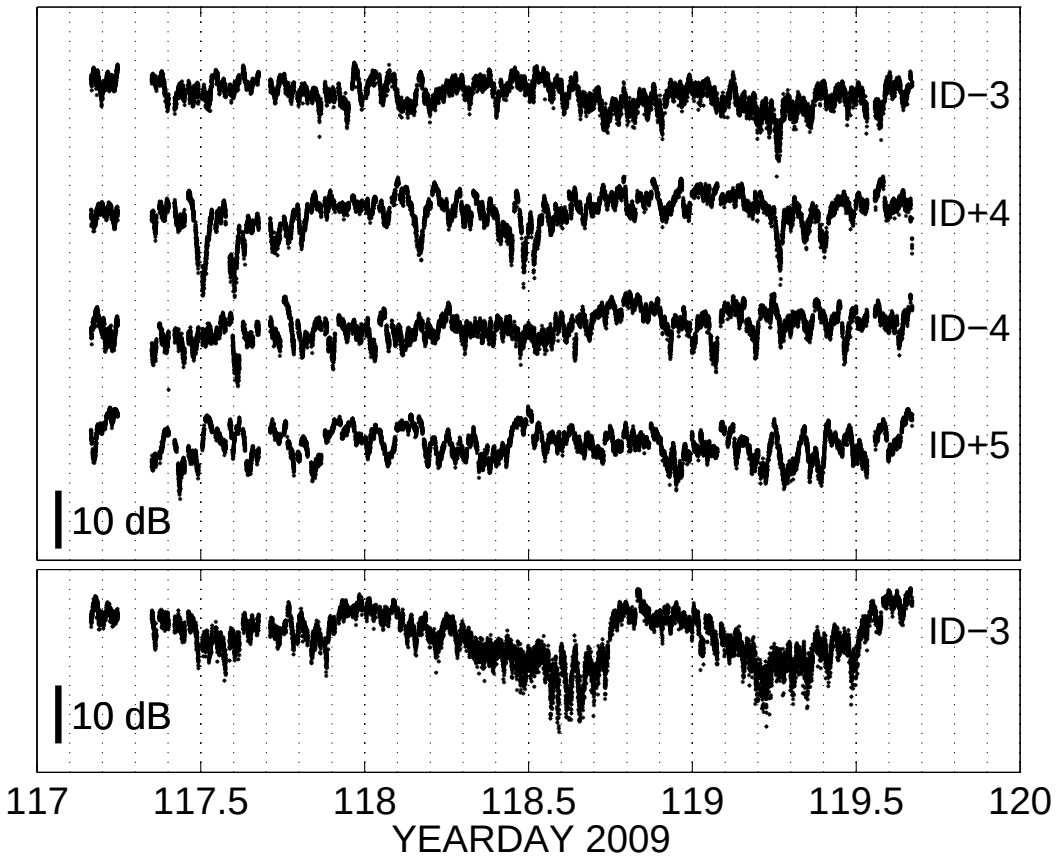

Figure 2.4: The top panel shows as an example time-series of $10log_{10}(I/\langle I\rangle)$, recorded on the 900 m hydrophone, for paths ID-3, ID+4, ID-4, and ID+5. The bottom panel shows ID-3 for the 1550 m hydrophone—an example of the deep fades (at YD 118.5 and 119.25) observed on the deeper phones of the shallow array. A bar representing the scale appears in both panels to the left of the label "10 dB".

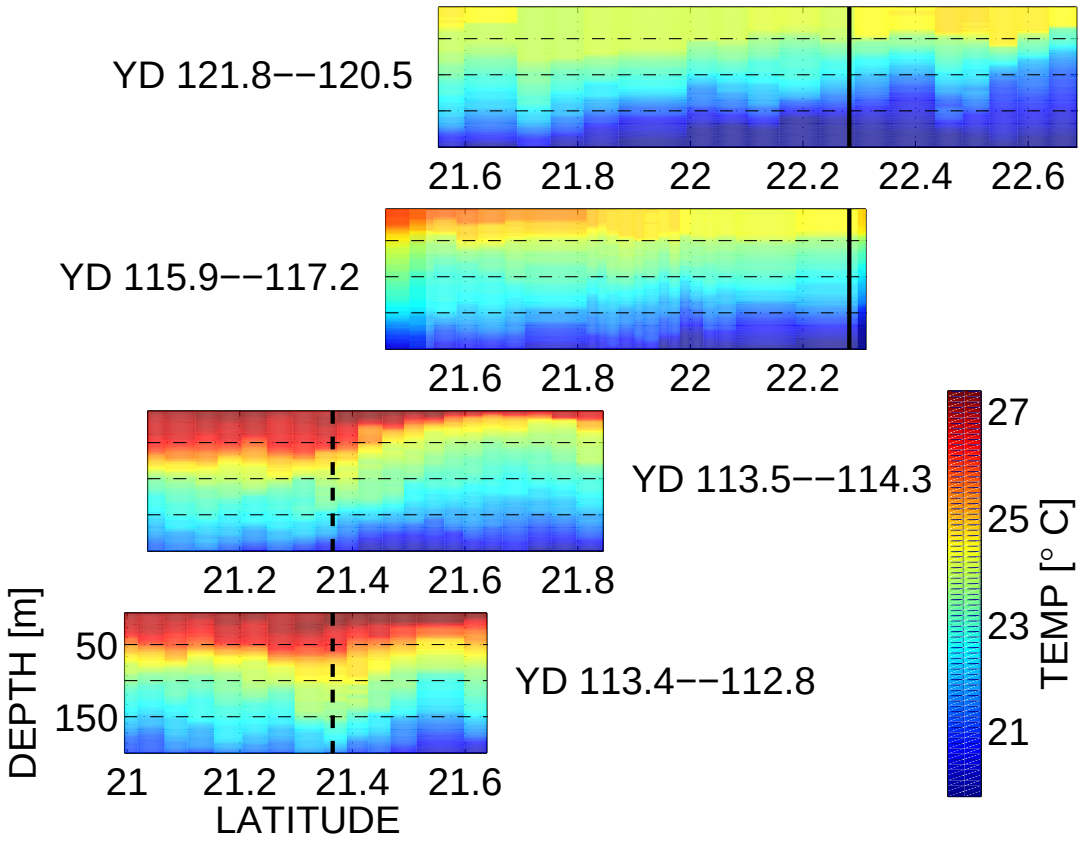

Figure 2.5: Shown here are XBT transects of ocean temperature, with latitude increasing from left to right, and time increasing from the bottom to the top of the figure. Note that the time in yeardays increases from left to right, except in the bottom and top panels, as indicated by the labels to the right or left of each panel. Individual casts were made an hour apart in time while the ship was underway. A strong range-dependence and some time-dependence are evident from the measurements. The vertical dashed and solid lines show the latitudes of the DVLA and SS107, respectively, for reference.

in the "adjusted" MCPE model, described in section 2.3.2.

2.3 Modeling

2.3.1 Ocean sound speed fluctuations

One parameter which may be adjusted in the GM spectral model of internal waves is the "strength", s_{GM}, which we will describe here as the product

$$s_{GM} = N\langle\zeta^2\rangle = 0.5 \cdot bE_{GM}N_0b \tag{2.1}$$

or the variance of the internal wave vertical displacement, ζ, scaled by the buoyancy frequency $N(z)$. In equation 2.1, b is the thermocline depth-scale, E_{GM} is the reference internal-wave energy level, and N_0 is the reference buoyancy frequency. Although ζ and N are functions of depth, their product, s_{GM}, is a constant, independent of depth. In the approach taken in this paper, we adjust the quantity s_{GM} in our simulated oceans to match the value we will here estimate from environmental observations.

After summation over the vertical internal-wave modes, the GM vertical-displacement spectrum $F_{\zeta\zeta}$ (scaled by N) is given by the equation

$$NF_{\zeta\zeta}(\omega) = \frac{2bE_{GM}N_0b\omega_i\sqrt{\omega^2 - \omega_i^2}}{\omega^3\pi} \tag{2.2}$$

where ω is frequency, and ω_i is the inertial frequency. Ocean internal waves exist at temporal frequencies between the inertial frequency and the local buoyancy frequency.

We seek to make an estimate of the scaled variance of displacement $N\widehat{\langle\zeta^2\rangle}$, which is equal to the integral over frequency of equation 2.2. The best source of information about temporal variability of the propagation environment was the collection of microCAT CTDs deployed on the DVLA. Time-series of displacement may be computed from the temperature, salinity and pressure records obtained by these instruments,

and then examined in various ways to get estimates of the GM strength for the Philippine Sea. We express this strength as the ratio $\hat{r}$ of the measured strength $\hat{s}$ to the standard GM strength:

$$\hat{r} = \frac{\hat{s}}{s_{GM}} = \frac{N\widehat{\langle\zeta^2\rangle}}{N\langle\zeta^2\rangle} \tag{2.3}$$

One approach would be to high-pass filter the time-series of displacement above the inertial frequency, and then calculate the variance of the resultant time-series, assuming the spectrum falls rapidly—such that any part of the spectrum above the local buoyancy frequency will provide a negligible contribution. Alternatively, if the tides were well-known and well-modeled, the time-series could be fit with a tidal model, and the fit removed. We choose here to make an estimate of the GM spectral level, $\widehat{F_{\zeta\zeta}(\omega)}$, in the region of the experiment, and integrate it to find an estimate of the strength ratio $\hat{r}$ (recall that multiplication by $N(z)$ makes this ratio depth-independent)

$$\hat{r} = \frac{N\int \widehat{F_{\zeta\zeta}(\omega)}\,\mathrm{d}\omega}{N\int F_{\zeta\zeta}(\omega)\,\mathrm{d}\omega} \tag{2.4}$$

Data from the 12 pumped microCAT CTDs on the DVLA were analyzed as described below to make an estimate of the GM strength parameter. The temperature-salinity-pressure measurements were first converted to sound speed using the TEOS-10 algorithms (TEOS-10, 2010) and are shown in figure 2.6. The array blow-downs mentioned earlier introduced fluctuations into the records as a result of the changes in depth of the sensors. The sound speed data were interpolated in depth in an attempt to remove this instrument-caused fluctuation. Several interpolation methods were examined, but the choice of interpolation method did not strongly influence the estimate; for its simplicity, a linear interpolation scheme was chosen. Time-series of displacement were computed by the relation

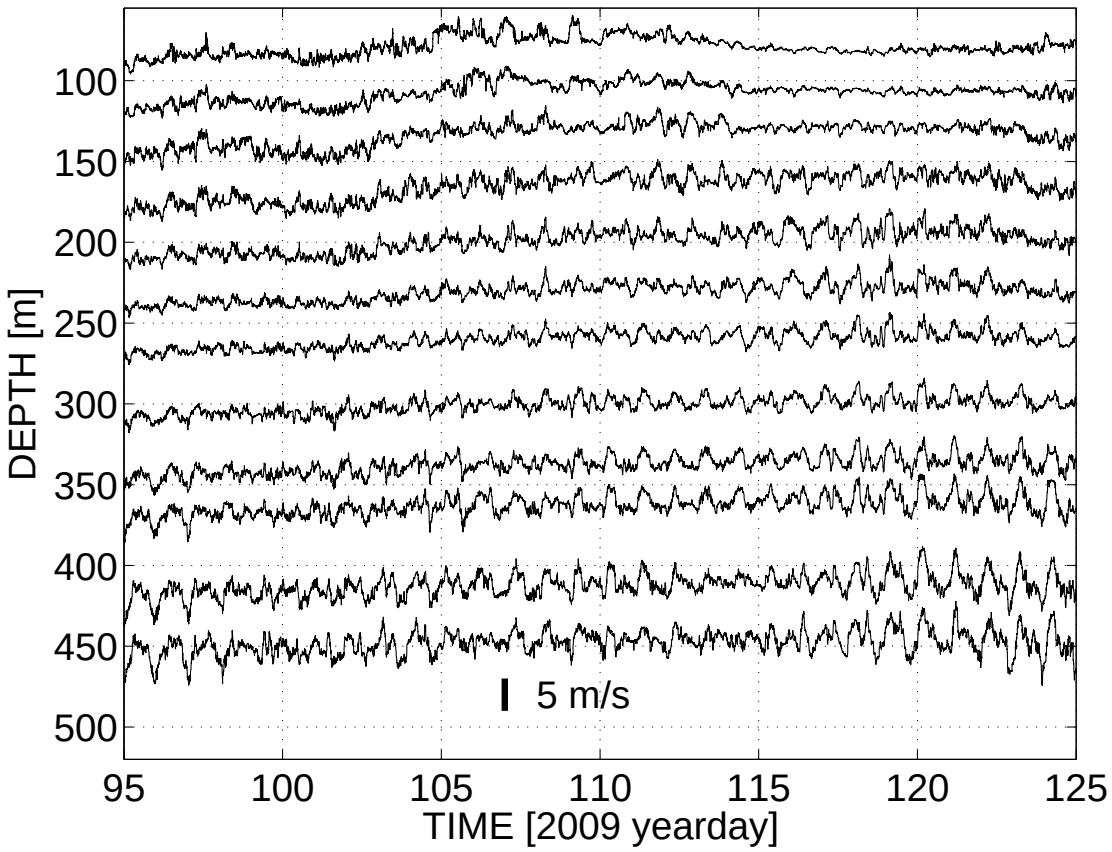

Figure 2.6: Time-series of sound speed variability computed from CTD measurements made on the DVLA. Each record is offset according to the sensor's mean depth. The vertical bar shows the scale of sound speed fluctuations.

$$\zeta(t;z) = \delta c(t;z) \left(\frac{\partial \bar{c}}{\partial z} \right)^{-1}_{Pot.} \tag{2.5}$$

The potential sound-speed gradient is appropriate because we don't want to include the effect of the portion of the gradient that is due to the pressure increase with depth. Spectra were estimated from these time-series using the multitaper approach (Percival and Walden, 1993) with a time-bandwidth product of 4. The spectra are shown in figure 2.7.

Various different approaches might be taken to estimate the "background" level of these diffuse internal waves in the region of the experiment. As may be seen in the estimate of the spectrum of sound speed fluctuations shown in figure 2.7, the locally-generated internal tides are a prominent source of variability in the Philippine Sea; these tides present a complication in estimating the level of variability due to diffuse internal waves. Ignoring these, the spectrum at higher frequencies appears, visually, to fit reasonably with a GM strength of $\hat{r} = 2$. This should be an useful check against any estimate we might make.

Since it is not clear to what extent the GM spectrum includes contributions from any contaminating local tides, we find it reasonable to make estimates of upper and lower bounds on GM strength for the region of the experiment. In equation 2.4, to calculate an upper bound on the GM strength, we integrate from the inertial to buoyancy frequencies. We consider the quantity

$$\phi(\omega) = \frac{\int_{\omega_i}^{\omega} \widehat{F_{\zeta\zeta}(\omega)} \mathrm{d}\omega}{\int_{\omega_i}^{N} \widehat{F_{\zeta\zeta}(\omega)} \mathrm{d}\omega} \tag{2.6}$$

where ω_i is the inertial frequency. This is the fraction of the contribution to the integral of $\widehat{F_{\zeta\zeta}}$ as a function of ω. Between 30 % to 55 % of the variance is due to the K1 tide, 10 % to 20 % due to the M2, and lesser amounts to the K3 and M4 components (with no easily-discernible trend in depth). In an attempt to calculate a lower bound on GM strength, we want the (local internal, deterministic) tides to be excluded from the variance, and therefore exclude the regions shaded in gray in figure 2.7.

The bounds in frequency of the excluded regions are chosen by eye. The assumption made is that the local tidal energy is defined as energy rising above a background spectral level due to diffuse internal waves. The extent to which the level between bands is filled in by the energy in the bands is not known. For example, if one were

to draw a line through the troughs between bands in figure 2.7, it would not seem to fit the GM model well in terms of its slope, in addition to appearing to be at a lower level than that apparent for higher frequencies. Estimates $\hat{r}$, (averaged in depth) of upper (3.33) and lower (1.6) bounds of GM strength appropriate for the Philippine Sea are given in figure 2.8. The lower estimate of 1.6 seemed to be consistent with the spectral level at higher frequencies and so was chosen as the level to be used in MCPE modeling. This level is in good agreement with the estimate of the GM strength made by Colosi et al. (2013), who used a tidal model to estimate and remove tides from the microCAT-derived displacements: their estimate of the GM strength was 1.4. They conclude that the outlook for modeling the internal tides is unclear; the agreement between our estimates, determined by a different approach, would seem to support the validity of their result.

2.3.2 MCPE

The Monte Carlo Parabolic Equation method is commonly used in the ocean acoustics community to model acoustic signal fluctuations in 2D. The idea is to generate random instances of an inhomogeneous sound-speed field that consists of some range-independent or slowly-varying background $\bar{c}(x, z)$ plus perturbations $\delta c(x, z)$ to this background. In this work we model the background sound speed as range-independent: $\bar{c}(x, z) = \bar{c}(z)$. The sound-speed perturbations are modeled as being solely due to internal waves whose statistics are consistent with the Garrett-Munk spectrum.

We employ an internal wave simulator that is described in Henyey and Reynolds (2013). The simulator produces vertical "slices" of an internal-wave displacement field, $\zeta(x, z)$, from which perturbations to the background sound speed are calculated. The perturbations are proportional to the vertical gradient in potential sound speed

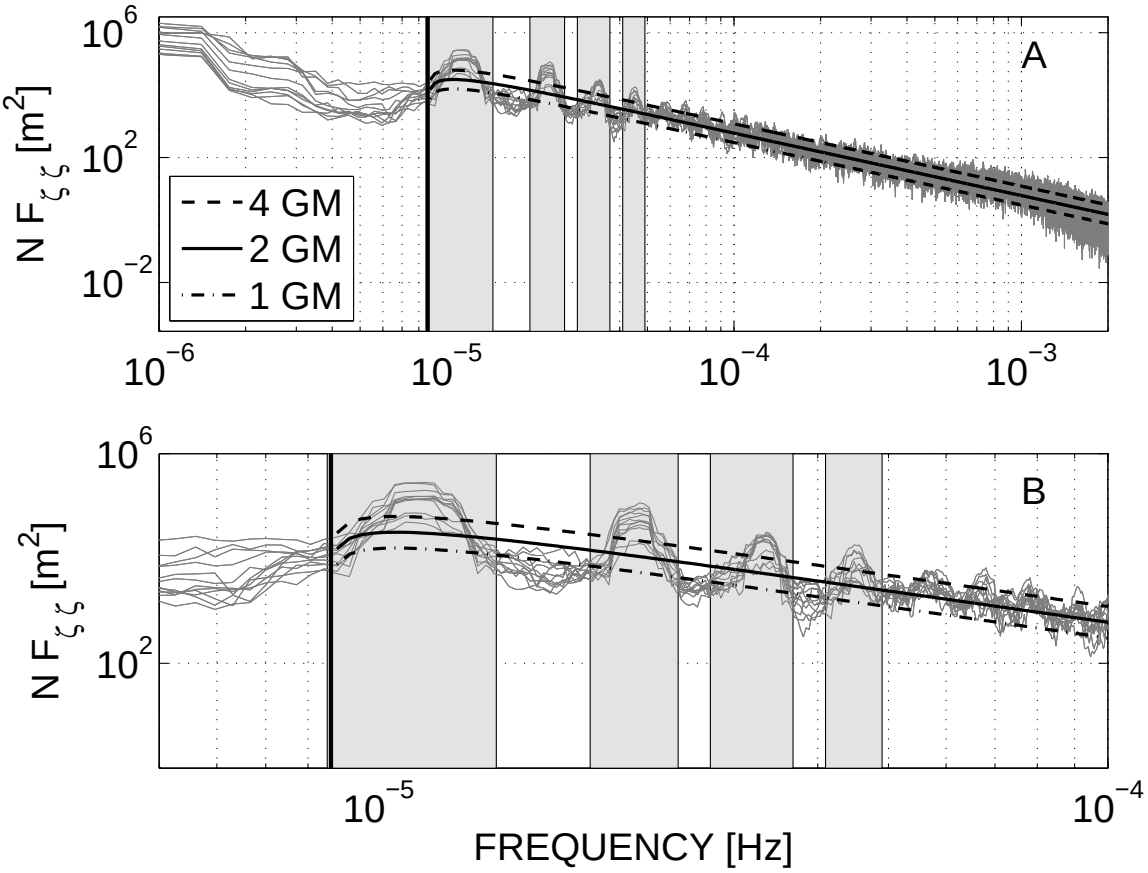

Figure 2.7: Panel A: spectra of displacement from the 12 microCAT CTD sensors on the DVLA. The spectra have been scaled by the buoyancy frequency. The thick black vertical line is the inertial frequency. There are 4 prominent tidal peaks visible in the spectra, known as the K1, M2, K3, M4 tides (Colosi et al., 2013) (in order from left to right) that appear just to the right of the inertial frequency on the plot. The gray shaded regions highlight the frequencies for which these four tidal peaks appear to rise above the background level. Superimposed are the GM spectra for strengths $\hat{r} =$ 1, 2 and 4 (appearing from bottom to top) for reference. Panel B shows the portion of the spectra near tidal frequencies in greater detail.

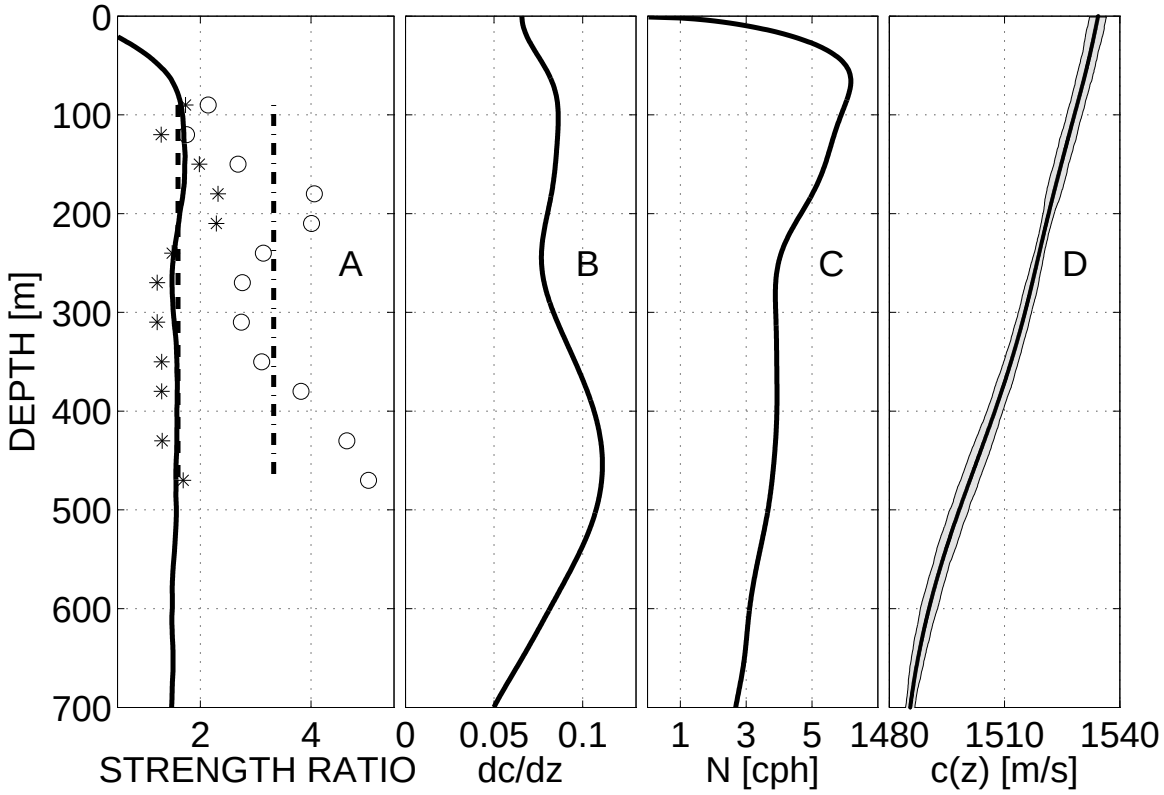

Figure 2.8: Panel A: estimates of the strength ratio $\hat{r} = \hat{s}/s_{GM}$ made from the individual microCAT sensor time-series of displacement. The tides are included in the integral over the spectra shown in figure 2.7 for the estimates shown with a 'o' symbol, with the mean estimate shown by the dash-dot line. The tides are excluded from estimates shown with a '*', with the mean estimate shown by the dashed line. The solid curve shows the strength ratio estimated from 100 simulated oceans. Panel B: the vertical potential sound speed gradient in $\mathrm{m\,s^{-1}\,m^{-1}}$. Panel C shows the buoyancy frequency. Panel D: smoothed, averaged sound speed, from the 19 CTD casts. The gray region shows 1 std.

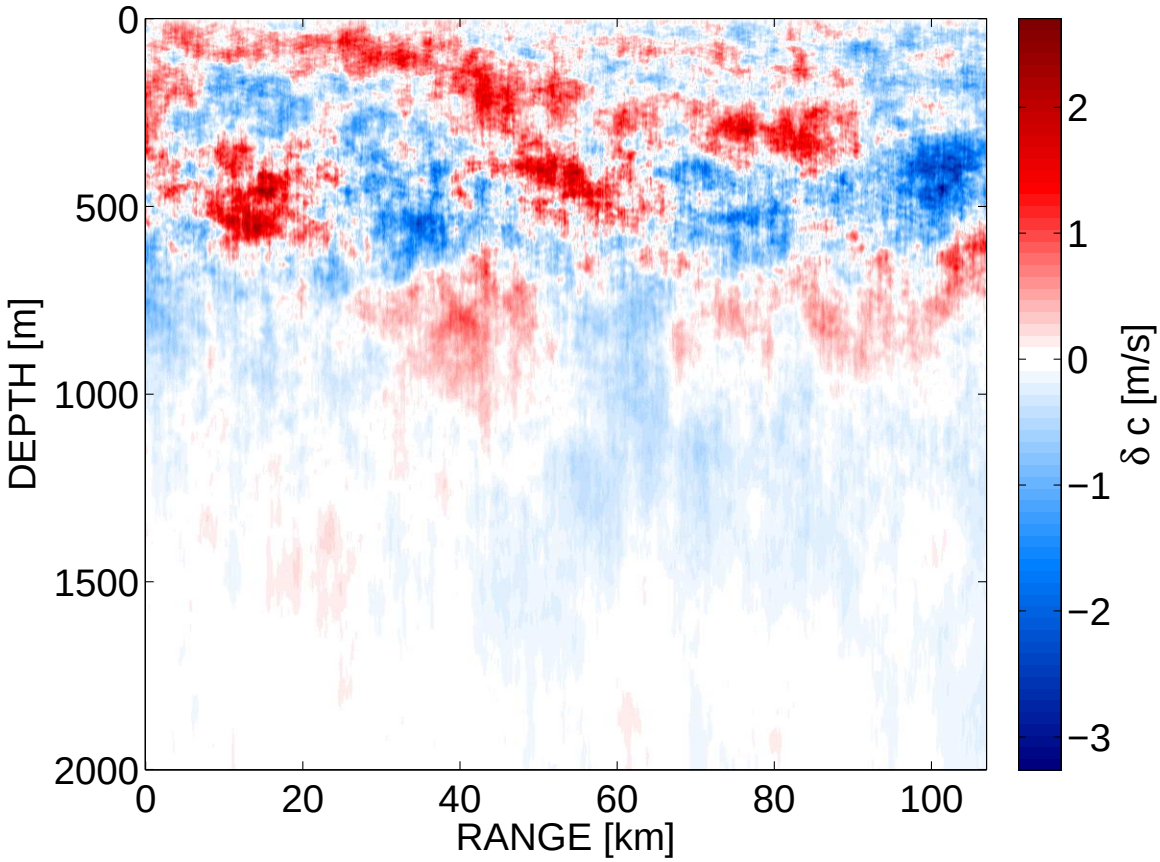

Figure 2.9: An example of a $\delta c(x, z)$ range-depth slice from simulation. The full propagation range is shown, but only the upper 2000 m of the slice are shown; fluctuations are much smaller below this depth.

at depth z:

$$\delta c(x, z) = \left(\frac{\partial \bar{c}}{\partial z}\right)_{Pot.} \zeta(x, z) \tag{2.7}$$

An example vertical slice of $\delta c(x, z)$ is shown in figure 2.9.

Parabolic equation models and associated computer codes that are used for studies of underwater acoustic waves are well-known and plentiful. We chose the Navy Standard Parabolic Equation, or NSPE, for this work—see appendix 2.8 for further

description. Each perturbed sound speed field is written to an input file for the NSPE code, then broadband propagation through this environment is computed. A time-front is produced, from which arrivals are windowed and the single-frequency intensity is computed as was done with the acoustic transmission data.

The acoustic source spectrum was modeled as Gaussian, centered at a frequency of $f_{center} = 284\,\mathrm{Hz}$, and falling to a value of $S(f = f_{center}) * 1/e$ at frequencies of $f_{center} \pm f_{center}/4$. Propagation was calculated at 852 frequencies with a spacing of $1/3\,\mathrm{Hz}$, over the band $f_{center} \pm f_{center}/2$. The frequencies outside the $1/e$ level were included in order to reduce ringing in the timefront.

In the work presented in this report, two types of MCPE simulation are used. In one of the simulations, a time-independent MCPE (which will be referred to as the "TI simulation"), independent random instances of the internal-wave displacement field are computed; in the second simulation, a single random internal-wave displacement field is evolved in time, allowing for time-dependent model-data comparison (the "TD simulation"). The TI simulation consisted of 226 random instances of a 2-D (range-depth) slice of perturbed sound-speed, like that shown in figure 2.9. For the TD simulation, the internal-wave displacement field was evolved at a time-step of 240 s for a total of 320 h (ten times the local inertial period, the longest timescale in the GM spectrum), generating a time-series composed of a total of 4800 timefronts.

2.4 Results

We will consider as measures of the intensity fluctuations the scintillation index (SI) (which is the fourth moment of the acoustic field and the second moment of intensity, normalized by the mean intensity squared):

$$SI = \frac{\langle I^2 \rangle - \langle I \rangle^2}{\langle I \rangle^2} \tag{2.8}$$

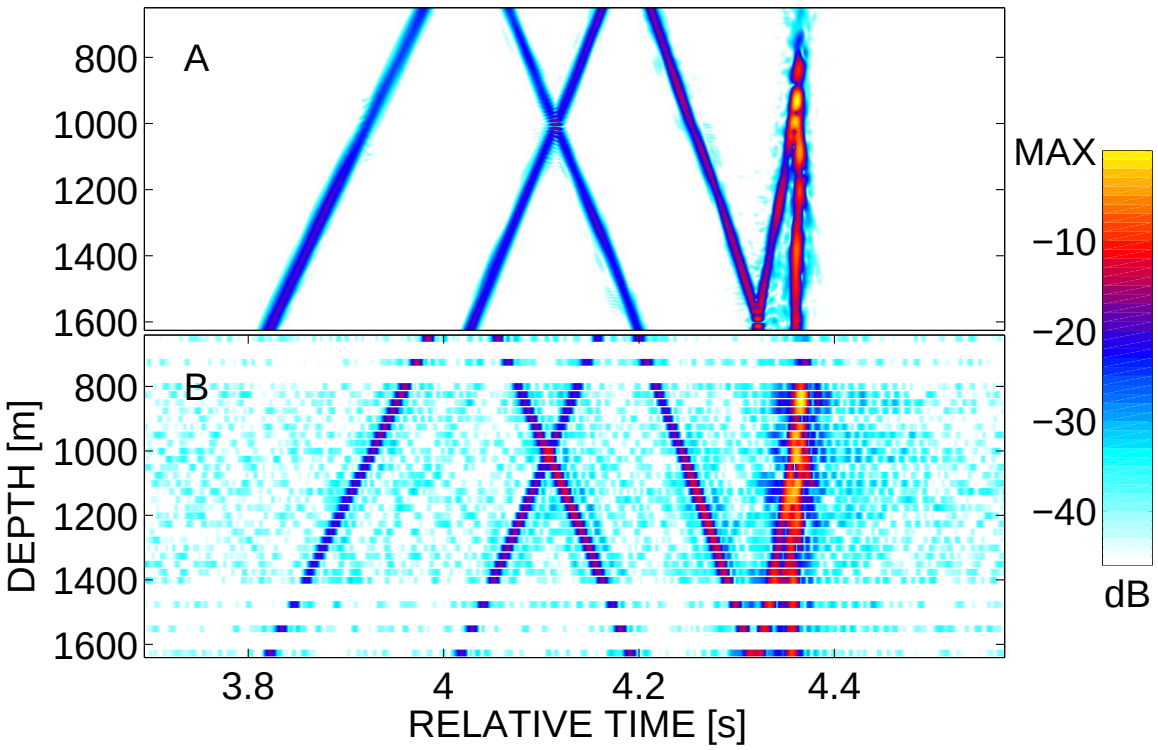

Figure 2.10: Panel A: An example MCPE timefront. Panel B: An example of a measured timefront received on the upper sub-array of the DVLA, after hydrophone clock corrections and post-equalization have been applied. Gaps are due to hydrophone spacing in depth. The first four arrivals on the portion of the array above 1000 m are paths ID-3, ID-4, ID+4, and ID+5, ordered from earlier to later time (the order-of-arrival of paths ID-4 and ID+4 is seen to switch below 1000 m depth). In each panel, the color scale is relative to the maximum intensity shown in the window.

and the variance of log-intensity, where the log-intensity, ι, is given in dB by $\iota = 10log_{10}(I/\langle I \rangle)$, and its variance σ_ι^2:

$$\sigma_\iota^2 = \langle \iota^2 \rangle - \langle \iota \rangle^2 \tag{2.9}$$

Examples of MCPE and observed timefronts are shown in figure 2.10. At some depths the paths ID+4, ID-4, and ID+5 were not sufficiently separated in time from other paths to allow windowing; these paths are excluded at those depths. The subsets of depths for which it was possible to separate particular arrivals differed slightly between the simulations and measured datasets. It is for this reason that results for histograms, SI, and σ_ι^2 will not be shown at all depths.

Confidence intervals for the TI MCPE simulation are more easily computed than for the experimental data and TD MCPE because all samples in the TI simulation are independent—while the experimental data and the TD MCPE have temporal correlations. For a given hydrophone depth, the set of 226 TI MCPE-derived intensity samples was resampled with replacement to create new sample sets of the same size as the original 1000 times. The SI was computed from each new set and the resulting estimates ordered from smallest to largest. The absolute difference between the 25^{th} ordered estimate(the 2.5 % percentile) and the original estimate and the difference between the 975^{th} ordered estimate (the 97.5 % percentile) and the original are averaged to give the 95 % confidence interval. In the case of the experimental data, the standard error was estimated by block bootstrapping (Davison and Hinkley, 1997) with a fixed block size of 400, using the sample variance of the bootstrap sample (Cojbasic and Tomovic, 2007). The standard error was then scaled assuming an asymptotic Gaussian distribution to give the 95 % confidence interval. Confidence intervals were computed identically for the variance of log-intensity, σ_ι^2.

A comparison of observations and MCPE predictions for the SI and σ_ι^2 appear in

figure 2.11. The MCPE and data 95 % confidence intervals on the SI and σ_ι^2 overlap for ID+4, ID-4, and ID+5 at all hydrophone depths. The confidence intervals for data and simulation overlap for ID-3 for depths shallower than 1150 m, though the prediction is consistently slightly smaller than the measured value. The confidence intervals do not overlap for ID-3 for hydrophone depths deeper than 1150 m.

Histograms of observed and modeled $I/\langle I\rangle$ at all hydrophone depths are shown in figure 2.12. Intensities at each depth were sorted into bins with a width of 0.05, and with bin edges ranging from 0 to 3.5. The resulting histogram counts were normalized by the total number of intensities recorded at that depth. For reference, 5 % and 1 % represent counts of 785 and 157, respectively, for the measured data, and 240 and 48, respectively, for the simulated data.

The distributions of measured intensities exhibit depth-dependence and structure that appear to be consistent across multiple hydrophones. The distribution at several depths around 1300 m appears to be bi-modal for ID+4; the same is true at 725 m for ID-4, and at various depths for ID+5. The mode of the distributions of ID-3 are shifted increasingly with depth toward low intensities for hydrophones below about 1150 m, and the distribution widens with depth, with more high intensities on the deeper hydrophones. The low-intensity mode of the ID-3 distribution is consistent with the intensity fading shown in the bottom panel of figure 2.4.

The distributions of the TD MCPE intensities are seen to be uni-modal for all four paths and at all depths for which paths could be separated. The MCPE distribution for ID-3 is noticeably narrower than for the other paths, apparent in the width of the light-blue portion of the histograms—as well as having a mode at a slightly higher intensity. The MCPE histograms appear otherwise to be quite similar to each other over the full range of receiver depths.

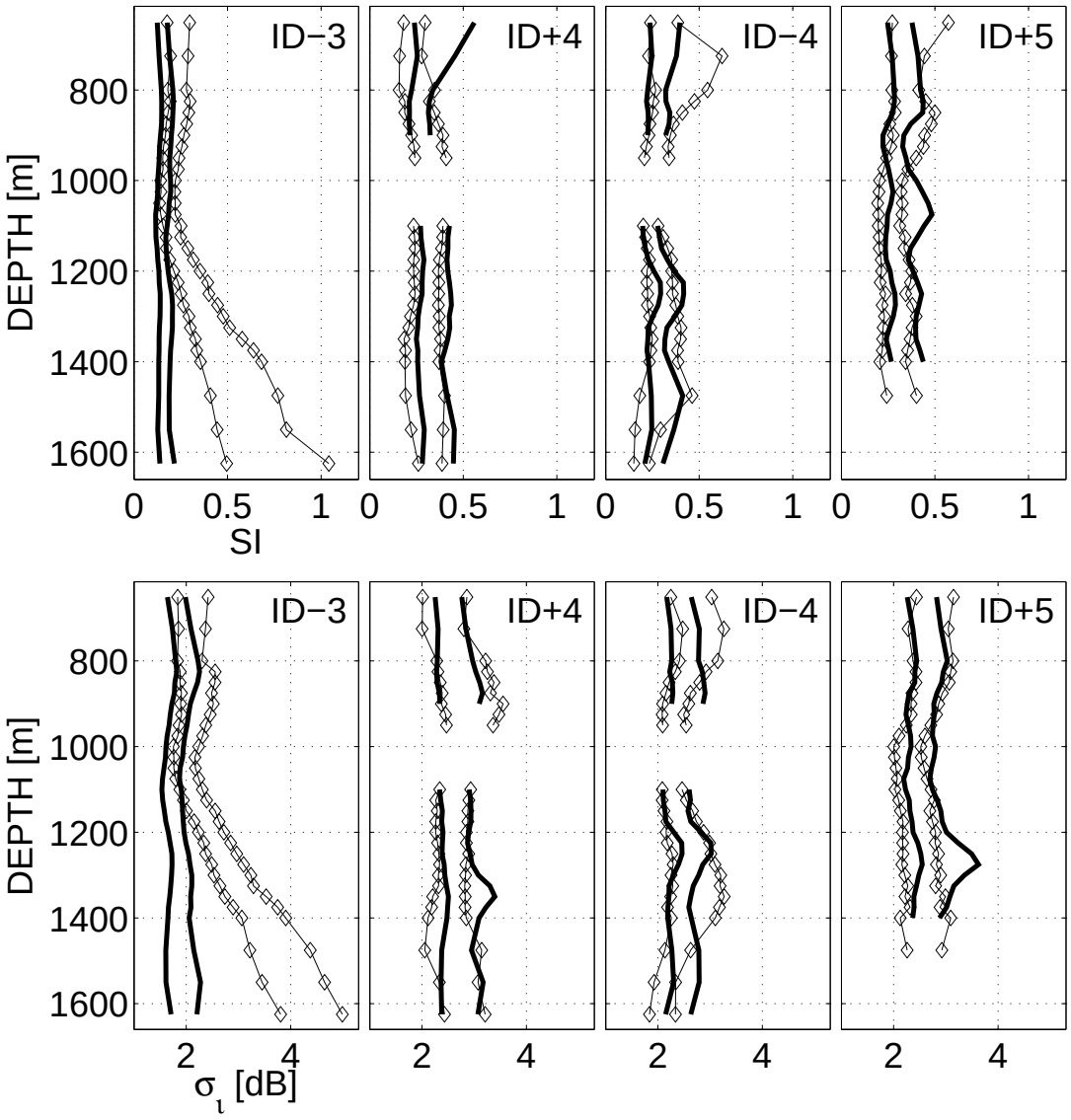

Figure 2.11: Top row: comparison of TI MCPE predictions of SI with measured values. The curves give the 2.5 % and 97.5 % percentiles—hence the 95 % confidence intervals. Bold curves show the MCPE confidence intervals and curves with diamonds show confidence intervals on the measured values. Diamonds indicate the depths at which the measurements were made. The bottom row shows the same for σ_ι.

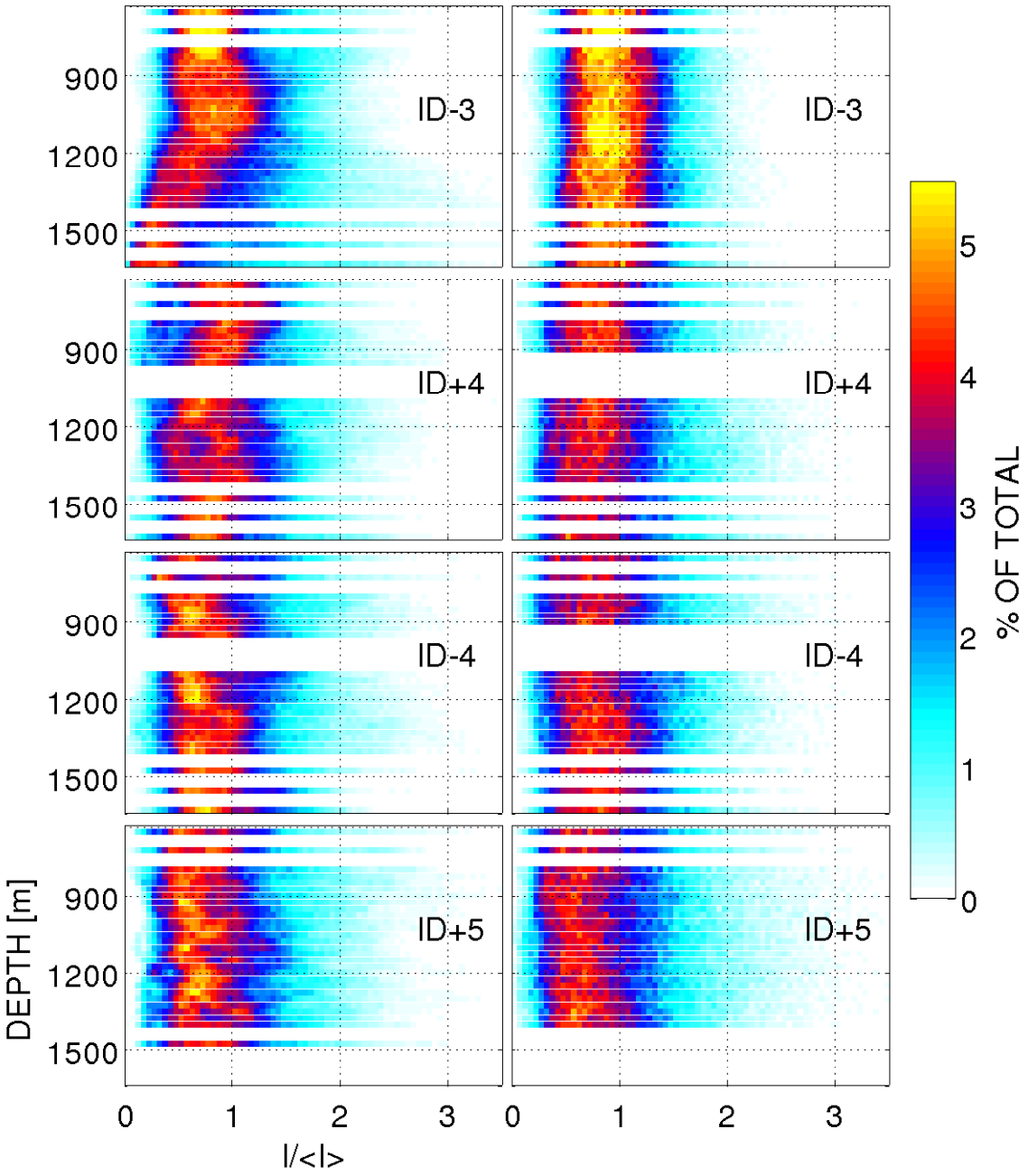

Figure 2.12: Shown in the left column are normalized histograms of $I/\langle I \rangle$ from the experiment. Shown in the right column are the same from the TD MCPE. Approximately 15 700 samples are included in the histograms at each depth for the measured data, while 4800 samples were included at each depth in the TD MCPE histograms.

2.5 Discussion

The SI and σ_ι^2 predictions for paths ID+4, ID-4, and ID+5 are not different from each other by a statistically significant amount. The predictions for path ID-3 are lower than for the other three paths. The same fluctuation measures of the observed intensities for paths ID+4, ID-4, and ID+5, which had 2, 2, and 3 UTPs, respectively, at depths from 260 m to 451 m, were also in agreement with each other. Path ID-3 had one UTP at depths between 53 m to 126 m, with the shallowest-turning paths reaching the deepest hydrophones on the upper array. At hydrophone depths shallower than 1150 m, the upper bound of the confidence interval on the SI is only slightly greater than the lower bound for paths ID-4 and ID+5, but compares better with path ID+4. For hydrophone depths greater than 1150 m in path ID-3, there is clearly some other modulating process in the intensity record that causes it to look qualitatively different than for all other paths. It is not clear whether the number of UTP can be said to affect the strength of the intensity fluctuations in the measured data, given the relatively small differences in SI and σ_ι^2 between the various paths—and the possibly significant differences in UTP depth (see table 2.1).

The MCPE model predicts the SI and σ_ι^2 quite well for paths ID+4, ID-4, and ID+5 at hydrophones from 651 m to 1625 m depth. The model differs from the observations in that it does not predict these same measures of intensity fluctuations for path ID-3 for hydrophone depths 1150 m and deeper, and somewhat under-predicts the variability at the shallower hydrophones for that path.

The MCPE distributions of $I/\langle I\rangle$ are similar to those of the measured intensity in the location of the distribution mode for most hydrophone depths, though the measured data exhibit some depth dependence of this mode location. The distributions of the measured data were bi-modal at some depths, while the simulated data had uni-modal distributions. Finally, the high-intensity tails of the measured data

extended out further for path ID-3 at depths where fades were observed than for the shallower depths. The length of the measured time-series was only about 60 h, while the TD MCPE time-series were 320 h in duration; it seems possible that this could be related to the greater depth-dependence and structure seen in the distributions of the measured data; i.e. the inclusion of more cycles of the long-period variability could "smear out" the distributions of the measured data.

The choice of model GM strength seems an unlikely explanation for the data/model differences: indeed, an identical MCPE simulation with a GM strength near 4.6 (not shown here) did not predict a SI as large as that observed for path ID-3—while the same simulation over-predicts the SI for paths ID+4 and ID-4 by about a factor of three.

Ray-tracing through the background sound-speed profile indicated that acoustic paths with a shallow UTP near 60 m would turn below the average mixed-layer depth seen in the 19 CTD casts. The vertical Fresnel zone around that shallow-turning ray, however, extends vertically from 10 m to 100 m depth at the upper turning point—allowing for the possibility that this acoustic path interacted with the mixed layer. This may introduce a long-timescale (diurnal) modulation that is not part of a standard GM internal-wave model. No attempt was made to include a mixed layer in the MCPE model, as the primary processes that drive the mixed-layer depth (Soloviev and Lukas, 2006) are not encompassed by the GM model.

An observation that could be related to the deep fades is that the 3 or 4 shallowest microCATs on the DVLA (shown in figure 2.6) showed an increase in sound speed near YD 110, followed by a decrease, and then a period of very little fluctuation from YD 112 to YD 122 or 123—despite large variability measured by the deeper sensors during that same period of time. These features coincide with the westward motion past the DVLA of the warm mesoscale feature, visible just to the southwest

of it in figure 2.1 (the westward motion is apparent from additional SSH maps from AVISO at 7-day intervals, but that are not shown here). This lack of sound-speed fluctuations in the upper ocean from YD 112 to YD 122 would seem to indicate that the water at those depths was well-mixed, or at least that the vertical gradient of sound speed was diminished during that period of time. The changing positions of mesoscale features may be related to this apparent change in the amount of vertical displacement observed by those shallowest sensors.

Simulations of a random eddy field with an assumed spectrum have been performed by Freitas (2008) and indicate that the presence of eddies can have a significant impact on acoustic propagation; in particular, she concluded that the eddy field caused acoustic energy to become trapped in surface ducts, caused shifts in horizontal and vertical convergence zone position, and caused convergence zone spreading. It is apparent from the temperature measurements shown in figure 2.5 that there is a strong large-scale range-dependence to the sound speed profile. It is difficult to say from the work presented here whether the presence of mesoscale eddies has had an effect on the intensity. The good data-model agreement for arrivals with UTP between 260 m to 451 m would suggest that the effect was not significant for those paths—but the cause of the deep fades in path ID-3 requires further study.

Peaks at tidal frequencies are prominent in the spectrum of sound speed variability measured by the CTD sensors on the DVLA. Further evidence of the time-dependence of the large-scale sound-speed field appears in the XBT transects shown in figure 2.5. Some transects overlapped in latitude, for example near 21.6° N, and a decrease in temperature is apparent—though the time elapsed between the transects does not allow one to infer much about the timescale of that variability.

An important feature of the observed deep fades is the time-dependence. Two and possibly part of a third deep fade are visible in the 1550 m time-series shown in

the bottom panel of figure 2.4. The intensity appears, roughly, to have a 5 dB fade during yearday 117, a 10 dB fade during yearday 118, and another 10 dB fade during yearday 119. The character of these fades is not sinusoidal, making it difficult to identify a particular periodicity, especially given only two clearly recognizable 10 dB fading events. It seems possible that the timescale is related to the observed strong local internal tides (Colosi et al., 2013).

The MCPE modeling presented in this report has made the assumption that the GM spectrum is an accurate representation of sound-speed fluctuations in the Philippine Sea. It is possible that the model-data discrepancy for paths turning in the extreme upper ocean is due to disagreement with the GM spectrum there, but the similarity to tidal timescales of the deep fades would seem to at least partially implicate the local internal tides.

Construction of a model or models that address the mesoscale variability and/or internal tides go beyond the MCPE approach taken here, however, which has made the assumption of a range-independent background sound-speed profile. Attempts to include range-dependence in MCPE models are not unheard of; Wolfson and Spiesberger (1999) included a range-dependent background, for example, in a study of a long-range experiment.

2.6 Conclusions

Despite the simplification of range-independence and the exclusion of internal tides from MCPE model simulations, the predictions of the SI, σ_ι^2, and the distribution of $I/\langle I\rangle$ for paths with UTPs below the extreme upper ocean generally agree with observations—the only model adjustment made was of the GM strength. This conclusion is in agreement with the results presented in Colosi et al. (2013) (to the extent that the MCPE model provides a validation of the ocean model), who stud-

ied the PhilSea09 environmental measurements more extensively. Their results were consistent with the GM spectral model's assumptions of horizontal isotropy and homogeneity (for diffuse internal waves), and they conclude that the GM spectrum could be used as an input to acoustic fluctuation calculations. The measures of intensity fluctuations studied here, the SI and σ_ι^2, did not appear to be strongly influenced by the number of UTPs in the path—though a compensating effect due to differences in UTP depth cannot be ruled out. Some of the differences between the distributions of the simulated and measured intensities may be due to the shorter duration of the measured time-series; an experiment with a longer duration would be required to resolve the ambiguity. Enhanced variability in the form of long-period deep fades is observed for paths turning in the extreme upper ocean; this enhanced variability is not predicted by the MCPE model employed here, and will be the subject of a follow-on report.

2.7 Acknowledgments

This work was supported by the the Long Range/Deep Water Propagation thrust area of the Ocean Acoustics Program at the Office of Naval Research under APL/UW grants N00014-08-1-0843 and N00014-08-1-0200, Scripps Institution of Oceanography grant N00014-08-1-0840 and Naval Postgraduate School grant N00014-11-WR20115.

2.8 Appendix A: PE model and convergence tests

The NSPE was chosen because it provides test cases and is actively maintained by the U.S. Navy. The code includes an implementation of a split-step Fourier (Tappert, 1977) algorithm, and an implementation of a split-step Padé algorithm derived from RAM (the Range-dependent Acoustic Model (Collins, 1993)). We used the split-step Padé version. The NSPE is capable of propagation through a range-dependent sound-

speed field such as that of an internal-wave perturbed ocean model environment. The angle between the horizontal and the direction of acoustic paths leaving the source was well within the limits for this PE.

Convergence tests were performed on the number of modes used in the internal wave simulator and on the range-step taken in the PE code. Features in the sound speed field that are much smaller than the acoustic wavelength will have a negligible effect on the propagation of acoustic waves; see e.g. Hegewisch et al. (2005). The criterion used to determine convergence was the normalized sum of squared errors

$$e_m = \frac{\sum_{i=1}^{n}(p_{m+10}(t_i) - p_m(t_i))^2}{\sum_{i=1}^{n}(p_m(t_i))^2} \tag{2.10}$$

where $p(t_i)$ is the n-point real pressure time-series computed by propagation of a broadband acoustic signal through a single instance of a GM internal wave perturbed random ocean composed of m modes. This measure of convergence fell to a value of $10 \cdot log_{10}(e_m) = -30$, or 0.1 % when 200 vertical internal wave modes were included in the random ocean. A similar metric was used to determine convergence for range-step, except that the range-step was halved each time. A value of -30 was reached when the range-step was 25 m.

10 Padé coefficients were retained in order to avoid performing an additional convergence test on the number of coefficients.

2.9 Note about references

The reference list for this chapter, as it appears in the submitted-paper version, has been merged into the thesis bibliography in section 5.2.

Chapter 3

TIME-DEPENDENT MEASURES

3.1 Temporal fluctuation measures

In this chapter, we will examine further the time-dependent (TD) MCPE modeling effort that was described in section 2.3.2. The purpose of the TD simulation was to test the predictive capability, for measures of temporal variability, of a time-evolving internal-wave-perturbed environmental model against measurements made during PhilSea09. The "background" or diffuse internal waves are assumed to be a stationary process that is described by the GM spectrum. The variability that these internal waves impart to the ocean's sound speed result in intensity fluctuations that are a function of time, and which could be described by some spectrum. In this chapter we make predictions of the power spectral density (PSD) and corresponding temporal auto-correlation functions of the intensity fluctuations measured during PhilSea09 for one of the hydrophone depths from PhilSea09; the predictions for the rest of the 30 hydrophone depths appear in appendix D.

The task of computing a prediction of the spectrum of intensity fluctuations from the simulated time-series is straightforward; making an estimate of the same quantity from the measured data is complicated by both planned and unplanned gaps in the measured time-series. This "gappy-data" problem is not completely solved in this thesis, though efforts are made to assess the viability of a couple of potential methods that could be used to compute these estimates. At least one further alternative solution to the problem exists (Bronez, 1988), though implementation of that solution and comparison to the methods studied in this chapter are left as future work. It was tractable to compare a couple of methods for computing the PSD using the time-series from only one of the available hydrophone depths—and in the future to compare those results with the alternative solution from Bronez (1988) before computing estimates at the remainder of the hydrophone depths.

Section 3.1.1 describes the specific measures of temporal variability considered

in this chapter. Measured and simulated intensity time-series at all 30 hydrophone depths will be presented in section 3.1.2. A qualitative comparison is made. A brief description of lowess trends that were estimated from a subset of measured and simulated time-series to be used throughout the rest of this chapter appears in section 3.1.4. Section 3.2 describes efforts to understand the gaps' effect on the spectral estimates, including a Monte Carlo approach involving an auto-regressive (AR) model, presented in section 3.2.1, and an introduction of the gaps into the TD MCPE-simulated time-series is presented in section 3.2.2. Finally we will discuss the implications of the gap-effect study in sections 3.4 and 3.5.

3.1.1 Power spectral density and the temporal autocorrelation function

Following Bendat and Piersol (1986), the power spectral (also called autospectral) density function S_{xx} is defined for a stationary random process $\{x(t)\}$ by the expression

$$S_{xx}(f) = \lim_{T\to\infty} E[\widehat{S_{xx}}(f,T,k)]$$

where $\widehat{S_{xx}}(f,T,k)$ is an estimate from the k_{th} sample record $x_k(t)$ of length T of that process, and $E[\,]$ represents the expected value over ensemble index k. S_{xx} is defined for frequencies $-\infty < f < \infty$, and is related to the auto-correlation function R_{xx} by Fourier transform

$$S_{xx}(f) = \int_{-\infty}^{\infty} R_{xx}(\tau) e^{-j2\pi f\tau} \mathrm{d}\tau$$

The one-sided power spectral density function G_{xx} is defined for $f \geq 0$. G_{xx} is related to the autocorrelation function, R_{xx}, by

$$G_{xx}(f) = 4\int_{0}^{\infty} R_{xx}(\tau) cos(2\pi f\tau)\, \mathrm{d}\tau$$

(limits of integration reflect the symmetry of R_{xx}) and vice versa

$$R_{xx}(\tau) = \int_0^\infty G_{xx}(\tau)\cos(2\pi f\tau)\,\mathrm{d}\tau \tag{3.1}$$

In this work, estimates $\widehat{G_{xx}}(f)$ of the one-sided PSD are made via the multi-taper method (MTM) (cf. Percival and Walden (1993)), and the discrete form of equation (3.1) is used to estimate the autocorrelation function.

3.1.2 Measured and TD MCPE intensity time-series

Pressure time-series were recorded on the 30 hydrophones of the upper sub-array of the DVLA and were processed in the manner described in this section. Hydrophones provided continuous sampling throughout each hour at a rate of 1953.125 samples/s, with a small gap at the end of each hour to allow for acoustic tracking of the DVLA. The hydrophone records were resampled at a rate that was four times the 284.166 666 Hz carrier-frequency used in transmissions, in preparation for pulse-compression. (The m-sequence signals used in the PhilSea09 experiment were discussed in section 1.1, and further in appendix A.) Data were separated into 7.2 s-long sections, (referred to here as "receptions"), which were post-equalized as was described in section 2.2.1, and then pulse-compressed.

Outlier removal for the hydrophone records obtained during PhilSea09 consisted of several steps. A mask of bits that corresponded to reception times was constructed, with either a "1" or a "0" indicating whether data was to be included or excluded, respectively, from the analysis. All bits corresponding to receptions that were recorded at times that the transmitter was not transmitting were set to "0". All full-power transmissions were preceded by a "ramp-up", or gradual increase, in signal level for marine-mammal protection; receptions made during "ramp-up" times were also excluded. Malfunction and overheating of the power amplifier that was being tested

during PhilSea09 caused signal drop-outs and glitches; these problems were diagnosed later with the use of records of voltage and current that were made throughout the experiment. Data that were affected by these problems were excluded.

Sonar signals of unknown origin occurred at regular intervals throughout most of the experiment, and were loud enough within the transmitted signal's frequency band to necessitate exclusion of receptions made during the times at which they occurred. Spectrograms were computed at the 1550 m hydrophone depth for each recorded hour, allowing for identification of the times when the contaminating sonar signal was in the water. The sonar signals consisted of upward or downward sweeps in frequency, followed by a single tone, and ending with another set of upward or downward sweeps in frequency. A list of reception times at which the central single-tone portion of the signal occurred was saved in a file. There were several variants of the sonar signal, and a window of appropriate length was designed for each one; a label denoting the signal variant was also saved for each observation of the signal. Receptions that were made during the window of time around each observation were excluded.

The overheating problem was noticed early on in the experiment and was dealt with by changing the planned transmission schedule to limit the length of each transmission—effectively inserting further gaps into the time-series (in addition to the gap in the hydrophone record at the end of each hour and the sonar signal contamination).

Each reception consisted of various numbers of arrivals—each corresponding to the individual path taken by the associated wavefront. The terminology used to describe these paths was defined previously, in section 2.2.2. The particular paths considered in this thesis (ID-3, ID+4, ID-4, and ID+5) were individually windowed for each reception at each hydrophone. Variability of the arrival time, also called "wander", of individual paths occurs due to changes in the positions of the transmitter and

the receiving array, and due to propagation through the time-varying ocean medium. The first form of variability is considered to be a source of instrument-based noise, while the second form of variability is the observable in the field of ocean acoustic tomography. As it relates to the efforts in this thesis (which focus specifically on the intensity), wander is instead a hurdle to be overcome while attempting to window the individual acoustic paths for analysis. This problem was solved by stepping through the time-series at each hydrophone, and visually selecting windows that were valid for small subsets of receptions (the subsets being a set of times for which the travel-time didn't vary by much in comparison to the size of the window).

The noise level of the pulse-compressed data varied between hydrophones on the shallow array. The mean and standard deviation noise level in the 284 Hz Fourier component within a time window equal in length to 16 M-sequences were calculated. This averaging time was chosen based on the reasoning that $16\,\text{Mseq} \times 7.2\,\text{s/Mseq} \approx 120\,\text{s}$; this window is sufficiently short that an elevated noise level due to the passing of a ship would be detected. In a final check to ensure that only high-quality data were included in the analysis, all individual path arrivals were therefore required to have an intensity that was more than one standard deviation above the noise level of this running-mean window.

The time-series of intensity for all hydrophones on the upper array of the DVLA are shown in figures 3.1–3.4. ID-3 was received on all hydrophones of the upper array of the DVLA. The paths ID+4 and ID-4 were also received on all hydrophones, but are not separable in time at depths near the center of the sub-array. Path ID+5 could not be separated from later arrivals at the hydrophones located at 1550 m and 1625 m depth. The deep fades that were mentioned in section 2.2.2 are apparent in the bottom half of panel A at yeardays 118.5 and 119.25.

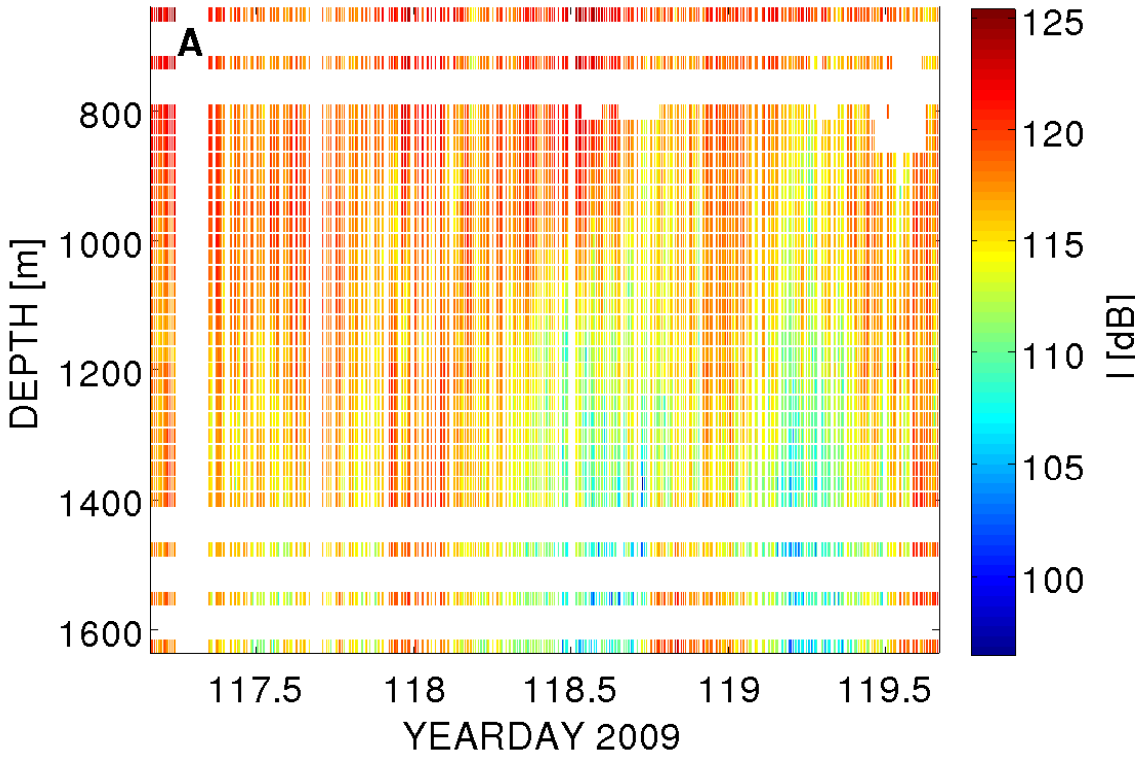

Figure 3.1: Measured intensities of all good receptions on the upper array of the DVLA for path ID-3. Intensity is represented by color in 22 m-wide bands in depth for clarity of presentation. At some of the shallowest hydrophones on the array, some further data were excluded—apparent here, and in figures 3.2– 3.4 as white patches.

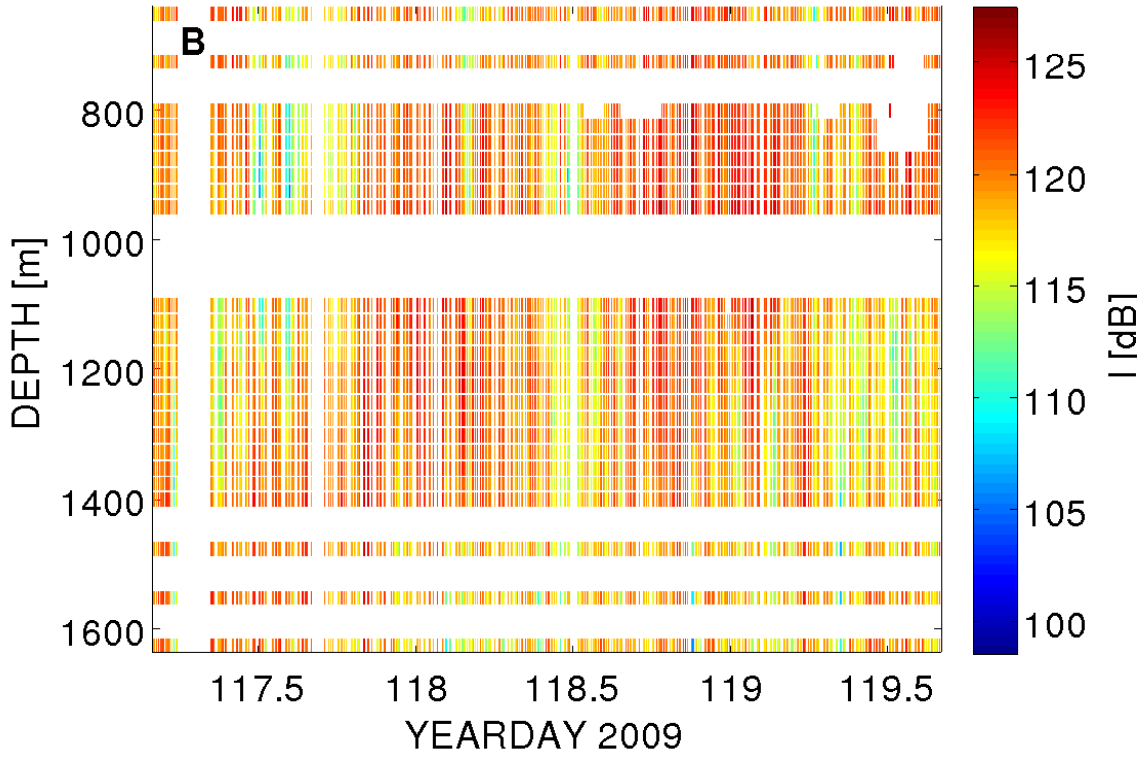

Figure 3.2: Measured intensities of all good receptions on the upper array of the DVLA for path ID+4. Intensity is represented by color in 22 m-wide bands in depth for clarity of presentation. At some of the shallowest hydrophones on the array, some further data were excluded—apparent as white patches. Not all arrivals were available at all hydrophone depths of the sub-array; it is for this reason that whole time-series are missing at several depths.

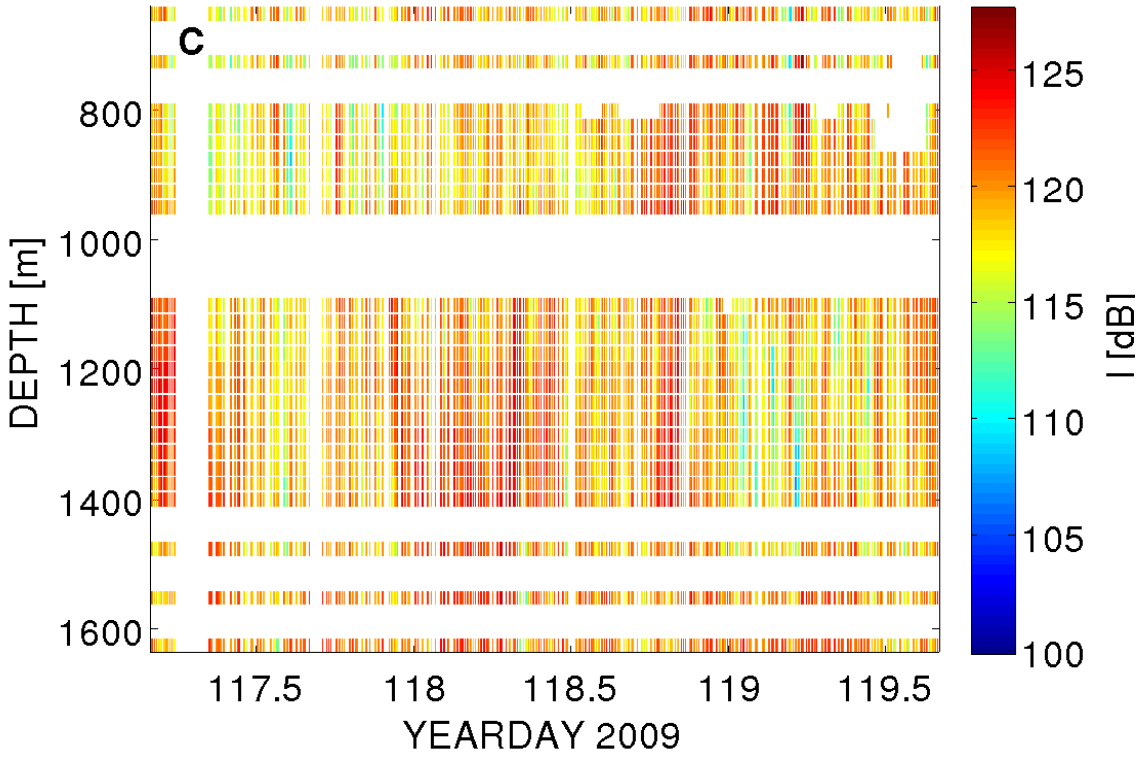

Figure 3.3: Measured intensities of all good receptions on the upper array of the DVLA for path ID-4. Intensity is represented by color in 22 m-wide bands in depth for clarity of presentation. Not all arrivals were available at all hydrophone depths of the sub-array; it is for this reason that whole time-series are missing at several depths. At some of the shallowest hydrophones on the array, some further data were excluded—apparent as white patches.

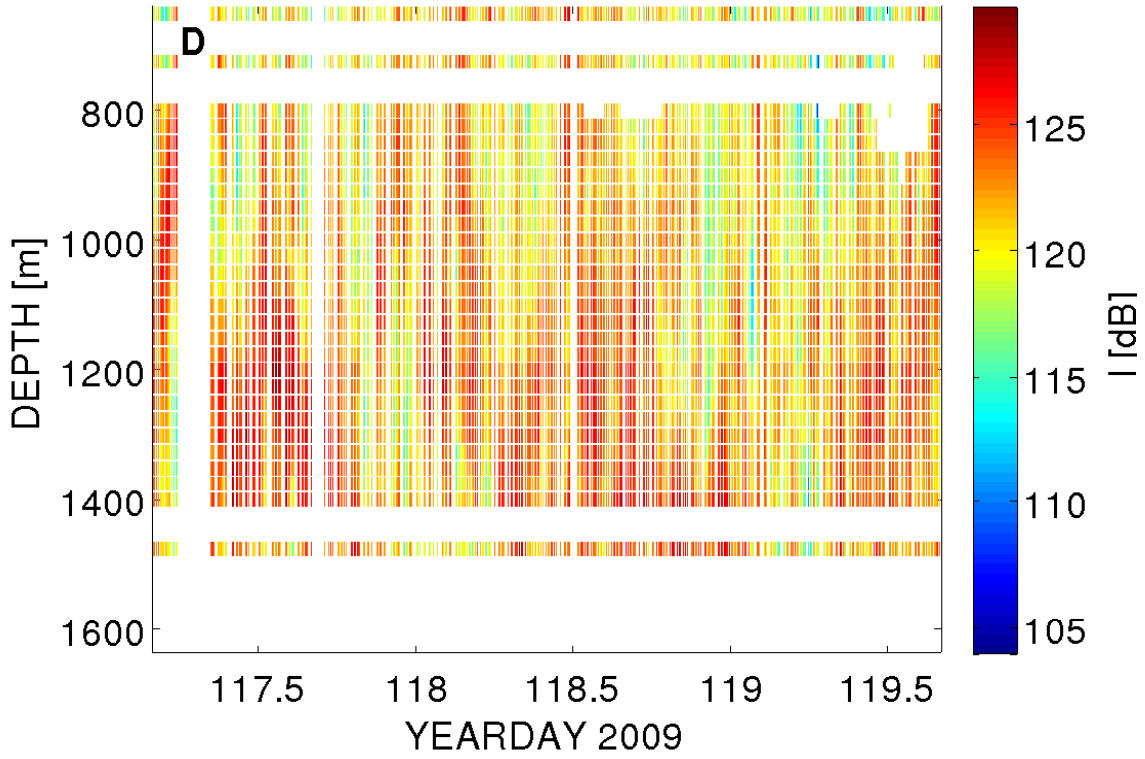

Figure 3.4: Measured intensities of all good receptions on the upper array of the DVLA for path ID-5. Not all arrivals were available at all hydrophone depths of the sub-array; it is for this reason that whole time-series are missing at several depths. At some of the shallowest hydrophones on the array, some further data were excluded—apparent as white patches.

3.1.3 Time-dependent MCPE simulation

Recall that the time-dependent model was identical to the time-independent model, except that instead of using random time-independent snapshots of the model environment as inputs to the NSPE model, a single instance of the internal-wave displacement field is evolved in time, with snapshots of the field made at regular intervals in time used as input to the NSPE model. The results of this simulation are time-series of intensity at 5505 depths with a 1 m spacing between depths, though only simulated data at the hydrophone depths used in PhilSea09 will be considered here. The time-step used in time-dependent modeling was 240 s and the time-series computed out to ten local inertial periods, or about 320 h.

60 h-long samples of the TD MCPE simulated intensity are shown in figures 3.5–3.8. The same problem of some arrivals being too close together in time occurs in the simulations, and explains the absence of time-series for some depths.

Figure 3.9 shows a typical comparison between the measured and simulated intensities. It is evident from the plots that the fluctuations are of similar magnitude and generally that the timescales of variability are also similar. Notice also that the difference in sample rate will somewhat limit the frequency range over which comparison will be possible. As seen in the bottom panel of the figure, there is some higher-frequency variability in the measured data of around a dB.

Given the lengths and sample rates of the measured and simulated time-series, the PSD may be predicted and estimated over two partially-overlapping bands of frequencies. The lengths of the time-series were 320 h and 60.134 h, respectively, for the simulated and measured data. The sample rates were 1/240 s and 1/7.2 s for the simulated and measured data, respectively. The frequency bands over which we estimate the PSD are 8.6×10^{-7} Hz to 2×10^{-3} Hz and 4.6×10^{-6} Hz to 6.9×10^{-2} Hz, respectively, for the simulated and measured data.

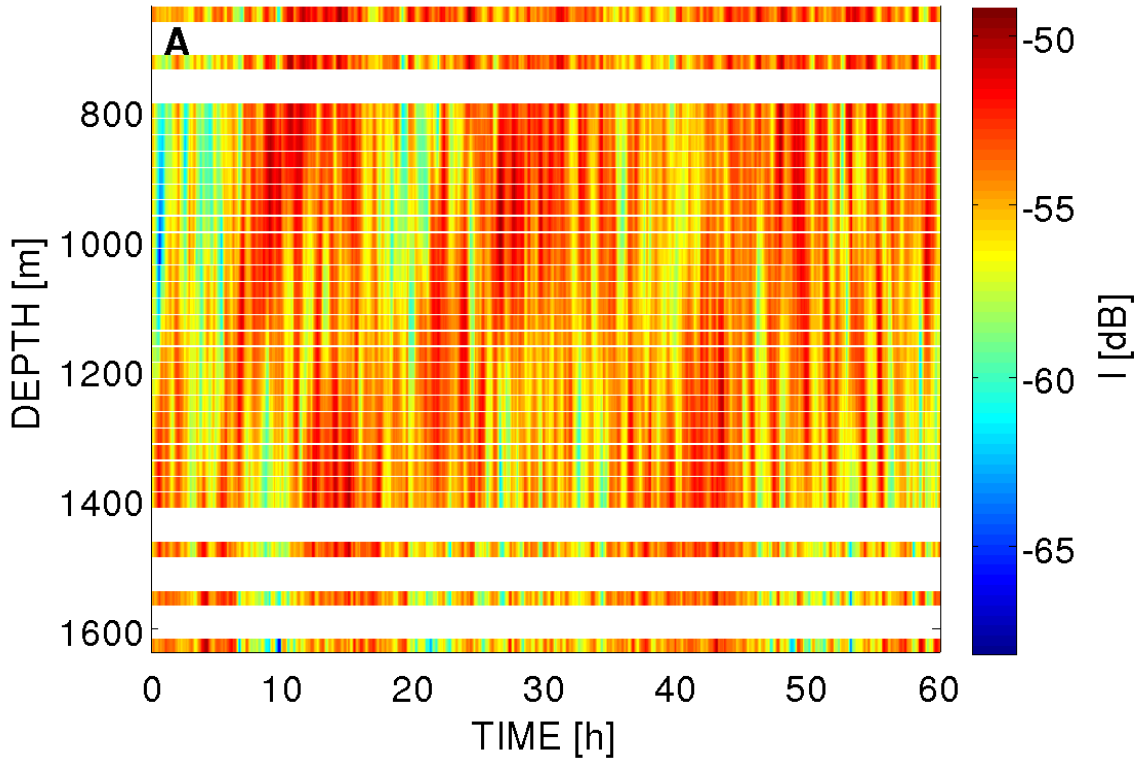

Figure 3.5: Shown here are 60 h out of the 320 h of simulated intensities of arrival ID-3. Time-series are computed at a vertical spacing of 1 m depth in the simulation, but only data at the hydrophone depths are shown here. Data have been spread over adjacent depths in the same way as was done in the plots of the measured data in figures 3.1–3.4.

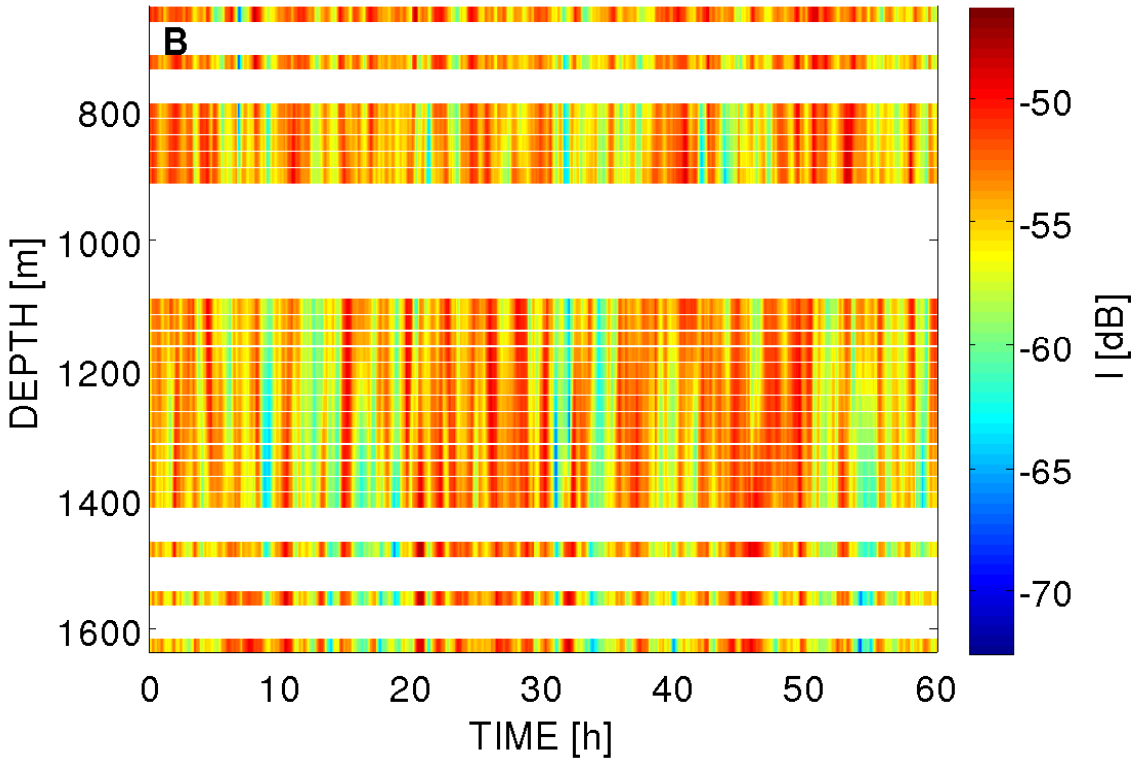

Figure 3.6: Shown here are 60 h out of the 320 h of simulated intensities of arrival ID+4. Time-series are computed at a vertical spacing of 1 m depth in the simulation, but only data at the hydrophone depths are shown here. Data have been spread over adjacent depths in the same way as was done in the plots of the measured data in figures 3.1–3.4.

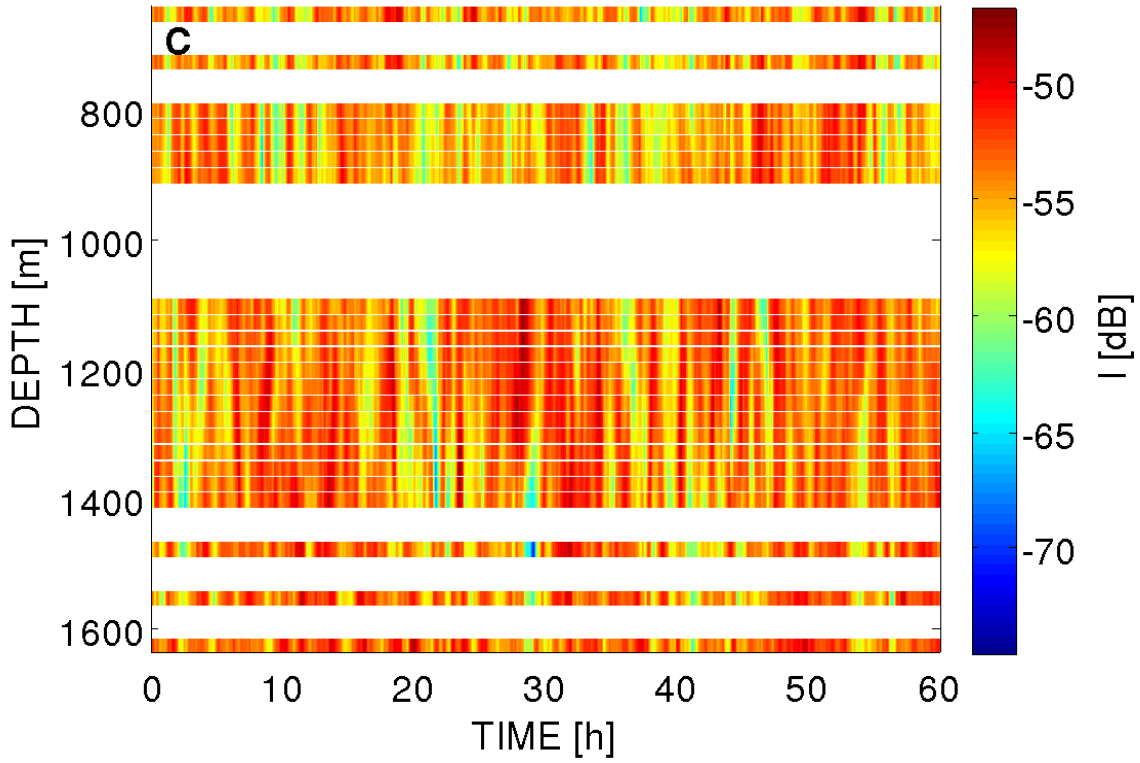

Figure 3.7: Shown here are 60 h out of the 320 h of simulated intensities of arrival ID-4. Time-series are computed at a vertical spacing of 1 m depth in the simulation, but only data at the hydrophone depths are shown here. Data have been spread over adjacent depths in the same way as was done in the plots of the measured data in figures 3.1–3.4.

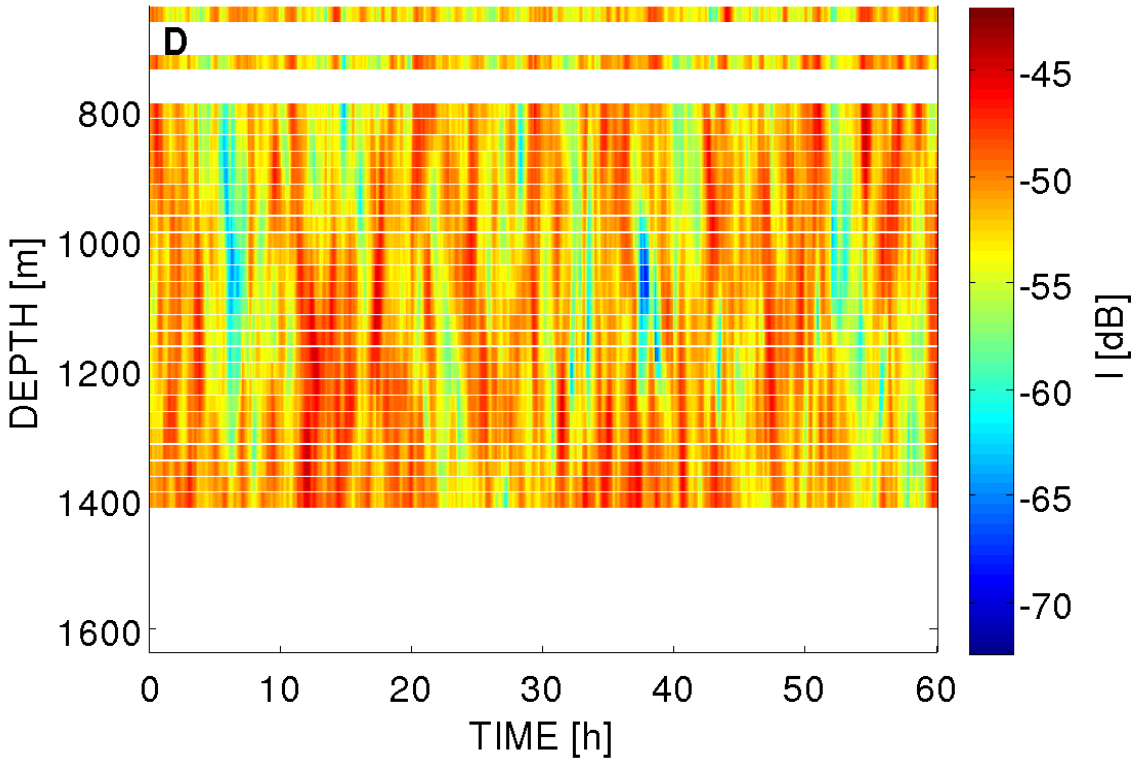

Figure 3.8: Shown here are 60 h out of the 320 h of simulated intensities of arrival ID-5. Time-series are computed at a vertical spacing of 1 m depth in the simulation, but only data at the hydrophone depths are shown here. Data have been spread over adjacent depths in the same way as was done in the plots of the measured data in figures 3.1–3.4.

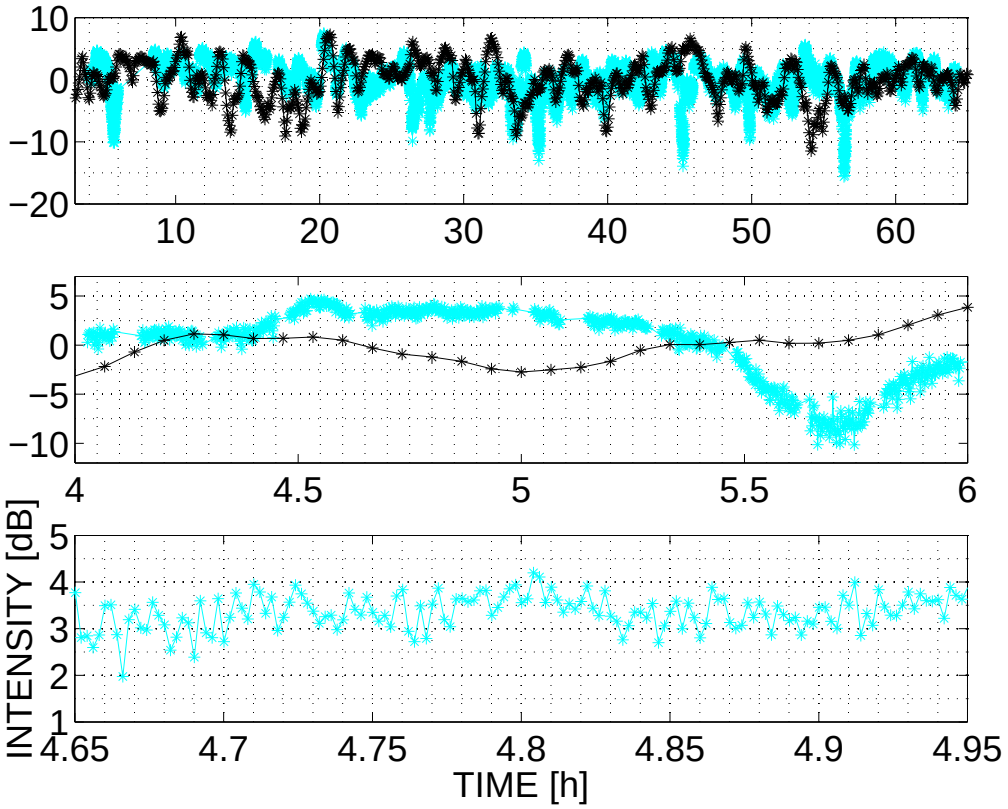

Figure 3.9: Comparison of typical fluctuations in measured vs. simulated intensities. In all panels, cyan symbols are the measured data; in the top and middle panels, the simulated data are shown with black symbols. The intensity record shown is that of ID+4 at 1550 m depth in all panels. Different timescales are shown in each panel, with the entire record for the measured intensities shown in the top panel.

3.1.4 Lowess trend

In attempting to compute estimates of the PSD from the measured intensity records, it was found that gaps in the transmission schedule caused different types of bias in the estimate. The first form of bias caused by these gaps was an elevated spectral level at high frequencies within the band of interest, and a diminished spectral level at low frequencies within the band. The second form of bias, noticeable mostly in the PSD estimates for ID-3 at hydrophone depths at which deep fades were observed, was an elevated spectral level at several frequencies related to the transmission schedule, apparent as "spikes" in the estimates.

The long timescale (about a day) of the fades, and their presence in only one of the acoustic paths suggests that they are due to some process other than the background internal waves; thus an attempt was made to separate the deep fades from the rest of the intensity fluctuations. It will be seen that this idea of separating the two supposed processes leads to a means of partial reduction of both forms of bias just described.

A lowess trend was computed for the ID-3 intensity recorded at 1550 m depth (shown previously in figure 2.4). The trend is shown in figure 3.10. Trends were also computed for the simulated ID-3 time-series at that depth, and for the measured and simulated ID+4 time-series at the same depth. These other trends are not shown, but are used throughout the remainder of the chapter in studying the gaps' effect on the PSD estimates. The trend in the measured 1550 m intensities makes apparent the deep fades observed on some of the deeper hydrophones for path ID-3. The other trends mentioned do not have this feature, but the trends are computed and used in all time-series for consistency in the remaining part of the analysis.

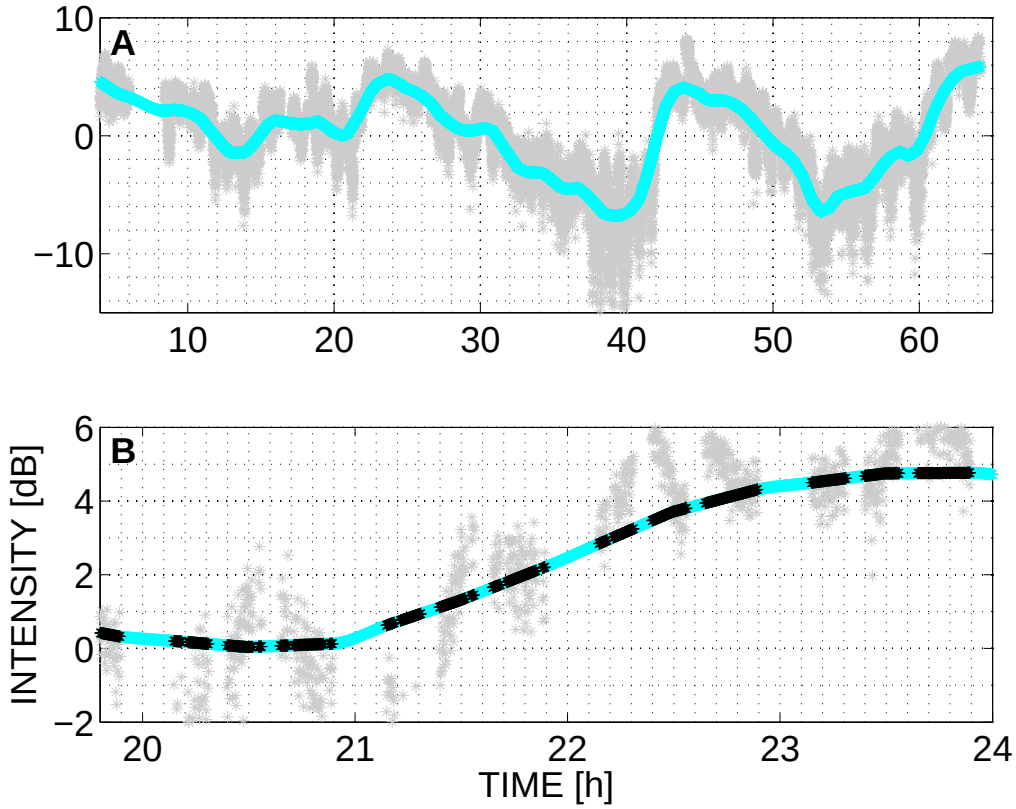

Figure 3.10: Panel A: Measured intensity time-series of ID-3 at 1550 m depth. All measured data are plotted as gray symbols; cyan symbols show the interpolated lowess trend. Panel B: same as panel A, except the additional black symbols show the lowess trend with gaps, and a smaller window in time is shown.

3.2 The effect of gaps

In this section, we will explore the effect of the gaps on the PSD estimates by considering two methods for computing the PSD: the first method uses an auto-regressive model and the second method uses the TD MCPE time-series as a model. Both methods will make use of the lowess trend described in the previous section.

3.2.1 AR model

Again following Bendat and Piersol (1986), consider a stationary random process $\{y(t)\}$ that is the sum of two stationary random processes $\{x_1(t)\}$ and $\{x_2(t)\}$ such that each sample function is of the form

$$y_k = a_1 x_{1,k}(t) + a_2 x_{2,k}(t), \tag{3.2}$$

where a_1 and a_2 are two arbitrary constants, then expressions for the spectrum G_{yy} and autocorrelation function R_{yy} are given by

$$G_{yy} = a_1^2 G_{x_1 x_1} + 2a_1 a_2 C_{x_1 x_2} + a_2^2 G_{x_2 x_2} \tag{3.3}$$

$$R_{yy} = a_1^2 R_{x_1 x_1} + a_1 a_2 [R_{x_1 x_2} + R_{x_2 x_1}] + a_2^2 R_{x_2 x_2} \tag{3.4}$$

$$C_{x_1 x_2} = 2Re[S_{x_1 x_2}] \tag{3.5}$$

where $C_{x_1 x_2}$ is the co-spectrum of processes $\{x_{1,k}(t)\}$ and $\{x_{2,k}(t)\}$, defined for frequencies $f > 0$. Equations (3.4) and (3.3) indicate that, even for our simple model of additive processes, we must consider possible correlations between the two processes—especially given that locally-generated internal tides (which could be the source of the

deep fades) are internal waves, and therefore probably influence what we model in the TD MCPE, for example, as the "background" internal waves.

We model the de-trended part of the ID-3 time-series as an AR(1) process

$$y_t = c_0 + c_1 y_{t-1} + \epsilon_t \tag{3.6}$$

where c_0 is a constant offset, set to zero, $c_1 = 0.9$, and ϵ is an independent and identically distributed, "i.i.d.", random variable. The advantage to creating a model is that we know what happened during the self-imposed "gaps in transmission" in the model, whereas for the data we do not. Instances of this model are computationally inexpensive to create (unlike a time-dependent MCPE time-series), which allows us to introduce the gaps and determine, via Monte-Carlo, what average effect these gaps have on our estimate of the PSD.

The method was as follows:

1. Generate a set ϵ_t of random numbers with the aforementioned properties
2. Use this to make one realization of the AR(1) model
3. Compute an estimate of the one-sided PSD of this realization
4. Introduce transmission schedule gaps into the realization
5. repeat step 3
6. save results and compare

These steps were repeated 2000 times each for each of three versions of the model, creating an ensemble for each version from which we compute an estimate of the average bias in the PSD that is caused by the transmission schedule.

The first model was the AR(1) process. This model was a time-series with a length equal to the time elapsed between the times of the first and last transmissions made during PhilSea09: a period of 60.134 h at 7.2 s intervals, giving 30 067 points. The same mask of "0"'s and "1"'s that was used to mark all measured intensities as either good or bad was then applied to the AR(1) time-series. In the case of this first model, points in the time-series marked as bad were set to a value of "0". The PSD was computed for the time-series with all of the points, and then for the time-series with the gaps.

The second model consisted of the lowess trend for the ID-3 1550 m depth intensity record plus the AR(1) process. In this model, when the gaps are imposed on the time-series, the data in the gaps is replaced by the value "0". The third model is the same as the second model, except that data in the gaps is replaced with the interpolated trend. Examples of the three models are shown in figure 3.11.

3.2.2 TD MCPE simulation

Our end goal is to understand what biases the gaps cause in the PSD estimates from the measured intensities. The AR(1) model has the advantage of being computationally inexpensive; the TD MCPE does not share this quality. The disadvantage to the AR(1) model is that its spectrum is significantly different from the spectra of either the TD MCPE or the measured intensity. The biases caused by the gaps depends on the spectrum of the underlying process. We can get some idea about how the spectrum of the TD MCPE would be affected by the transmission gaps by imposing those gaps on the TD MCPE time-series. The time-series is 320 h in length, as compared to the 60.134 h of PhilSea09 transmissions. In addition to this difference in record length, the sample rate of the measured data was 1/7.2 s and the TD MCPE sample rate was 1/240 s. The first problem is solved by simply repeating the

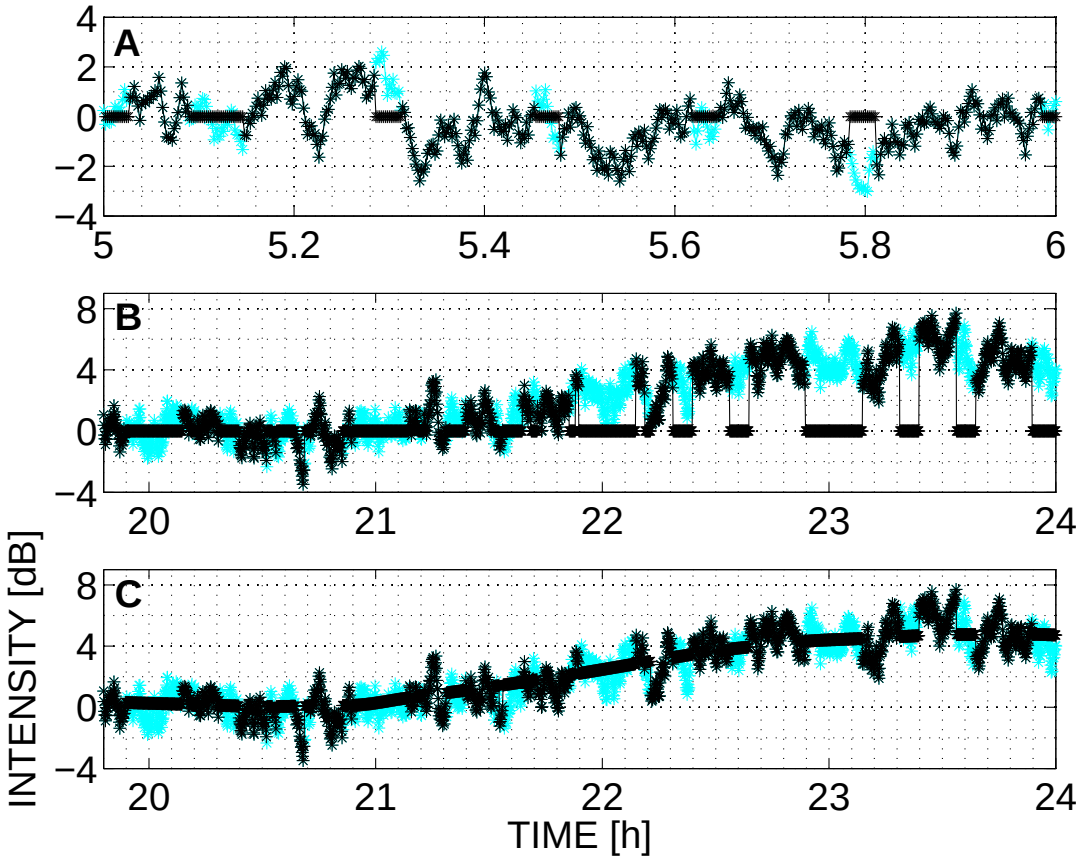

Figure 3.11: The three versions of a single realization of the AR(1) model. Panel A, B, and C show the first, second, and third models, respectively—as described in section 3.2.1. In all panels, the cyan (black) symbols show a particular model before (after) introduction of the gaps. Different subsets of the model time-series are shown in each case for clarity of presentation.

gap schedule until is has a length equal to the TD MCPE time-series. The second problem is solved by interpolating the TD MCPE time-series onto times that are 7.2 s apart. Gaps are filled either with "0"'s or with the interpolated lowess trend. The autocorrelation function R_{II} prediction for each of the modified time-series was computed as in equation (3.1). Results are shown in section 3.3.2.

3.3 Results

3.3.1 AR model

The results of the AR modeling are shown in figure 3.12. As can be seen in the plots labeled A and B, the effect of the transmission schedule on the AR(1) process is to lower the PSD by about two or three dB at all frequencies considered in this study. The effect of the transmission schedule on the trend is to introduce spikes at frequencies corresponding to $1/T$ where T corresponds to the lengths of the transmissions. Spikes also occur at frequencies of $1\,\mathrm{h}^{-1}$ and $0.5\,\mathrm{h}^{-1}$. The level of the trend's estimated PSD rises at high frequencies; presumably this is due to the energy added by sharp jumps and drops at the beginning and end of transmissions. This energy added at frequencies which exceed the Nyquist frequency are likely aliased back into the estimate.

When the trend in ID-3 is added to the AR(1) model (see figure 3.12, plots C and D), a frequency-dependent bias appears in the estimate of the PSD. At frequencies below 1×10^{-4} Hz, the PSD estimate is reduced by about six dB with introduction of the transmission schedule gaps. The reduction in the estimate decreases at intermediate frequencies. At higher frequencies ($1\,\mathrm{h}^{-1}$ and greater) the estimate shows large positive biases in the form of spikes at particular frequencies. The aliased energy which was apparent in the PSD estimate of the ID-3 trend appears to be far below the level of the PSD of the AR(1) model at high frequencies.

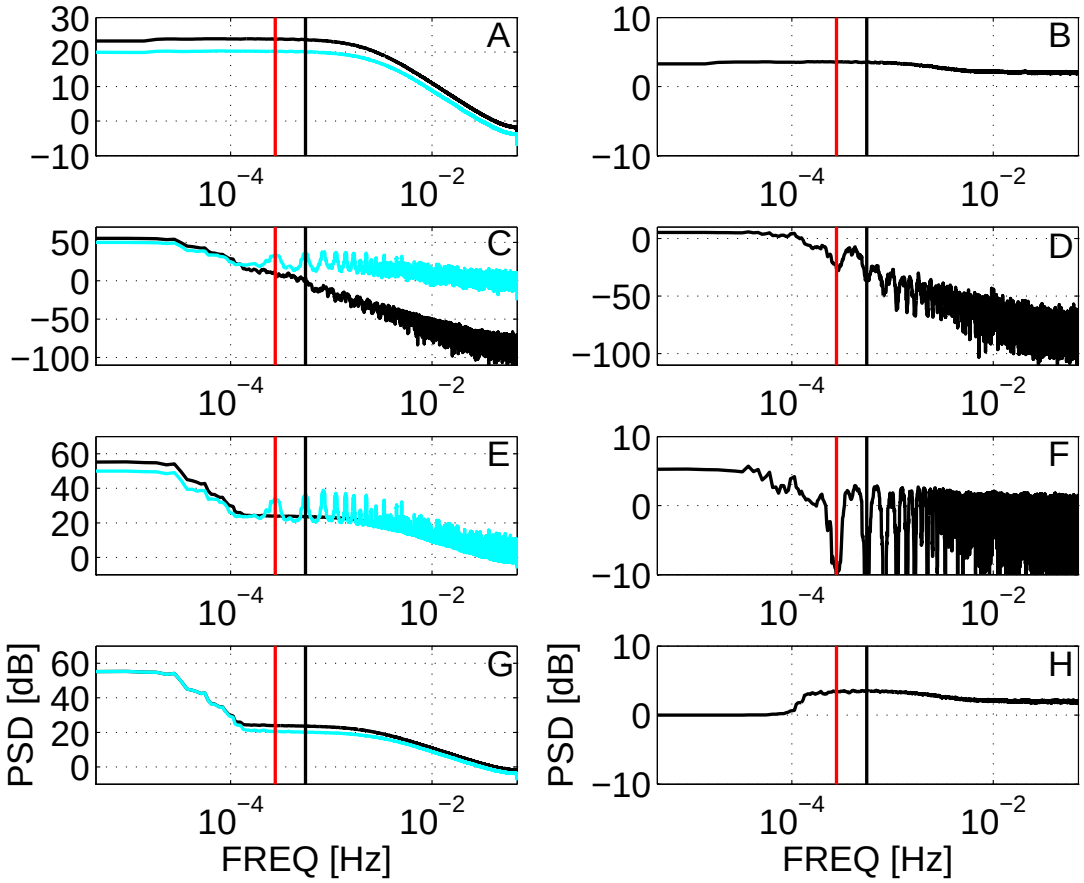

Figure 3.12: Comparisons of PSD estimates for measured and modeled data. Panel A shows the AR(1) model mean PSD estimate. Panel C shows the mean estimate for the ID-3 trend. Panel E shows the mean estimate for the model + interpolated trend. Panel G shows the mean estimate for the model + interpolated trend. In panels A, C, E, and G, the black curve is the model and the cyan curve is the same model with gaps due to the introduction of the transmission schedule. Panels B, D, F, and H show the black curve minus the cyan curve, i.e. model mean PSD estimate minus model-with-gaps mean PSD estimate. In panels G and H only, the interpolated trend replaced the model in the gaps for the cyan curve; in all other plots, the data in the gaps was set to a value of zero for the cyan curve. The vertical red and black lines in all plots show frequencies of $1\,\mathrm{h}^{-1}$ and $2\,\mathrm{h}^{-1}$, respectively, for reference. Notice that the abscissa axes differ between panels.

By interpolating the trend across the gaps (figure 3.12, plots G and H), we can see that the spikes due to the transmission schedule are substantially decreased. It is evident in figure 3.12 that the 6 dB reduction at low frequencies seen when the trend is not interpolated across the gaps becomes negligible. This is a reflection of the fact that our model without gaps *is* the interpolated trend. We can not know precisely how the lower frequencies are affected by the gaps due to the transmission schedule, however, the length of the majority of the gaps is much less than the period of the lower frequencies. The longest gap was two and a half hours, but the second-longest gap was around an hour in duration. These gaps may leak some energy into frequencies below 1×10^{-4} Hz (2.8 h period).

3.3.2 TD MCPE

The PSD predictions made from the modified simulated time-series are shown in figure 3.13 and 3.14. Introduction of "0"'s at the positions of the transmission gaps (figure 3.13) causes the predicted level to be decreased by between 4 dB to 6 dB from 1×10^{-6} Hz to 4×10^{-4} Hz. The prediction is increased at frequencies higher than 4×10^{-4} Hz. When the interpolated trend replaces the data in the transmission gaps (figure 3.14), the prediction is unaffected for frequencies below 5×10^{-5} Hz. Between frequencies of 5×10^{-5} Hz to 7×10^{-4} Hz, the prediction is decreased by as much as 6 dB—and for frequencies above 7×10^{-4} Hz the prediction is increased.

The autocorrelation function R_{II} predictions are shown in figures 3.15 and 3.16. When data in the gaps are replaced with "0"'s (figure 3.15), the autocorrelation function prediction is decreased at all lags shown in the figure. A small spike in correlation appears at a lag of one hour for the gappy time-series. The correlation time is decreased by a factor of two for both paths. When data in the gaps are replaced by the interpolated trend (figure 3.16), the prediction is decreased for lags

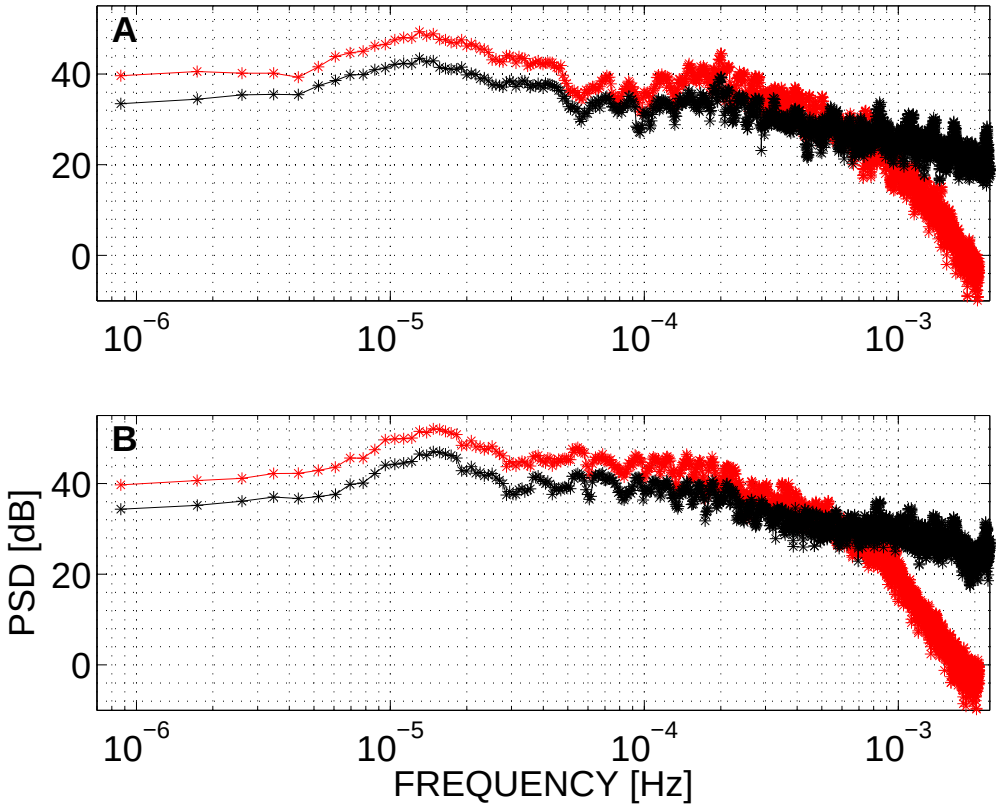

Figure 3.13: PSD predictions using synthetic MCPE data. The red curve shows the prediction from the original simulated data at 240 s intervals. The black curve shows the prediction when data occurring during the transmission gaps are set to a value of "0". Panel A: ID-3 at 1550 m depth. Panel B shows the same for ID+4.

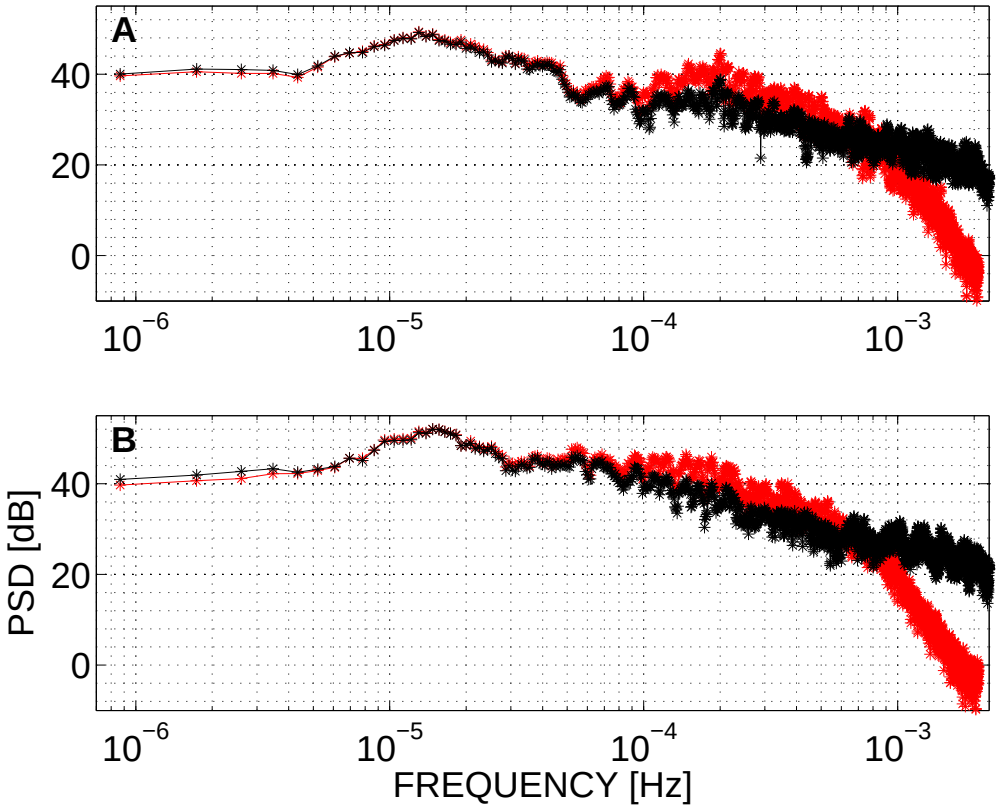

Figure 3.14: PSD predictions using synthetic MCPE data and trend-filled gaps. Same as figure 3.13, except that data occurring during transmission gaps are set to the interpolated trend values instead of being set to "0".

less than 10 min and increased for lags greater than 10 min. The predicted correlation time is increased from 20 min to 90 min for path ID-3, and increased from 25 min to 45 min for path ID+4. While a small spike in correlation appeared at a one-hour lag with the introduction of "0"'s into the gaps in figure 3.15, a small dip appears instead at the one-hour lag with introduction of the interpolated trend.

3.3.3 Measurements

Comparisons of estimates of the PSD from the measured data are shown in figure 3.17. When the measured data in the gaps are replaced with "0"'s, the estimate is lower than that in which the data is replaced with the interpolated trend for frequencies from 5×10^{-6} Hz to 1×10^{-4} Hz, for paths ID-3 and ID+4. At higher frequencies, the predictions are equal for both paths, except for the spikes at frequencies related to underlying periodicity of the gaps— which only appear in path ID-3. The spikes are reduced when the interpolated trend is used; the reduction is slight for the spike at $1\,\mathrm{h}^{-1}$, and increases as frequency increases. In path ID+4, the predictions are essentially equal above a frequency of 1×10^{-4} Hz.

A comparison between the prediction and estimate from measurement of the PSD is shown in figure 3.18. The prediction was made from the TD MCPE-simulated data, with gaps introduced and filled with the interpolated lowess trend. Paths ID-3 and ID+4 are shown. There is good agreement for frequencies above 3×10^{-5} Hz for path ID+4, and for frequencies above 1×10^{-4} Hz for path ID-3. Both PSD predictions reach a maximum level near a frequency of $1\,\mathrm{d}^{-1}$. In fact, this feature appears in the predictions for all paths at all depths considered in this thesis, as may be seen in appendix D. The PSD estimate from the measured data for path ID+4 does not have this maximum at $1\,\mathrm{d}^{-1}$, and appears to keep rising as frequency decreases. Path ID-3's PSD exceeds the prediction at frequencies below 1×10^{-4} hertz by up to

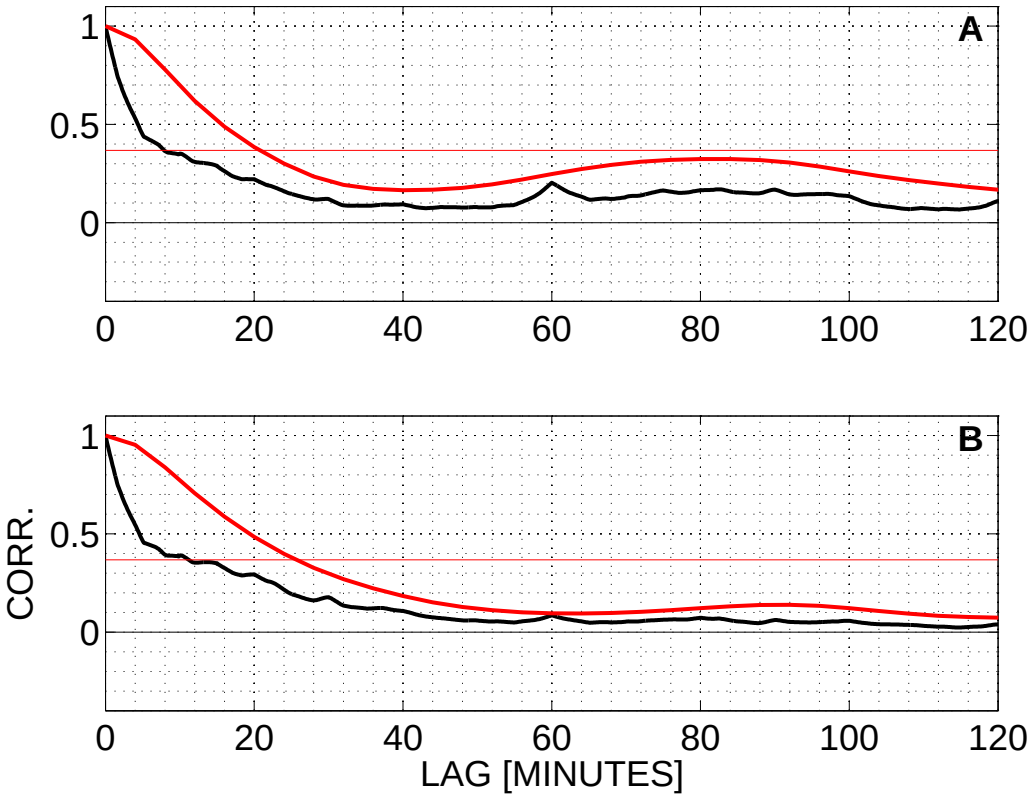

Figure 3.15: Intensity autocorrelation functions, synthetic MCPE data, zero-filled gaps. Panel A: R_{II} estimates for ID-3 at 1550 m depth. The red curve shows the estimate for the original simulated data at 240 s intervals. The black curve shows the estimate when data occurring during the transmission gaps are set to a value of "0". Panel B shows the same for ID+4. The red horizontal line shows the value of $1/e$ for reference. The correlation time is the smallest lag at which the autocorrelation function falls below this value.

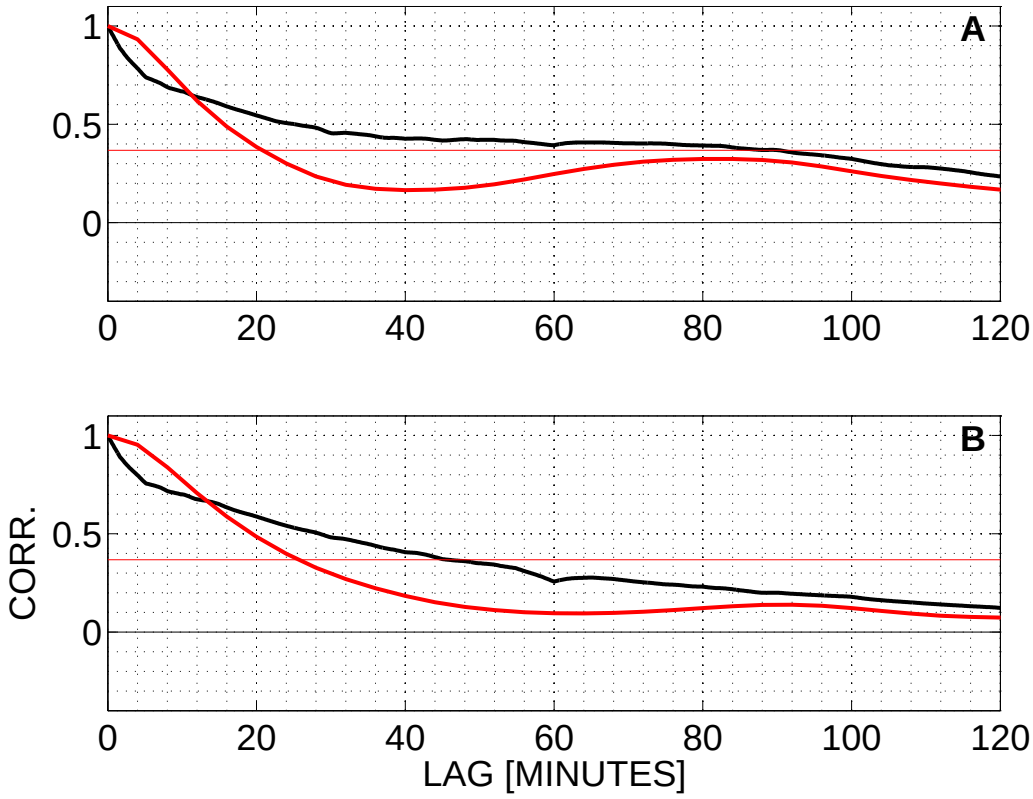

Figure 3.16: Intensity autocorrelation functions, synthetic MCPE data, interpolated-trend-filled gaps. Same as figure 3.15, except that data occurring during transmission gaps are set to the interpolated trend values instead of being set to "0".

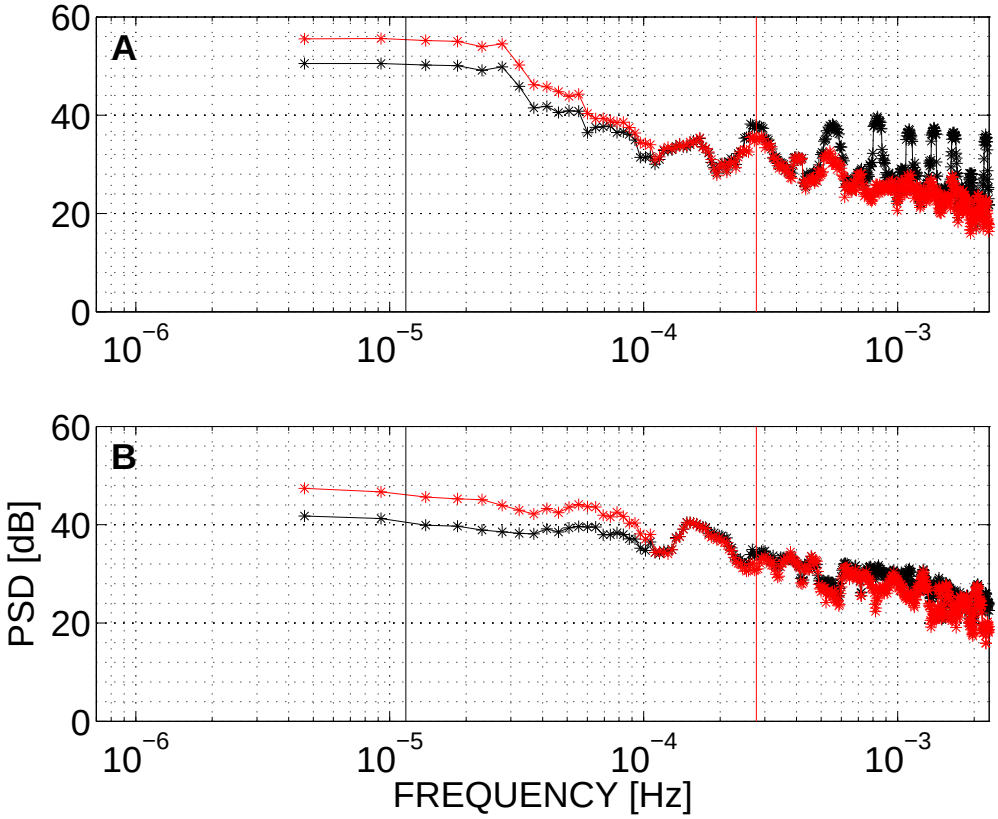

Figure 3.17: PSD estimates of measured data for ID-3 and ID+4 are shown in panels A and B, respectively, with missing data filled in with zeroes for the black curve and missing data filled in with the interpolated trend for the red curve. The black and red vertical lines show frequencies of $1\,\mathrm{d}^{-1}$ and $1\,\mathrm{h}^{-1}$, respectively, for reference.

nearly 16 dB at the lowest frequency shown, and is seen to be nearly flat for frequencies from 4.5×10^{-6} Hz to 3×10^{-5} Hz—though the small number of Fourier points means that a small amount of spectral leakage between the bins would conceal any underlying shape. Path ID+4's PSD is less than the predicted value for frequencies from 8×10^{-6} Hz to 3×10^{-5} Hz, and exceeds the prediction at the lowest frequency for which it can be calculated.

3.4 Discussion

While one may measure, and possibly attempt to model, the temporal variations in the ocean's sound speed, the relationship between these variations and their effect on the temporal characteristics of the acoustic intensity is not precisely known. The power spectral density gives a quantitative description of the energy content at various temporal frequencies for a given process. The variance of that process is the integral of the power spectral density over frequency. Models for calculating the PSD analytically do exist, e.g. Munk and Zachariasen (1976). This model, known as the Munk-Zachariasen (MZ) model is an adaptation of the Rytov (Rytov et al., 1989) weak-fluctuation theory. The MZ model employs the GM model as the description of environmental fluctuations. The main goal of the work presented in this thesis was to test whether the GM model would be a sufficient description for the purpose of predicting acoustic intensity fluctuations in the Philippine Sea, as it has been in other regions. The MZ model is based in a ray-theory framework, which makes some significant approximations, and therefore it was decided to take instead the full-wave approach provided by MCPE simulation—so as to not complicate the effort with any further approximations to the propagation than necessary. The idea of a temporal correlation function is to describe quantitatively how quickly a process changes in time. The power spectral density and temporal correlation function are related by

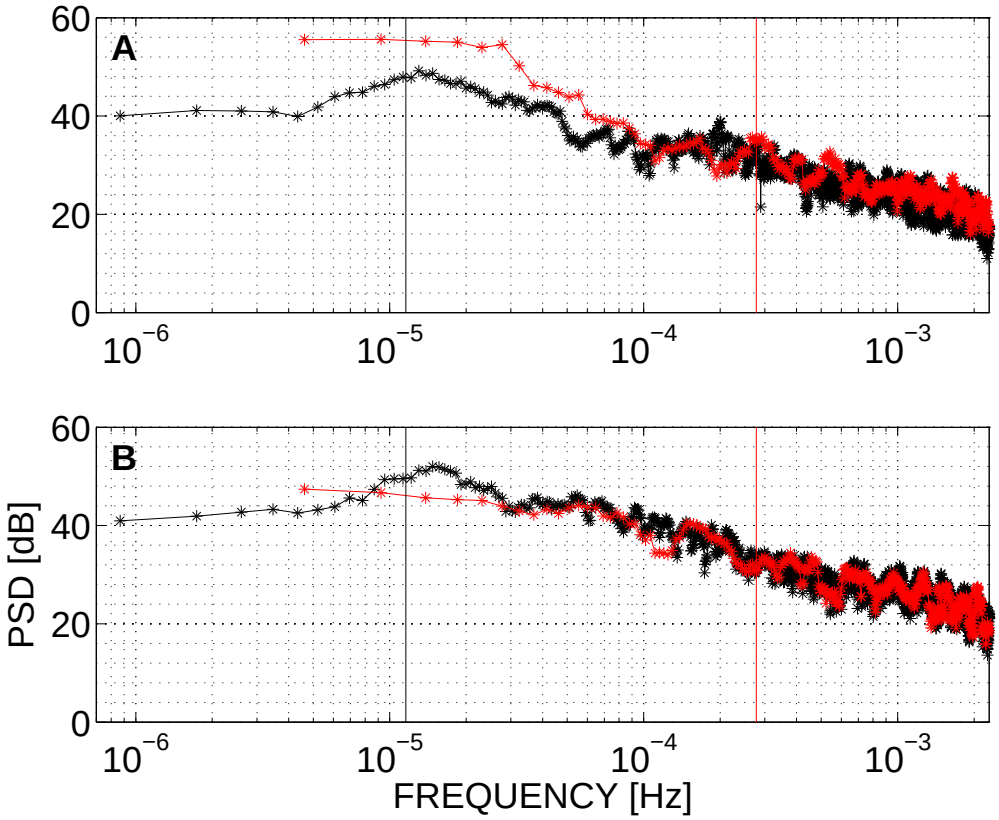

Figure 3.18: PSD predictions and estimates for paths ID-3 and ID+4 at 1550 m depth are shown in panels A and B, respectively. Black curves are the predicted PSD with transmission gaps imposed and filled with the interpolated trend. Red curves are the estimates from measured data, with the gaps also filled with the interpolated trend. Black and red vertical lines show frequencies of $1\,\mathrm{d}^{-1}$ and $1\,\mathrm{h}^{-1}$, respectively.

Fourier transform. These quantities constitute a good start in describing the time-dependence of acoustic intensity fluctuations.

The effect of having gaps in the intensity time-series seriously complicates the estimation of the PSD and temporal autocorrelation function by introducing various types of bias into the estimates. The simplest solution to the problem of gappy data, when one wishes to compute the spectrum, is to simply fill in the missing data with "0"'s. The study using the AR(1) model showed that for a nearly flat spectrum, the result of doing so with the transmission schedule used in PhilSea09 was to lower the spectral level by 3 dB to 4 dB: substituting zeroes effectively lowers the energy level. This was partially offset by the rise at higher frequencies, as shown in panel B of figure 3.11. The rise at high frequencies was probably due to aliasing of bogus high frequency content introduced by abrupt gap edges.

The spectrum of the lowess trend from the measured ID-3 data had an elevated level at low frequencies and fell very rapidly with increasing frequency. This is as expected, since the lowess trend is largely a low-frequency process. Introduction of gaps into the trend caused a decrease in the slope of that fall—alternatively, the gaps caused a rise in spectral level at high frequencies (again, abrupt gap edges add high-frequency energy). By comparing panels A, C, E, and G of figure 3.11, it is apparent that the PSD of the trend exceeded that of the AR(1) process for frequencies below 1×10^{-4} Hz. Comparing panels E and G, it may be seen that the spikes are effectively reduced by filling the data gaps with an interpolated trend instead of with "0"'s. This fact leads to the idea to alter the TD MCPE prediction by imposing gaps in order to be able to compare it with data. Though the spikes could be reduced nearly completely, the elevated level at high frequencies due to the gaps could not be corrected. The failure to remove this bias means that the comparison between the predicted and measured spectral slope may not be trusted. The situation at low frequencies (below

1×10^{-4} Hz), however, is probably not as dire; it was shown that replacement of data in the gaps with the interpolated trend caused the spectrum to be changed very little from its true value.

3.5 Conclusions

Data outliers due to equipment malfunction, signal ramp-up, elevated noise or weak SNR, and man-made noise sources such as passing ships and sonar were detected and removed. This clean-up effort helped to contribute a set of measured intensity time-series to the ocean acoustics community for further study. Time-series were obtained at 30 hydrophone depths for path ID-3, 25 depths for paths ID+4 and ID-4, and 28 depths for path ID+5. These data have an unprecedented temporal resolution of 7.2 s, allowing the study of very short timescales of fluctuation. The measurements encompass a time period of just over 60 h.

Simulated time-series of intensity resulting from broadband propagation through a model of the time-evolving internal-wave-perturbed ocean, at a time-step of 240 s for 320 h at a 1 m-depth spacing have also been contributed. This data-simulation pair will allow other predictions and estimates of other quantities to be compared: for example, the vertical correlation of intensity.

Predictions by TD MCPE of the one-sided PSD and the temporal correlation function at all hydrophone depths have been computed, and appear in appendix D. These predictions will be available for comparison to measurements when the problem of bias in spectral estimates is more satisfactorily solved.

The spikes in the PSD which appear at particular frequencies were a product of the transmission gaps, and were only present in the estimates for the path with fades. These spikes were mostly removed by replacing the missing data with an interpolated lowess trend. The results of the studies of bias using AR(1) and TD

MCPE simulations showed that it was possible to remove the bias for some portions of the spectra. The correlation function was affected in a less-understandable way—and therefore the estimate of this quantity from the measurements was not included here.

A method to remove the bias at high frequency due to transmission gaps was not found here, but comparison between predicted and measured spectra at low frequencies was made. The spectra were better predicted for path ID+4 than for ID-3 at the low frequencies where path ID-3 had an increased spectral level. The comparison between the predicted and measured PSD was good for the two paths at frequencies above 1×10^{-4} Hz. The local maximum in spectral level at a frequency of $1\,\mathrm{d}^{-1}$ that was predicted was not observed; this may be due to the small number of spectral points at the low frequencies, i.e. poor resolution for periods of approximately 1 d and longer in the measured data. The fades in path ID-3 likely caused the large disagreement between prediction and measurement seen at the low frequencies. To the extent that it can be assumed that replacement by the interpolated trend affected the prediction in exactly the same way as it does the measurements, the spectra were seen to compare well at intermediate and high frequencies.

Part II

DEEP FADES

The best-laid schemes
o' mice an' men
Gang aft agley,

Robert Burns
To A Mouse, On Turning Her Up
In Her Nest With The Plough
Kilmarnock Volume

Chapter 4

ON DEEP FADES

4.1 Introduction

In chapter 2 it was seen that the MCPE simulation confidence intervals encompassed the experimentally-measured values for the SI and the rms log-amplitude σ_ι for hydrophone depths from 625 m to 1125 m for path ID-3. Below this depth, the measured values increased beyond the prediction (see figure 2.11), and the similarity between empirical intensity distributions decreased. Deep fades with durations of 12 h to 18 h were easily recognizable at hydrophone depths at which the predictions of fluctuation measures under-predicted the observations. As path ID-3 has the shallowest UTP of all paths in PhilSea09, a difference in variability in the extreme upper ocean between the simulated oceans and in-situ measurements seems a good place to start looking for the cause of these deep fades.

Various features of the Philippine Sea propagation environment were not modeled by the MCPE simulations that were presented in chapters 2 and 3. The sound speed model in the simulations consisted of a range-independent smooth, average profile $c(z)$ plus perturbations $\delta c(x, z)$ due to vertical internal-wave displacements. As was mentioned in chapter 2, the Philippine Sea has greater oceanographic variability than those environments for which the GM model has been found to be sufficient for modeling acoustic fluctuations. This greater variability is manifest in slow (timescales of several days to weeks or months) mesoscale (spatial scales of order 100 km) range-dependence and in large local internal tides. The internal tides' most energetic components are at diurnal and semi-diurnal timescales, and have spatial scales which overlap the order 100 km mesoscales at the longest scales and are tens of km at the smaller scales.

The effect on the acoustic intensity of these two most obvious oceanographic features is not addressed by the MCPE simulations—at least not specifically or intentionally. The values of the parameters and the functional forms of mode and wavenumber

spectra in the GM model of the diffuse internal waves, being empirically-derived, have undoubtedly been influenced by other processes. For example, the presence of local internal tides may have contributed to the value of the standard GM strength. This is not a criticism of the model, but rather a recognition of the fact that nature doesn't consider the scientists' need to isolate a particular physical process in order to most accurately measure and characterize it.

Some model-environment mismatch in the extreme upper ocean is apparent in figure 4.1, in which 21 CTD-derived sound-speed profiles taken during PhilSea09 are plotted against a set of profiles taken from internal-wave-perturbed model oceans. This mismatch is not a complete surprise, given that the GM model was not intended for the extreme upper ocean; the boundary condition for the vertical internal-wave modes requires them to go to zero at the ocean's surface. Also, in the approach taken in chapter 2, the GM strength parameter was set by excluding the contribution due to the local internal tides at several frequencies, thus extra variability should be expected in the actual ocean as compared to the model oceans.

Figure 4.1 exemplifies the extent to which the MCPE model environments underrepresent the measured sound-speed variability. The MCPE model oceans were built upon a range-independent "background" sound-speed profile, and should not be expected to contain all of the variability. For example, some of the profile-to-profile differences between the measured casts represent range-dependence that would not change much over the duration of the acoustic transmissions. The necessary amount of range-dependence to be included in a model environment is likely geometry- and geographical location-dependent.

Section 4.2 will present a variety of in-situ measurements, including satellite measurements made completely independently of the experiment, but that are available to the general public. In addition, sound-speed profiles measured in 2010 by autonomous

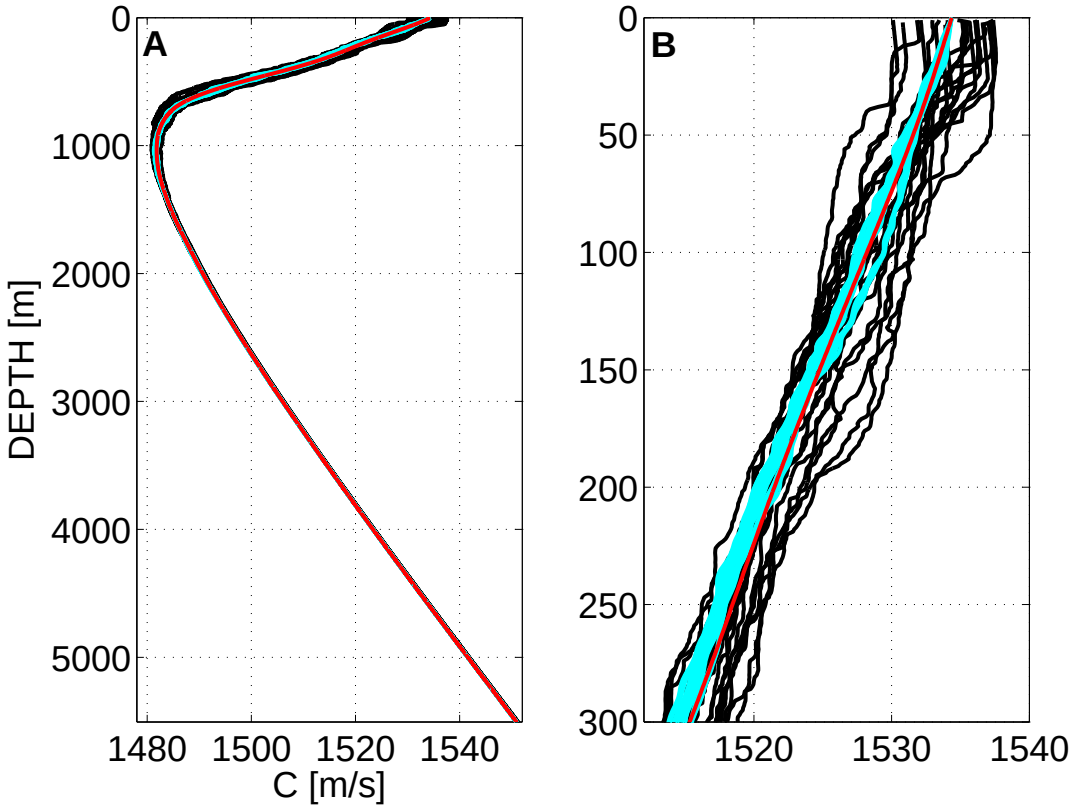

Figure 4.1: Shown here is a comparison of the 21 sound-speed profiles taken during PhilSea09 (black curves), with 21 profiles taken randomly from MCPE model oceans (cyan curves), and the range-independent average profile from the experiment (red curve). Panel A shows the full water-column depth and panel B is identical except that it shows only the upper 300 m.

underwater vehicles called "Seagliders" will be considered in section 4.4, as they provide many more measurements of the extreme upper ocean in the region—though at a different time of year. Section 4.3 will explore predictions of the variability in intensity that is to be expected due to the character of the measured sound-speed profiles shown in figure 4.1.

Section 4.4 focuses on a particular feature of the upper ocean: the surface mixed layer. The definition of the term "mixed layer" will be loosened slightly in consideration of its effect on acoustic propagation, as will be explained in that section. An attempt to characterize the mixed layer in the region, and predictions of intensity using a simple range-independent model will be presented.

In section 4.5, the local internal tides are examined. A simple internal-tide model is constructed using environmental measurements made at the DVLA, with the purpose of answering whether those measurements may be used to infer something about the internal tide at the location of path ID-3's UTP.

In this chapter, two hypotheses will be considered. One hypothesis involves interaction of the acoustic energy propagating along path ID-3 with a surface mixed layer. To explore the possibility of interaction with a surface mixed layer, the same range-independent profile used in the MCPE modeling was modified to include a mixed layer. Some of the results from acoustic mode propagation through the modified sound speed profile are consistent with this hypothesis. The other hypothesis involves a combination of the effects of mesoscale variability with sound-speed fluctuations caused by internal tides. Acoustic propagation modeling through some of the measured sound-speed profiles and the measurements of sound-speed fluctuations taken by instruments on the DVLA are consistent with this second hypothesis. Oceanographic measurements were too sparse to uniquely identify the primary process influencing the intensity fades—or as seems more likely—apportion the influence

to multiple confounding processes in a possible mixture.

4.2 Environmental measurements: 2009

4.2.1 AVISO

To begin our survey of the environmental data taken in the PhilSea09 and PhilSea10 experiments, measurements of sea-surface height (SSH) taken from the AVISO (Aviso and support from Cnes, 2012) database will be presented. These measurements give a synoptic view of the region of the experiment, and best represent the mesoscale variability that was present. Figure 4.2 shows six measurements, spanning longitudes from about 119.5° to 130.5° E and latitudes from 15.5° to 26.5° N, and spanning times from YD 98 to YD 133 of 2009. This period of time is also about the same as that over which the DVLA was deployed; instruments attached to the DVLA took measurements of temperature, salinity (from conductivity), pressure, and current velocity. The DVLA environmental measurements will be compared with the SSH measurements in this section, for the purpose of putting the experiment into its physical context, and providing some verification that interpretations of the various environmental data are consistent.

There are a few mesoscale-sized features that seem to persist throughout the period of time shown in figure 4.2. Two features in particular should be pointed out: the first is visible in the panel marked YD 98 at about 21.5° N latitude at the right edge of the panel as a depression (blue) in SSH, and the second feature is visible at about 21° N, 127° E as an elevated region (red). Elevated SSH is indicative of parcels that are composed of warmer water and depressed SSH indicates colder water. Plotted over the SSH are the current vectors, also available from AVISO, which are calculated assuming geostrophic balance.

Both of the features appear to move westward over the duration of the experiment.

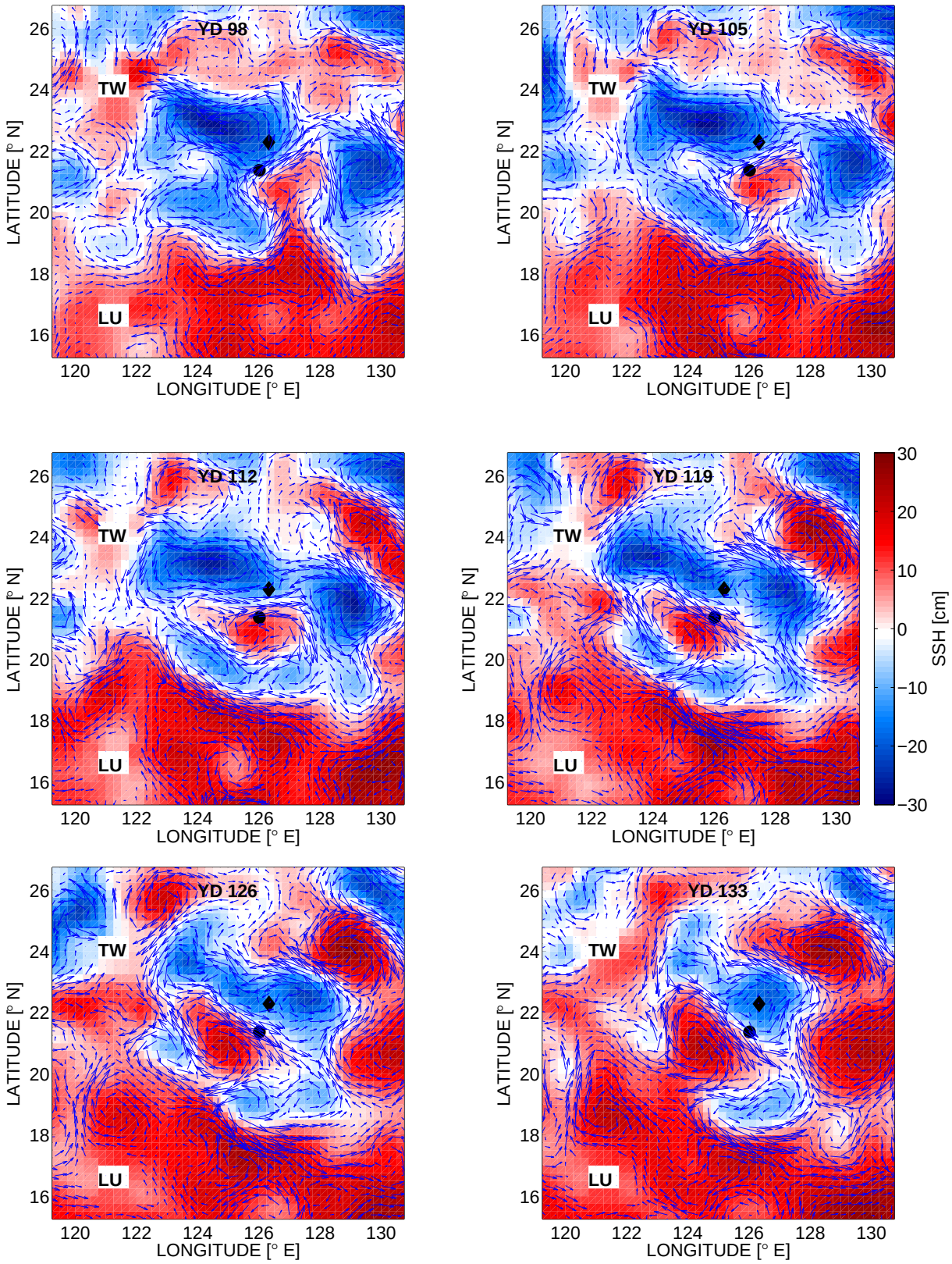
YD 98
YD 105
YD 112
YD 119
YD 126
YD 133
TW
LU
LATITUDE [° N]
LONGITUDE [° E]
SSH [cm]
26
24
22
20
18
16
120
122
124
126
128
130
30
20
10
0
−10
−20
−30

The northern edge of the elevated feature moves across the position of the DVLA around YD 112. If the assumed geostrophic balance provides an accurate picture of the currents, it would be expected that current velocity at the DVLA should have a positive northward component as the elevated feature approaches the DVLA, followed by a negligible north-south component, and then be directed southward as the feature recedes from it. A positive eastward component would be expected throughout the duration of the experiment.

4.2.2 Currents at the DVLA

An upward-looking acoustic Doppler current profiler (ADCP) was located on the DVLA, providing measurements over the depth range 350 m to 100 m. The current velocities measured by the ADCP are shown in figure 4.3. The vertical striping is caused by the diurnal internal tides' modulation. As is consistent with the geostrophic currents derived from SSH, the eastward component is positive during the time of the experiment, and the north-south component goes from northward to southward over the same period of time.

Figure 4.2 *(facing page)*: Shown is the sea surface height (SSH) from the AVISO database, with u and v superimposed—also from AVISO. The position of the DVLA is indicated by the circle and the diamond indicates the position SS107, from which acoustic transmissions were conducted. The islands of Taiwan and Luzon are labeled "TW" and "LU". The color scale is from -30 (blue) to +30 (red) cm. The yearday appears in the top center of each plot; shown here are measurements taken during the duration of the DVLA's deployment. Positive (negative) values of SSH are associated with features composed of warmer (colder) water temperatures. Westward propagation of a warm-water feature that is located at 21° N, 127° E on yearday 98 is apparent during the span of the measurements. The warm feature is seen to pass over the position of the DVLA. A cold-water feature that is located at 21.5° N, 129.5° E on yearday 98 propagates westward during the span of the measurements—coming into contact with the DVLA near the end of its deployment.

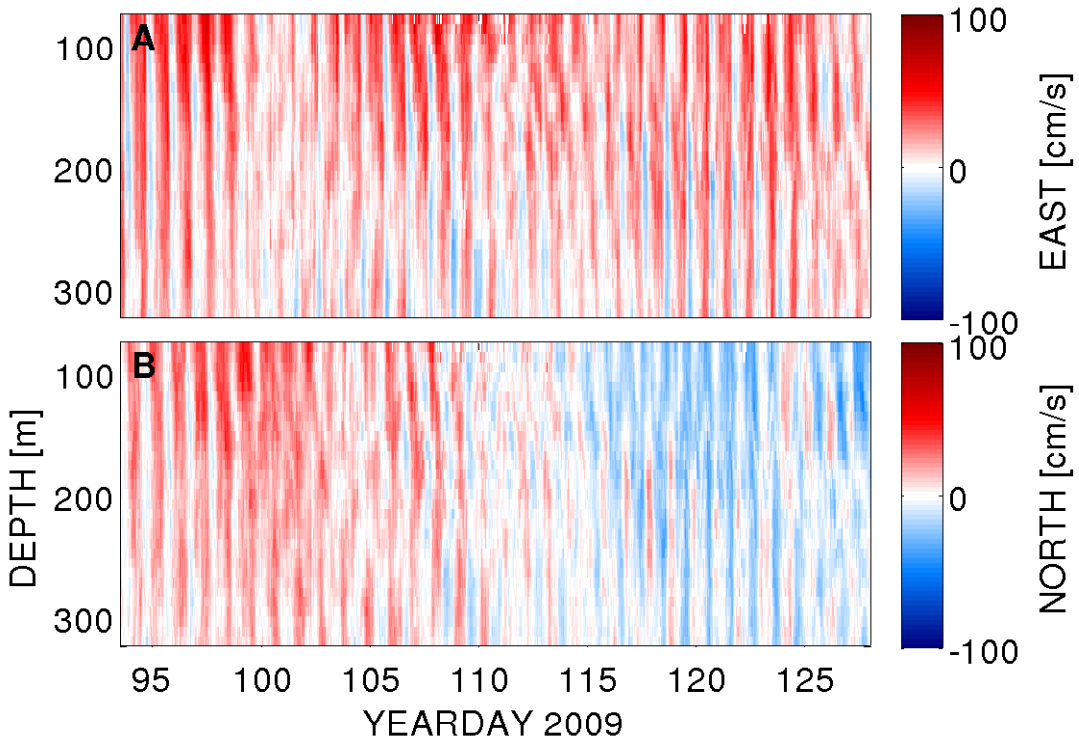

Figure 4.3: Shown are the currents measured at the DVLA by the upward-looking ADCP. Currents in the East-West (+/-) direction are shown in panel A and in the North-South (+/-) direction in panel B.

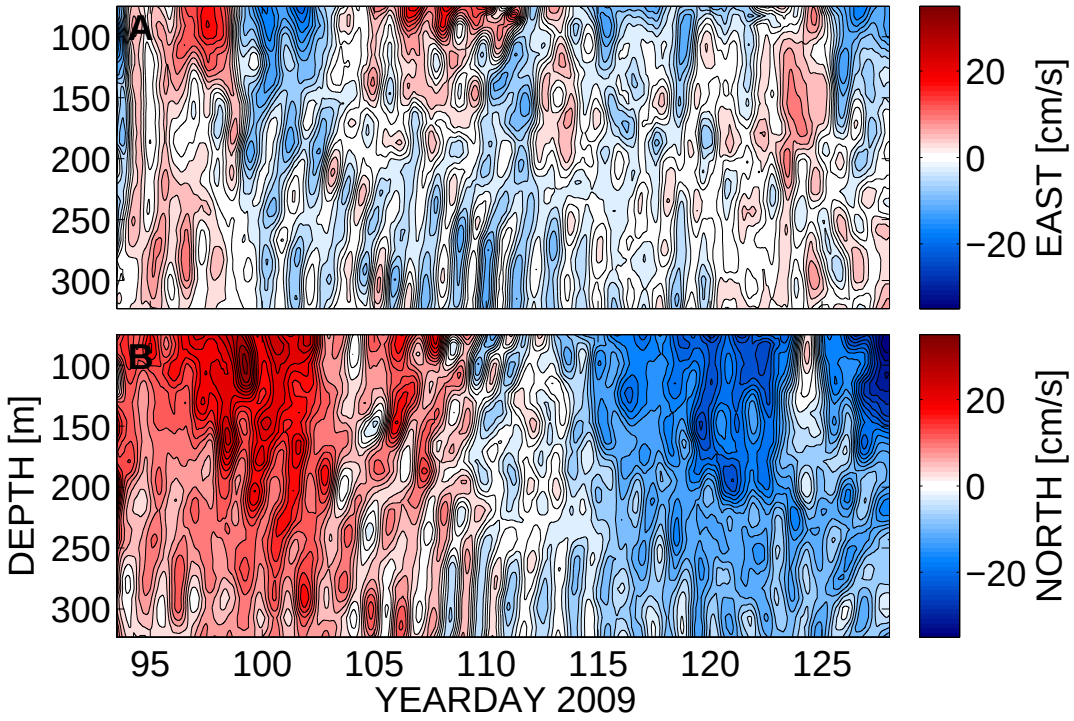

Figure 4.4: Shown is the low-pass (periods longer than 24 h) horizontal current velocity at the DVLA. Panel A is the East-West +/- component and panel B is the North-South +/- component.

The same currents, de-meaned and then low-pass filtered with a 3rd-order Chebyshev filter for frequencies below 1 /24 h, are shown in figure 4.4. In this case, the banded appearance is due to currents with frequencies near the inertial frequency at 1 /32 h—i.e. . The inclination of the bands that is apparent before YD 113 would seem to indicate upward-propagating waves.

4.2.3 Seawater properties at the DVLA

De-meaned and low-pass (for frequencies below 1 /24 h) filtered temperature and salinity at the DVLA are shown in figure 4.5. It is apparent in panel A of the figure

that around YD 105, warmer water passed by the DVLA, resulting in deepening of isotherms and, after YD 115, the warmest water at depths shallower than 120 m has gone away. The deepened isotherms remain, leaving a diminished vertical gradient in temperature.

The salinity record shown in panel B of figure 4.5 exhibits an increase in salinity beginning at YD 105. After YD 115, the salinity decreases below the value observed before YD 105, and the gradient in the depths from 150 m to 90 m is diminished.

De-meaned and low-pass filtered density and sound speed are shown in figure 4.6. The observed decrease in temperature after YD 105, accompanied by an increase in salinity apparently resulted in an overall decrease in density: the isopycnals deepened and, then after YD 115 spread further apart. The same changes in temperature and salinity resulted in an increased sound speed after YD 105. When the warm, salty water that was present from YD 105 to YD 115 goes away, the sound speed decreases and the vertical gradient becomes smaller than it was before YD 105 and is especially weak above about 150 m depth. This is all consistent with the proportionality (inverse) between temperature and sound speed (density), and the proportionality between salinity and both sound speed and density.

Figure 4.7 shows a comparison between sound speed and the northward component of current velocity, where both variables have been de-meaned and band-pass filtered for frequencies from 1 /24 h to 1 /12 h. The first period of time shown in panels A and B in the figure is from YD 105 to YD 115. Between YD 105 and YD 110 the northward current corresponds directly in time with an increase in sound speed, over the whole depth span shown. From YD 110 to YD 115 the currents in the north-south direction weakened and then appear to be less coherent in the vertical direction. The sound speed variability during that same period took on a different character, with maxima from 100 m to 200 m occurring at different times than those occurring at

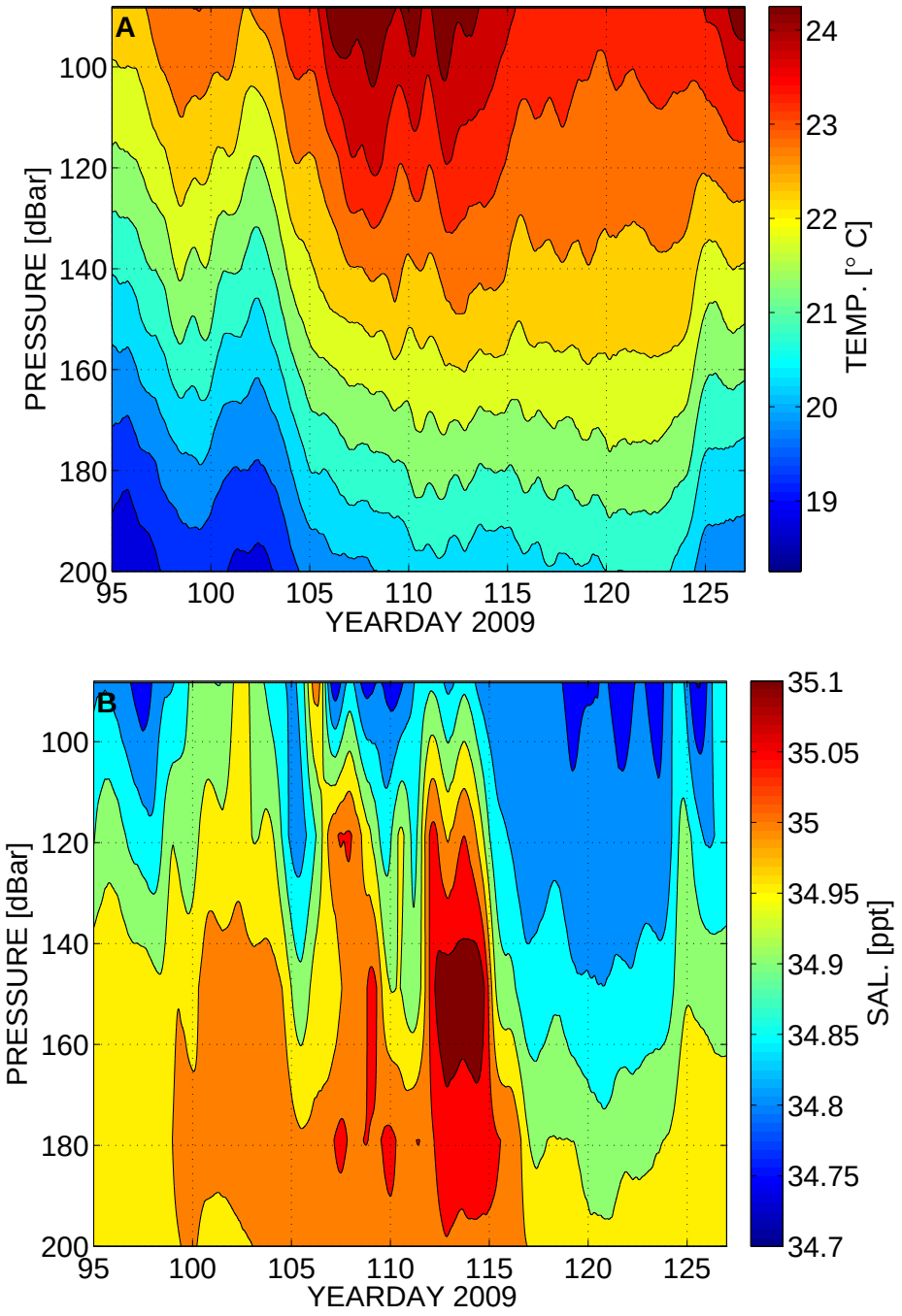

Figure 4.5: Shown here are the temperature, plot A and salinity (via conductivity), plot B measurements taken by the microCAT sensors on the DVLA. Only the upper 200 dbar are shown. Data have been low-pass filtered for periods longer than 24 h for clarity of presentation. Notice the warmer temperatures evident from yearday 105 to 115. This is in agreement with what would be expected from the SSH measurements shown in figure 4.2. During the same period there is an elevated level of salinity compared to before and after the same time period.

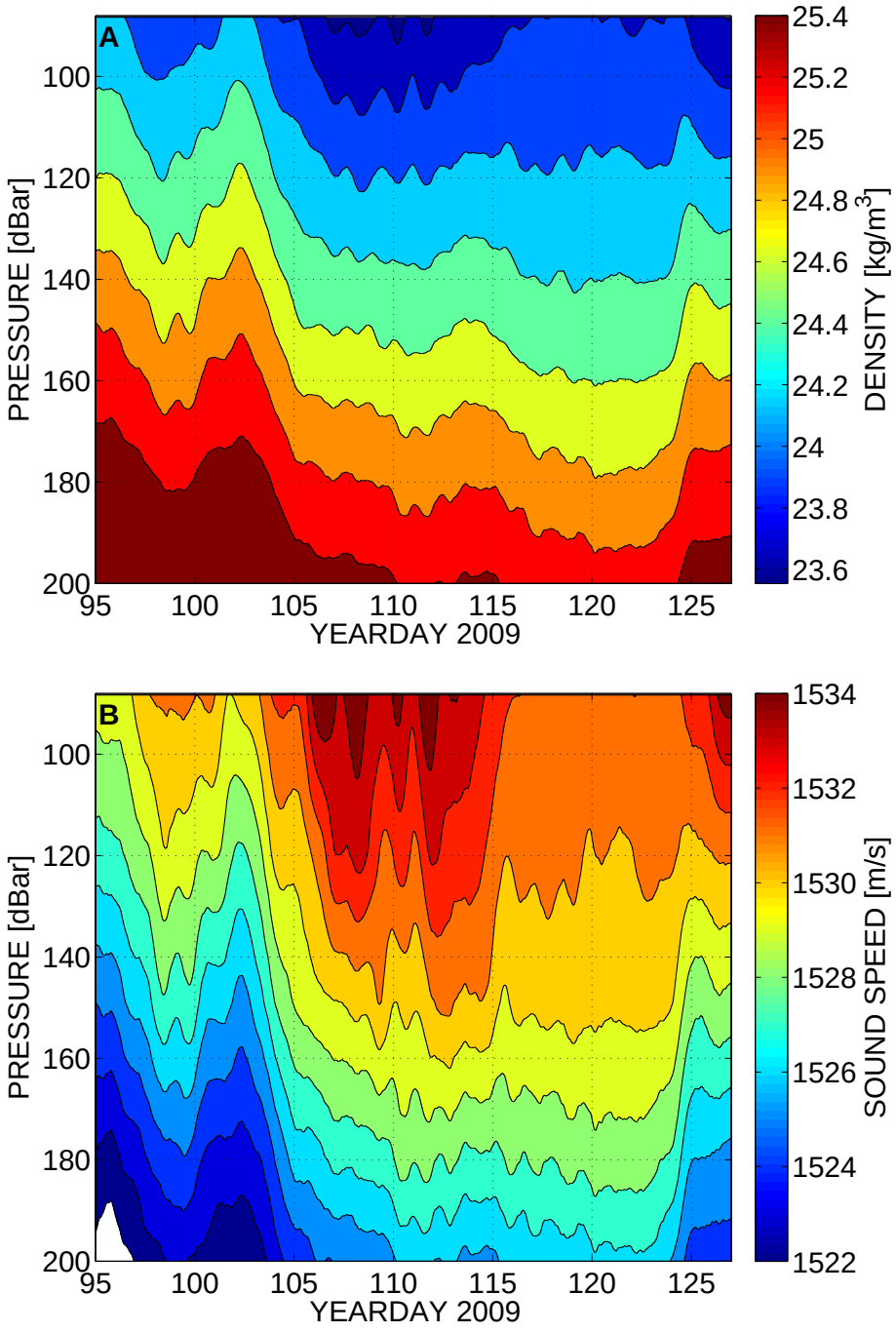

Figure 4.6: Shown are the density, plot A and sound speed, plot B from measurements taken by the microCAT sensors on the DVLA. Only the upper 200 dbar are shown. Data have been low-pass filtered for periods longer than 24 h for clarity of presentation. There is a decrease in density and an increase in sound speed from YD 105 to YD 115, followed by a decrease in the vertical gradient of both quantities after YD 115.

depths from 200 m to 300 m.

Panels C and D of figure 4.7 show the same measurements from YD 115 to YD 125. The dual-maxima structure in the sound speed before YD 115 is visible in the north-south currents after YD 115, with a minimum in current variability between the two maxima appearing to descend in depth from YD 115 to YD 125. The sound speed variability over the time period shown in panel D is characterized by stronger variability below 150 m depth—and very weak variability above that depth.

4.3 Intensity variability by profile

The vertical CTD casts provide information about the vertical structure of sound speed down to scales much smaller than an acoustic wavelength at 284 Hz. The measurement is almost a snapshot: the instrument takes about two hours to descend to the full ocean depth around 5 km or 6 km, as was the case in the Philippine Sea. No information is provided in the horizontal, however, and none of the other available measurements provide detailed information, except in the vertical. The horizontal extent of an UTP is of a similar scale to the horizontal correlation length of sound speed; a simple model that could be constructed from the CTD cast information is a measured sound-speed profile as a range-independent model, $c(z)$.

An idea about how much variability in intensity might be expected from differences in these measured profiles could be gained from modeling acoustic propagation through each of the set of such range-independent models. The set of 21 CTD casts represent variability in the vertical sound speed profile over a span of time equal to the duration of the experiment, and were taken over a transect with a length roughly twice that of the acoustic propagation paths, and approximately co-linear with those paths. An acoustic normal-mode propagation model is sufficient for a range-independent sound-speed environment. Acoustic normal modes were computed over the same

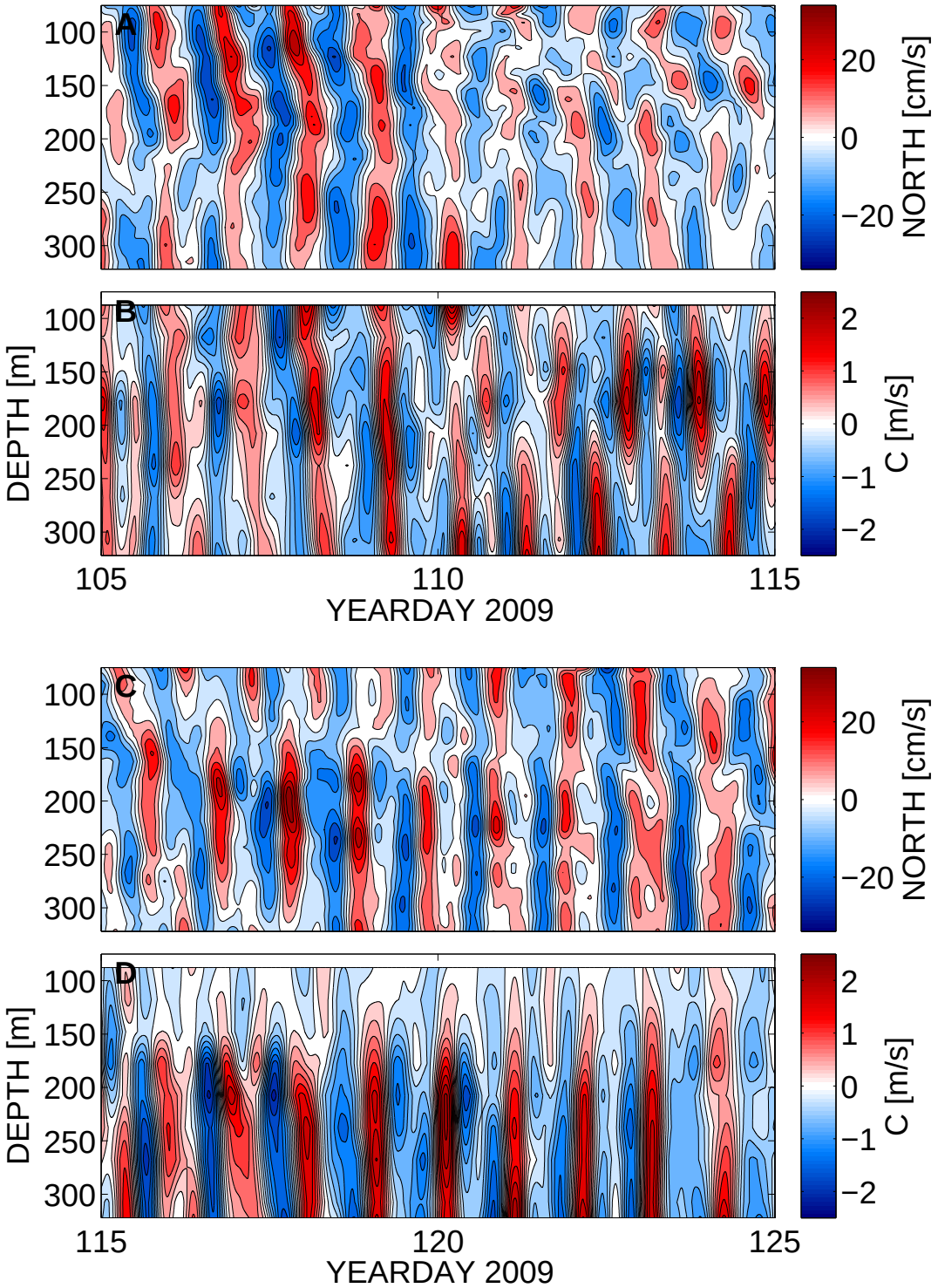

Figure 4.7: Comparison of northward current speed and sound speed fluctuations at the DVLA position. Shown in panels A and C are the currents (band-pass filtered for periods from 12 h to 24 h) in the North-South direction, with 5 cm s^{-1} contours for two different 10 d spans of time. Shown in panels B and D is the sound speed filtered with the same pass-band, with 0.25 m s^{-1} contours.

band of frequencies used in the MCPE model, using the KRAKEN (Porter and Reiss, 1984, 1985) computer code, and propagated through an environment consisting of each measured profile. Path ID-3 was windowed out from the resulting timefronts, and the intensity was calculated as the absolute square of the 284 Hz Fourier component for path ID-3 at each meter of depth from 625 m to 1625 m.

Selected results are shown in figures 4.8, 4.9, and 4.10—grouped according to the cruise on which the individual profiles were taken. Upper-turning-point depths for the various paths were given in table 2.1 in chapter 2. The reader will recall from this table that the shallowest-turning eigenrays (in the smooth, average profile) of path ID-3 arrived at the deeper receivers of the shallow sub-array, while those eigenrays whose upper turn was slightly deeper arrived at the shallower receivers. For reference, horizontal blue lines are plotted on the selected profiles that are shown in figures 4.8, 4.9, and 4.10 which follow—though the turning depths in any individual profile would differ somewhat from those corresponding to the smooth profile. The local time at which each cast was taken appears in each plot as well.

In figure 4.8, the sound speed is progressively slower above a depth of 150 meter with each cast for casts 2, 3 and 4. Cast 5 does not follow this pattern, however, and the sound speed is faster than the smooth, average profile for those same depths. The predicted intensity is seen to decrease along with the slower sound speed, and then to increase slightly as the sound speed increases with cast 5 at the shallowest receiver depths shown.

The profiles shown in figure 4.9 were taken on different days, but were taken closest in time to the time of the acoustic transmissions; profiles 9 and 10 were taken the immediately before and after the transmissions. Casts 6 and 9 did not exhibit sound speed that was markedly different from the smooth, average profile—and the predicted intensity for those casts is not greatly different from that of the smooth

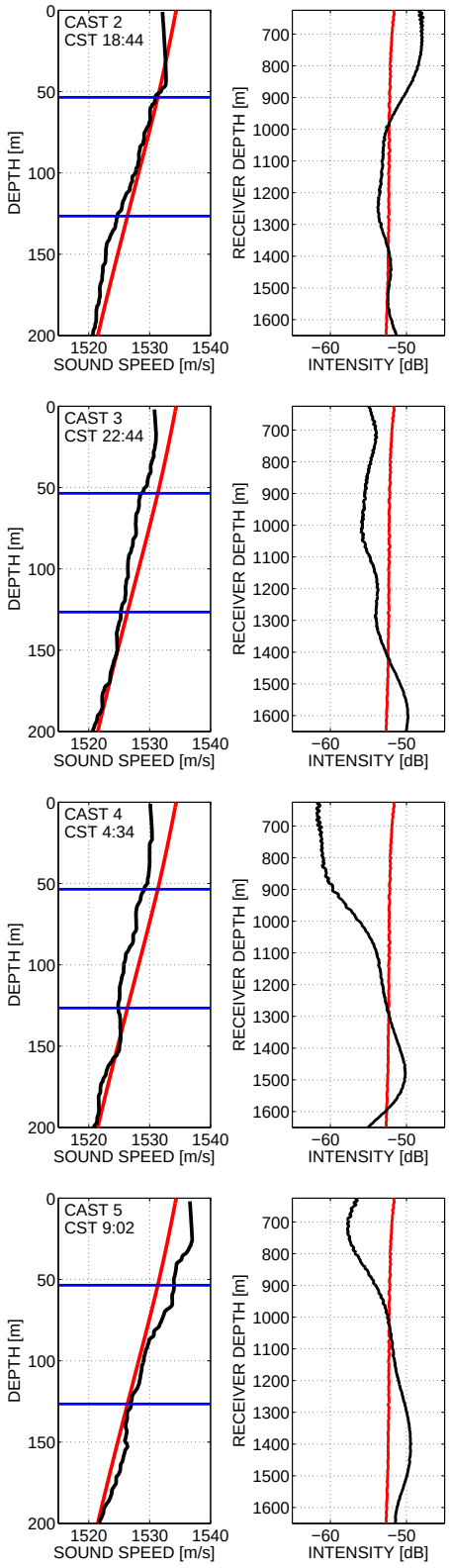

Figure 4.8: Comparison of predicted intensities for sound speed profiles measured in individual CTD casts with the predicted intensity for the smooth, average background profile. Shown is a set of four profiles taken during the DVLA deployment cruise (MV0905) during PhilSea09. The black curve shows the upper 200 m of the measured profile and the red curve shows the average range-independent profile used previously in MCPE modeling. Each profile is paired with the predicted intensity for path ID-3 at the depths of the upper sub-array, shown immediately to the right in each case. The local time, "China Standard Time" abbreviated "CST" is indicated in each panel. In the corresponding intensity panel, the intensity shown in black is that predicted for the particular profile; the red curve is the intensity predicted for the range-independent average profile. Blue lines show the upper turning depths of ID-3 in the range-independent average profile. The shallower of the two blue lines is the upper turning depth of the eigenray to the 1625 m hydrophone.

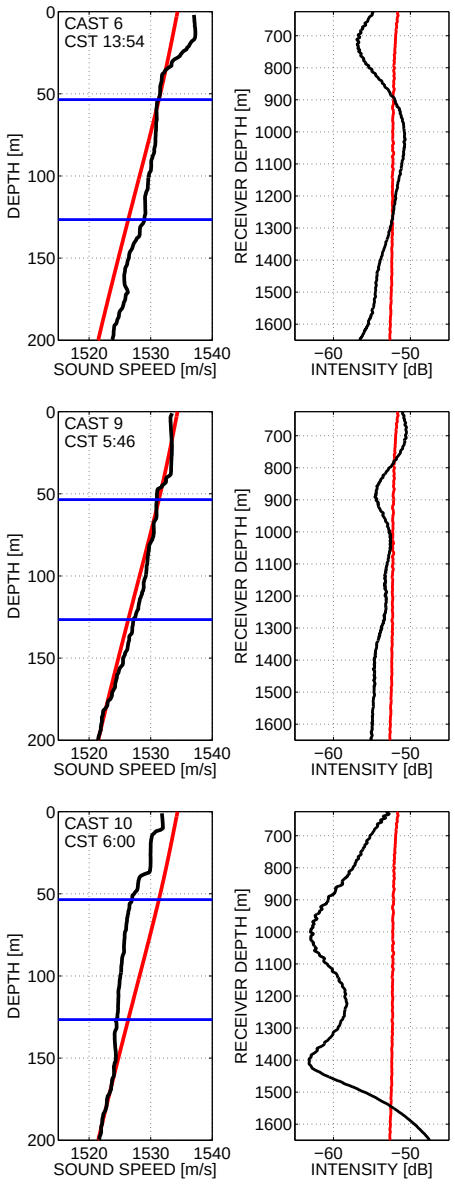

Figure 4.9: Comparison of predicted intensities for sound speed profiles measured in individual CTD casts with the predicted intensity for the smooth, average background profile. Same as figure 4.8 with profiles taken as part of the cruise during which acoustic transmissions were made (MV0906). The third cast was taken immediately following the acoustic transmissions, to the north of SS107.

profile. Profile 10 had slower sound speed at the turning depths for ID-3 and the intensity was diminished by about 10 dB. Profile 10 was taken a few hours after acoustic transmissions ended.

The final group of profiles is shown in figure 4.10. The casts were taken as the ship progressed southward along the propagation track. None of the profiles caused a predicted intensity decrease as large as that of profiles 4 or 10.

It is difficult to identify exactly what it is about a given profile that causes a predicted intensity decrease. Some possible mechanisms include ducting of acoustic energy and focusing/de-focusing. Ducting refers to the idea that at places in an acoustic path where energy is turning, the path might be extended or trapped in the horizontal direction by weak vertical gradients in sound speed. Focusing/de-focusing refers to the idea that decreases (increases) in intensity are due to spreading (convergence) of paths; this could be caused by features of the sound speed profile of tens of m in spatial extent (for this acoustic frequency). The specific cause of any particular vertical dependence of intensity is likely quite difficult to identify in a given profile—though in the cases of the two profiles with sound speed about $4\,\mathrm{m\,s^{-1}}$ slower than the smooth, average profile, the predicted intensity was up to 10 dB less than for the smooth profile.

Figure 4.10 *(facing page)*: Comparison of predicted intensities for sound speed profiles measured in individual CTD casts with the predicted intensity for the smooth, average background profile. Same as figures 4.8 and 4.9, profiles taken during the DVLA recovery cruise (MV0907).

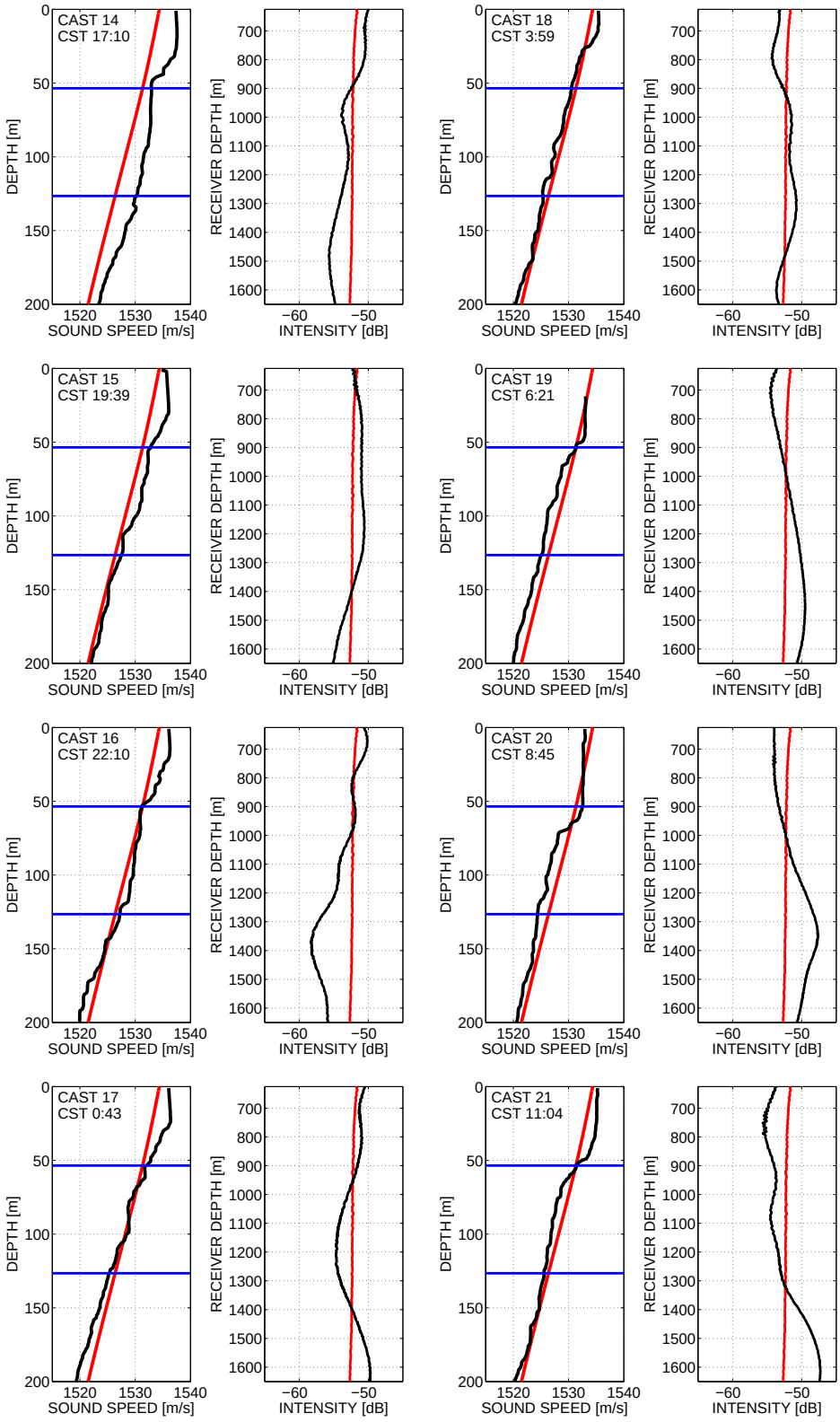
CAST 14
CST 17:10
CAST 18
CST 3:59
CAST 15
CST 19:39
CAST 19
CST 6:21
CAST 16
CST 22:10
CAST 20
CST 8:45
CAST 17
CST 0:43
CAST 21
CST 11:04
DEPTH [m]
SOUND SPEED [m/s]
RECEIVER DEPTH [m]
INTENSITY [dB]
0
50
100
150
200
1520
1530
1540
700
800
900
1000
1100
1200
1300
1400
1500
1600
−60
−50

4.4 Mixed layer

4.4.1 Introduction

The ocean's near-surface mixed layer depth exhibits variability on several timescales, most significantly for this discussion, seasonal and approximately daily. The largest variability happens on the seasonal timescale; the mixed layer goes from its deepest observed depths to not being present at all during particular times of the year.

During daylight hours, the upper ocean is heated by fluxes of sensible and latent heat, as well as long-wave radiation into the surface and volume heating through absorption of short-wave solar radiation. These inputs of heat are balanced by heat leaving the upper ocean through long-wave radiation out of the surface. When these fluxes amount to a positive net heat input into the upper ocean, the heating can result in partial stratification (and therefore destruction) of the mixed layer, including a near-surface mixed layer if the wind speed is large enough. In the absence of significant wind, this daily-formed stratification may reach the surface.

The physical process immediately responsible for deepening of the mixed layer is convection. At night, the short-wave solar radiation ceases and the overlying air cools, causing a net negative flux of heat into the ocean's surface. Water parcels near the ocean surface cool until their density increases beyond that necessary for a stable stratification, and then these parcels sink. There may be some convective penetration in which the sinking parcels overshoot the bottom of the mixed layer, causing some turbulent entrainment of the warmer underlying water of the thermocline into the mixed layer.

The historical definition of the mixed layer depth was the depth over which the temperature was seen to vary little, compared to the large gradient seen in the main thermocline Soloviev and Lukas (2006). A more comprehensive definition would use

density as the variable of interest; density depends not only upon the temperature, but also on the salinity of the water. This is complicated by the possibility of a profile in which the temperature varies little, but a jump in the salinity occurs. The salinity and temperature may vary such that an increase in both variables is seen in a particular parcel of water, giving no change in density. This water is dynamically stable, but may have a different sound speed than that of the surrounding water. For the purposes of studying the mixed layer's effect on acoustic propagation, the more appropriate variable for a mixed layer definition is the sound speed.

In a mixed layer composed of water with uniform temperature and salinity, the sound speed gradient is slightly positive with increasing depth, with the increase caused by the dependence on pressure. In the ray approximation, this feature causes rays to be upward-bending in the mixed layer. A ray which would turn at some depth near the surface will in the presence of a mixed layer instead bend toward and reflect from the surface—causing a horizontal perturbation to its path. This could be described as a temporary ducting of the sound, since the sound does not become trapped in the layer.

In the CTD (conductivity, temperature, depth) and XBT (expendable bathythermograph) casts made during 2009, the deepest mixed layer observed was 80 m depth. In the Seaglider-based measurements that will be presented in section 4.4.2, mixed layer depths of up to 160 m were observed, around YD 390 of 2010 (YD $390-365=25$ of 2011). The acoustic transmissions discussed in this paper were made at the end of the month of April 2009.

4.4.2 Mixed-layer depth measurements: 2010-2011

Seagliders are re-usable autonomous underwater vehicles that were developed by the Applied Physics Laboratory and the Department of Oceanography at the University

of Washington. Thrust is provided by controlling the buoyancy difference between the Seaglider and the surrounding water; the pitch and roll are controlled by shifting the internal position of the battery pack. Seagliders are capable of extended missions with a duration of many months. Data recorded by Seagliders may be telemetered via satellite each time the glider surfaces (Eriksen et al., 2001).

Four Seagliders were deployed in the Philippine Sea during 2010-2011 (Van Uffelen et al., 2013). Seagliders are usually equipped with pressure, conductivity, and temperature sensors, which take data continuously throughout their periods of deployment—though in this experiment they were also fitted with hydrophones to record acoustic transmissions for tomographic purposes. The acoustic data recorded by these Seagliders is not used in this thesis. One Seaglider, labeled SG513, completed 577 dives in the time period between 12 November and 27 February; data taken during these dives will be presented here.

The sound-speed profiles taken by SG513 were used to find the depth of the mixed layer during each dive. Depths were chosen visually, by identifying the mixed layer depth as the depth above which the majority of the water had a gradient in sound speed $\mathrm{d}c/\mathrm{d}z \geq 0$; i.e. an upward-bending (or no bending) profile. The motivation for identifying this depth was the idea that ducting might play a role in causing the intensity to decrease; in addition, the modeling presented in the next section, 4.4.3, suggests that an increase in mixed-layer depth could cause the intensity to fade at the receiver depths used in PhilSea09. A histogram of these depths appears in figure 4.11. Depths as large as 160 m are observed in the profiles.

A lowess trend was estimated from the time-series of mixed-layer depth created from the SG513 dives, and is shown in figure 4.12. The trend has variability on timescales of 10 d, including possibly a seasonal change, with the mixed layer deepening over the course of the period of time over which the dives were made by up to

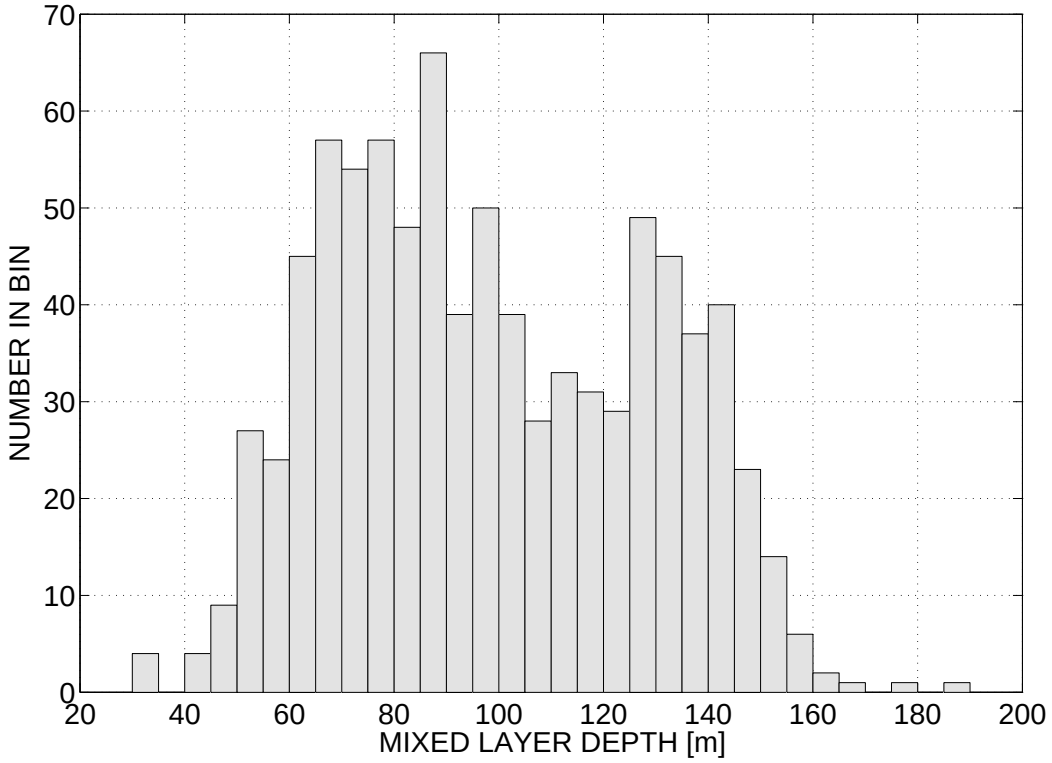

Figure 4.11: Histogram of hand-picked mixed-layer depths from the sound-speed profiles measured by SG513.

around 100 m.

Figure 4.13 shows a histogram of the mixed-layer depth after the trend has been subtracted from the time-series; this histogram gives an idea about how much the depth of the mixed layer changes on shorter timescales around a day. Apparently, changes by up to 60 m are possible—but almost all of the short-time variability is less than 20 m.

4.4.3 ML effects: normal modes

Sound-speed profiles were created with mixed layer depths from 2 m to 120 m. The mixed layers were given a vertical gradient in sound speed (just the gradient due to the pressure effect) which matched that observed in CTD casts; this gradient was estimated from pure mixed layers, i.e. well-mixed surface mixed layers—as opposed to a mixed layer which only satisfies the weaker condition $\mathrm{d}c/\mathrm{d}z \geq 0$. Modes that had been computed for each profile using the KRAKEN model for each acoustic frequency were propagated through each range-independent model environment to 106.6 km range. The arrival for path ID-3 was windowed, then Fourier-transformed and the absolute square of the 284 Hz component was calculated as the single-frequency intensity.

The top panel in figure 4.14 shows the modeled effect of a mixed layer on the acoustic intensity for receiver depths spanned by the upper sub-array. The modeling predicts a change of less than 3 dB for mixed-layer depths less than 55 m. Three regions of very large decreases in intensity appear in the prediction; these are the round white spots. The color is white because the decrease in intensity is greater than the deepest contour of the color scale shown. A decrease of about 9 dB is predicted around the three deepest hydrophone depths of 1475 m, 1550 m and 1625 m for mixed-layer depths around 90 m. The intensity decrease is greater for deeper hydrophone with any given mixed-layer depth. The intensity is predicted to begin to increase for

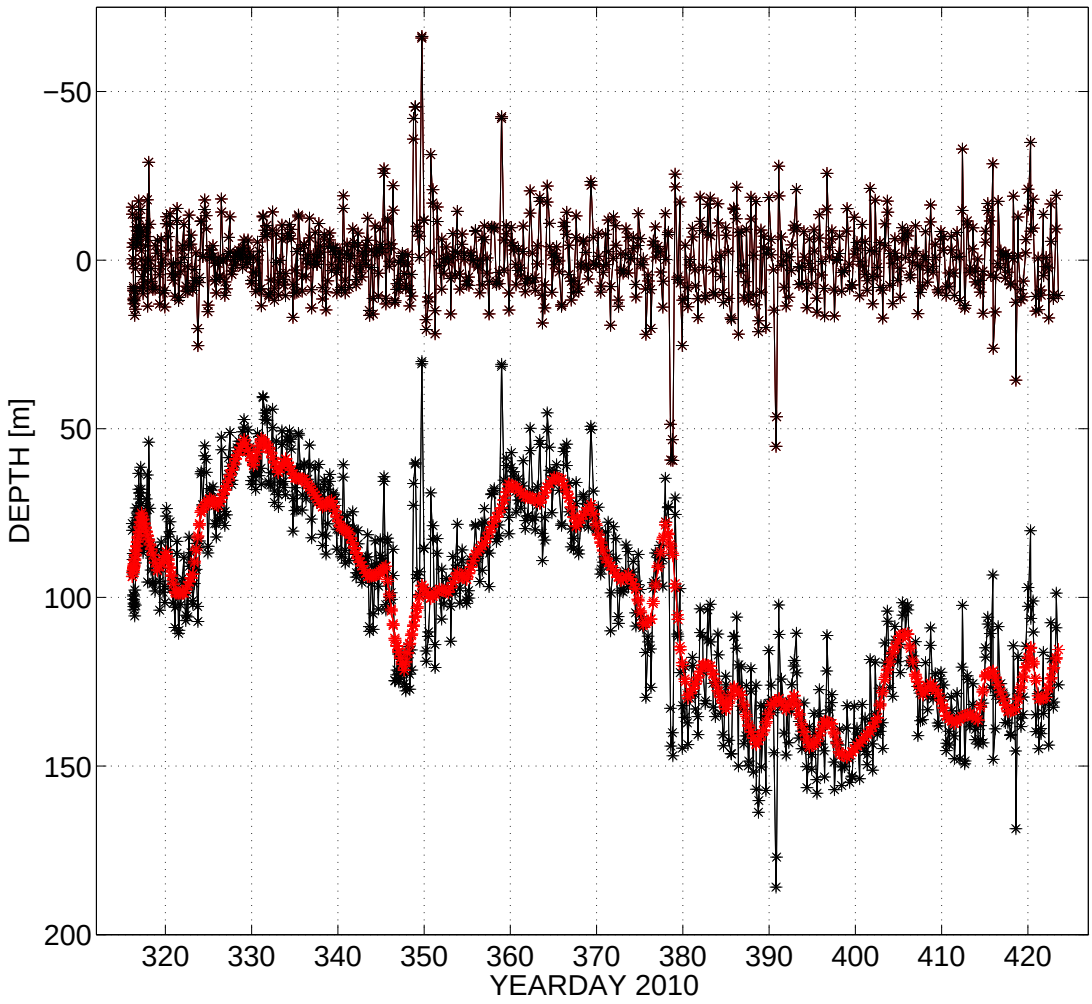

Figure 4.12: Time-series of mixed-layer depth from SG513 dives, along with a lowess trend in red. The curve centered at a depth of 0 m is the same time-series with the trend removed.

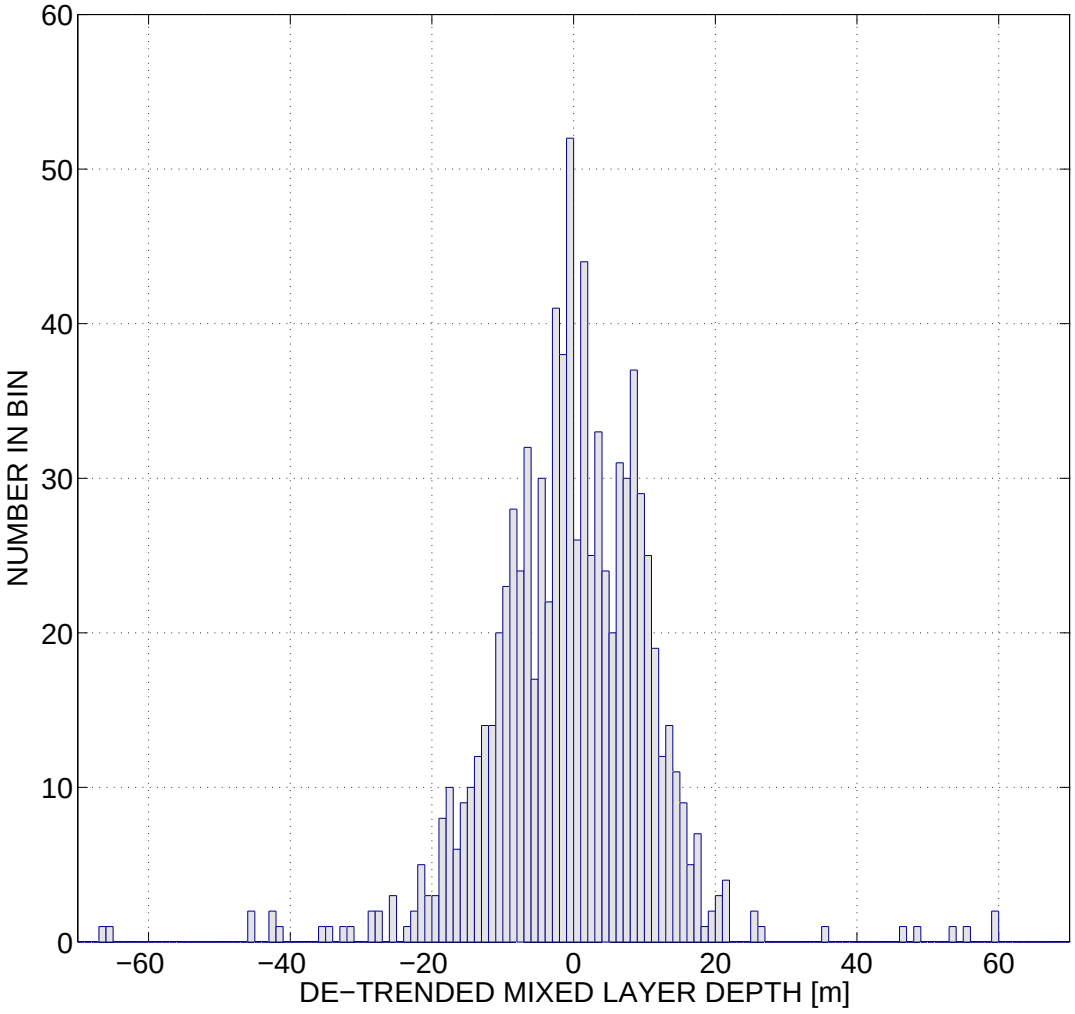

Figure 4.13: Shown is the histogram of deviations in mixed-layer depth from the trend shown in figure 4.12.

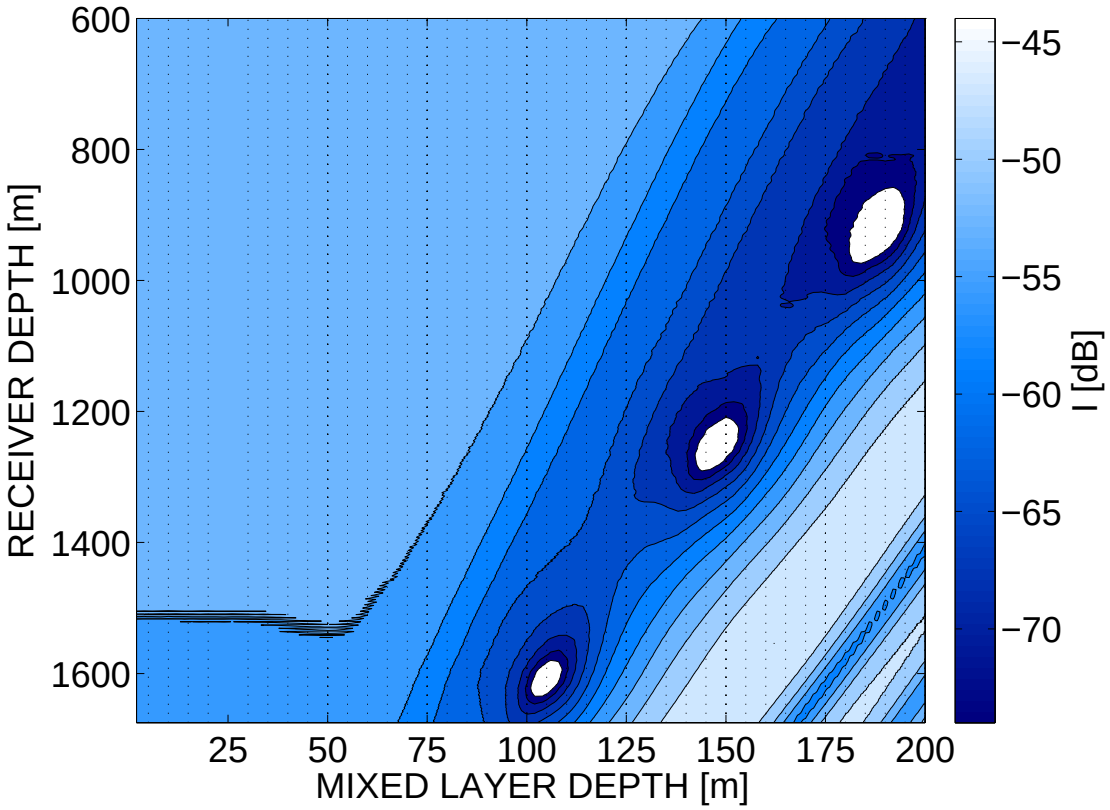

Figure 4.14: Shown is the predicted intensity of the 284 Hz Fourier component for path ID-3 for receiver depths from 600 m to 1650 m vs. mixed layer depth. 3 dB contours of intensity are plotted.

mixed-layer depths greater than about 105 m for receiver depths around 1600 m.

4.5 Internal Tides

4.5.1 Introduction

Internal tides (a baroclinic phenomenon) are generated when barotropic tides cause fluid flow over ocean bathymetry. Upon flowing over the bathymetry, isopycnals are disturbed and internal waves radiate from the location: this is conversion of barotropic to baroclinic energy (Zhao et al., 2012). Because the forcing is tidal, internal tides are dominated by waves near the constituent barotropic tidal frequencies. The amount of energy radiated at particular frequencies from a given location should depend on the geometry in terms of the tidal flow direction relative to the bathymetry, the depth of the bathymetry, and to the relative strength of the tidal components there. For example, in the Philippine Sea the diurnal internal tide radiates from the Luzon Strait, and the semidiurnal tide from both the Luzon Strait and from the arc of the Kyukyu Islands. An additional nearby source of internal tides is the Mariana Island Arc; flow across the bathymetry between islands combines with the shape of the arc to produce a beam of waves directed eastward, and slightly to the south of the PhilSea09 experimental region.

A model of plane internal-waves at tidal frequencies is described in this section. The purpose of constructing this model is to get an idea of how well sound-speed perturbations due to internal tides might correlate between the DVLA and ID-3 UTP positions. We obtained records of the sound speed at the DVLA, but would like to know how well these measurements might predict the changes in sound speed at the ID-3 UTP, located 106.6 km to the north-northeast. The sound speed record from the pumped microCAT sensors on the DVLA exhibits, after being band-pass filtered for frequencies including the diurnal and semidiurnal frequencies, sound-speed

perturbations of approximately $\pm 4\,\mathrm{m\,s^{-1}}$. Recall that this is the same amount that CTD profile numbers 4 and 10 were slower than the average profile; these profiles were associated with a decreased predicted intensity for path ID-3 using normal mode propagation modeling in section 4.3.

4.5.2 Model

The plane-internal-wave model consisted of the sum of the first ten modes at the diurnal and semidiurnal frequencies, with each mode given an amplitude and phase, $a_{kh,j}$ and $\theta_{kh,j}$, respectively. The vertical modes $\phi(z)_{kh,j}$ come from solution of the same equation that was solved for the internal-wave model used in MCPE calculations presented in part I; the eigenfrequencies are the modal phase-speeds $\omega_{kh,j}$.

$$\begin{aligned} \zeta(z,x_1,t)_{DVLA} &= \sum_{kh=kh_1}^{kh_2} \sum_{j=1}^{10} a_{kh,j}\phi(z)_{kh,j} e^{i(\omega_{kh,j}t+\theta_{kh,j})} \\ \zeta(z,x_2,t)_{UTP} &= \sum_{kh=kh_1}^{kh_2} \sum_{j=1}^{10} a_{kh,j}\phi(z)_{kh,j} e^{i(\omega_{kh,j}t+\theta_{kh,j}+\mathbf{kh}_{kh,j}\cdot\mathbf{r})} \end{aligned} \tag{4.1}$$

where $\mathbf{r}$ is the vector pointing from the position of the DVLA to the approximate position of the UTP for path ID-3. There are several parameters that may be adjusted in a model of this kind: the mode amplitudes and phases (possibly including some sort of randomness), the number of modes, and the directions of the waves. There are two questions that this section endeavors to address: "how well-correlated is the internal-tide-induced sound-speed variability at the positions of the DVLA and the path ID-3 UTP?", and "if the variability between the two positions is well-correlated, how large is the lag in time for maximum correlation?". Both questions will depend on the direction of the wave; for example, there is perfect correlation at zero lag parallel to a wavefront, for waves that are all going in the same direction. The phases and amplitudes of the waves should affect the correlation. The frequency-dependence

of the energy content of the waves is important for both questions because different spatial scales (wavelengths) will be more or less prevalent.

Though it may be possible to make a likely model in terms of these variables, the approach taken here was to try some realistic values or ranges of values for each, and perform a (200) Monte Carlo simulation on the phase of the waves. The direction of propagation of the diurnal and semidiurnal internal-tide constituents was estimated by fitting an ellipse to the current direction each day for YD 116 through YD 119. Currents were either band-pass filtered for the diurnal or semidiurnal frequency before the fit was calculated. Only waves at these two constituent frequencies are included in the model.

Four scenarios were considered with regard to the internal-tide model. In the first scenario, the direction vector for the waves was the estimate of the direction of the semimajor axis of the diurnal ellipse for each of the four days, and the diurnal component was given more power than the semidiurnal component. The second scenario was the same as the first, except that equal power was given to diurnal and semidiurnal components. The third scenario had different directions for the diurnal and semidiurnal waves, again estimated from the ellipse fits to the currents—and more power in the diurnal than semidiurnal components. The fourth scenario was the same as the third, except that equal power was given to the diurnal and semidiurnal waves. To summarize, each scenario had either equal or unequal power in the diurnal and semidiurnal, and the same, or different directions; in all cases the directions for the four days were estimated from the currents at the DVLA by fitting an ellipse to those currents and taking the semimajor axis direction as the direction for the waves.

In all scenarios, the relative power given to each mode was given by the relation

$$H(j) = \frac{h_{norm}}{j^2 + j_*^2} \tag{4.2}$$

where h_{norm} is set to make the sum over modes equal to unity. The phase in all cases was a random number from a uniform distribution with $0 \leq \theta < \pi$. The phase was matched for the diurnal and semidiurnal components for all modes, then advanced at the phase speed appropriate for each mode and frequency for the approximate distance from the Luzon Strait to the DVLA (ζ_{DVLA}) and then advanced further for the projection of the wave direction onto the DVLA-UTP direction vector (ζ_{UTP}).

Each displacement time-series was converted to a sound-speed perturbation by multiplication by the potential sound speed gradient $\mathrm{d}\bar{c}_{Pot.}/\mathrm{d}z$, calculated from the smooth, average profile. Example time-series for one of the four scenarios appears in figure 4.15.

The lag which maximized the correlation between the sound-speed perturbation at the DVLA and ID-3 UTP positions was calculated at each depth

$$\tau_* = \arg\max_{\tau} R_{\delta c_{DVLA}\delta c_{UTP}}(\tau) \tag{4.3}$$

where R is the cross-correlation sequence. A positive lag indicates that the displacement at the ID-3 UTP position correlates best with the sound speed perturbation at a later time at the DVLA. The maximum correlation at each depth for the Monte Carlo simulations for each of the four scenarios is shown in figure 4.16. The lag at each depth, for each simulation, that gave the maximum correlation is shown in figure 4.17.

4.6 Discussion

The mesoscale variability that was evident in figure 4.2 is not necessarily indicative of the presence of an eddy, but could instead be explained as linear Rossby waves. Linear vs. nonlinear waves are distinguished in this case by the metric U/C, where U is the maximum rotational fluid velocity in the interior of the possible eddy, and C is

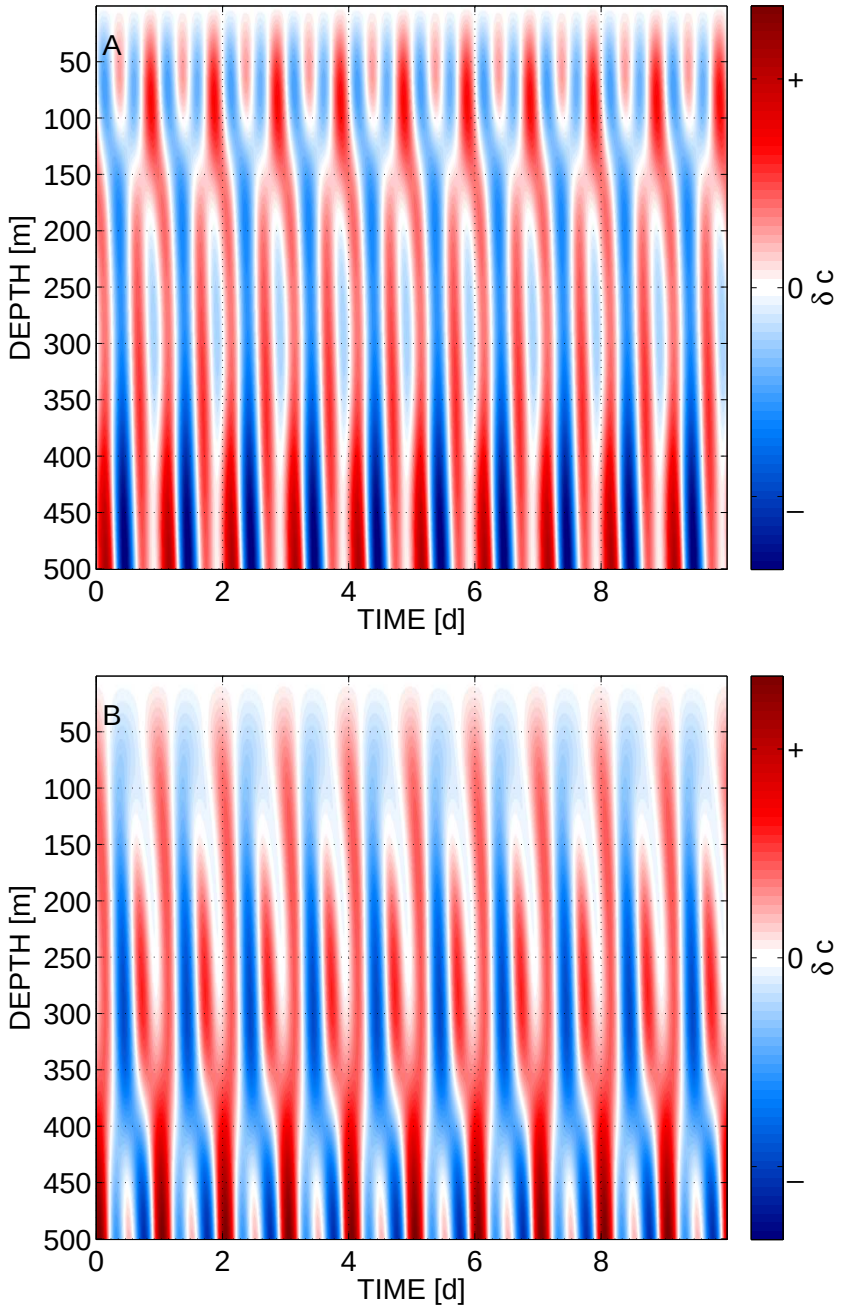

Figure 4.15: Comparison of example sound speed perturbation time-series for the upper 500 m at the DVLA (panel A) and at the ID-3 UTP position (panel B) for a single realization of the internal tide model. The comparison shown here is one of the four scenarios with lower correlation: power in the diurnal and semidiurnal components is equal, the angle is such that the projected distance between the DVLA and the ID-3 UTP is greatest, and the diurnal and semidiurnal contributions are coming from different horizontal directions. In the models with the highest correlations, the waves arrive at the two positions simultaneously, the diurnal component has greater power, and the diurnal and semidiurnal waves are in the same horizontal direction.

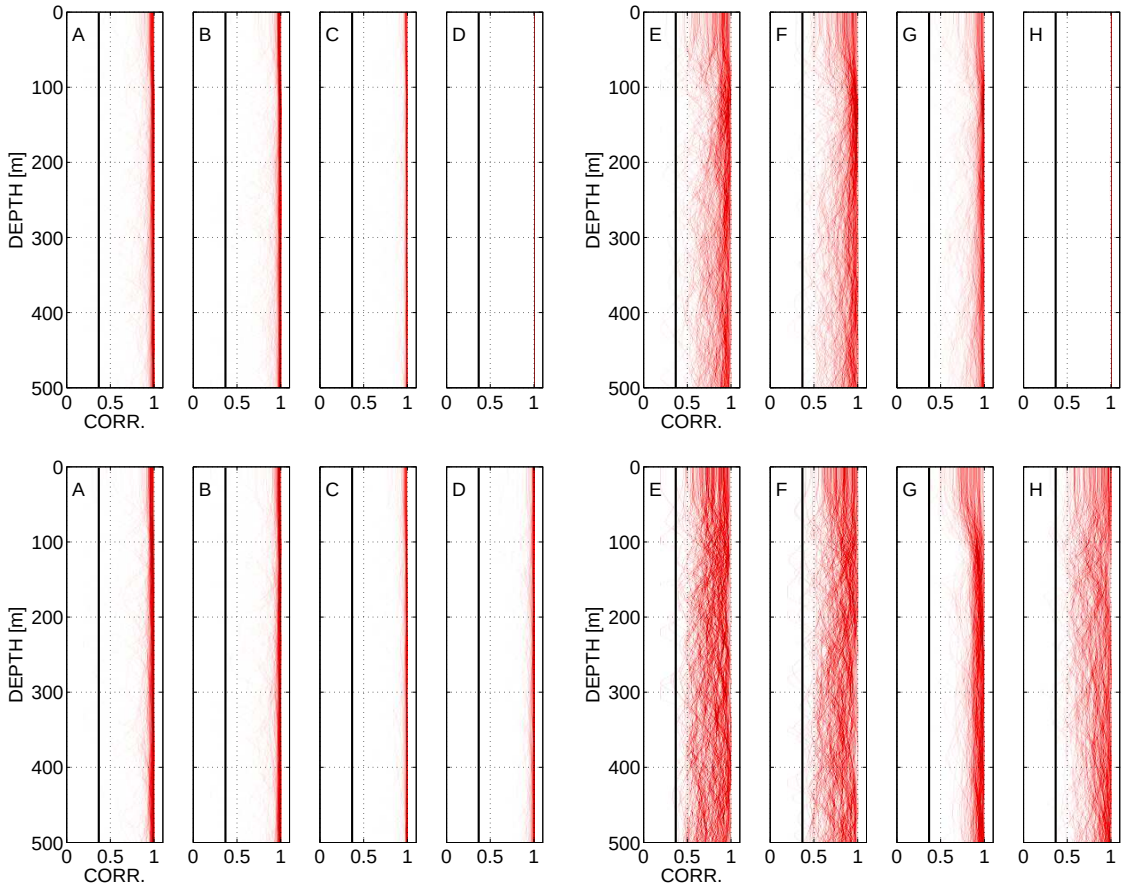

Figure 4.16: Monte Carlo histograms of correlation value vs. depth. Panels A-D in each row show the Monte Carlo histogram (200 samples) of the correlation value vs. depth for models with greater power in the diurnal contribution than that in the semidiurnal. Panels E-H in each row show the same for a model with equal power in diurnal and semidiurnal contributions. Panels A-D show the results for models corresponding to YD 116-119, respectively—panels E-H are in the same order, with each panel representing one day. The direction of the waves was set by the estimate of the current ellipse semi-major axis direction for each day (with separate estimates for diurnal and semidiurnal components; in some models the direction for the diurnal and semidiurnal components were set to the separately-estimated directions for each component, while in other models the diurnal direction was given to both components). The top row of plots show models with diurnal and semidiurnal contributions having the same horizontal direction, and the bottom row of plots show models with different horizontal directions for diurnal and semidiurnal components. The vertical black line indicates the value of 1/e in all plots.

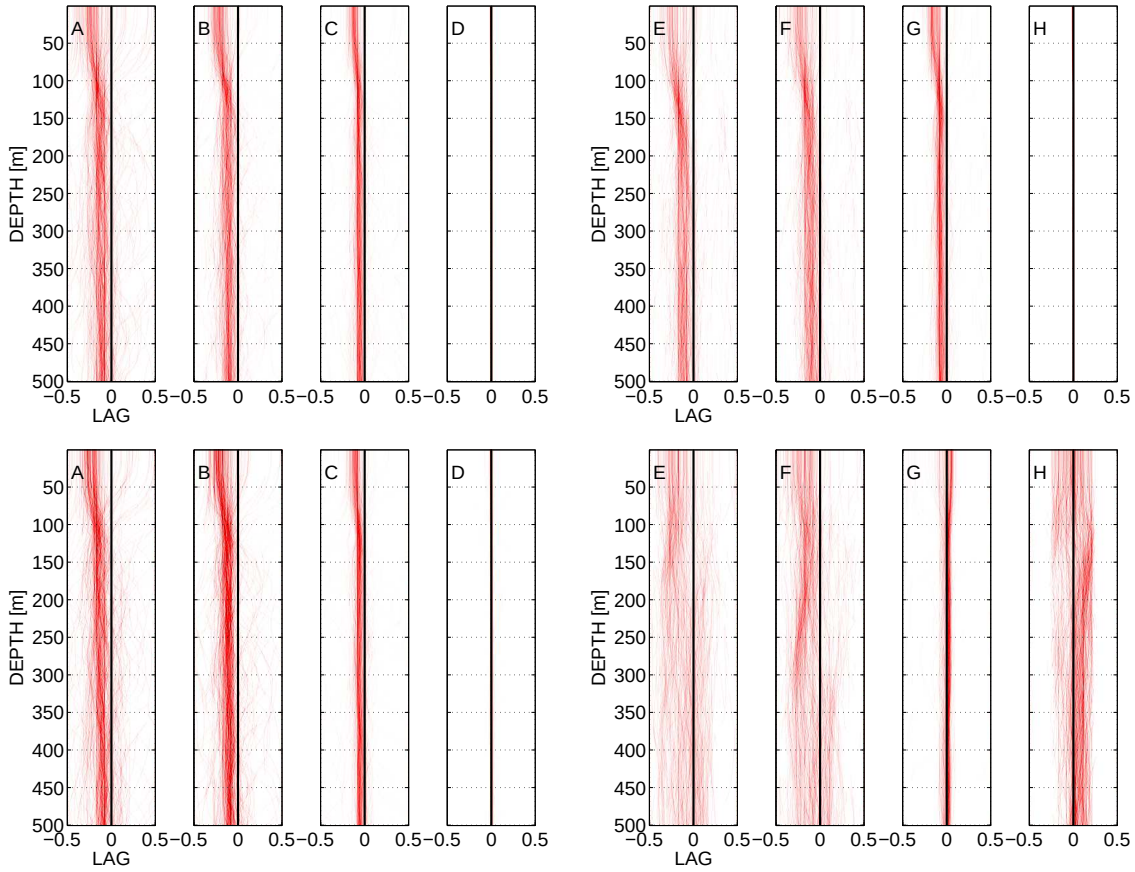

Figure 4.17: Monte Carlo histograms of lag value (in days) vs. depth. Panels A-D in each row show the Monte Carlo histogram (200 samples) of the lag value τ_* vs. depth for models with greater power in the diurnal contribution than that in the semidiurnal. Panels E-H in each row show the same for a model with equal power in diurnal and semidiurnal contributions. Panels A-D show the results for models corresponding to YD 116-119, respectively—panels E-H are in the same order, with each panel representing one day. The direction of the waves was set by the estimate of the current ellipse semi-major axis direction for each day (with separate estimates for diurnal and semidiurnal components; in some models the direction for the diurnal and semidiurnal components were set to the separately-estimated directions for each component, while in other models the diurnal direction was given to both components). The top row of plots show models with diurnal and semidiurnal contributions having the same horizontal direction, and the bottom row of plots show models with different horizontal directions for diurnal and semidiurnal components. The vertical black line indicates the value of 0 in all plots.

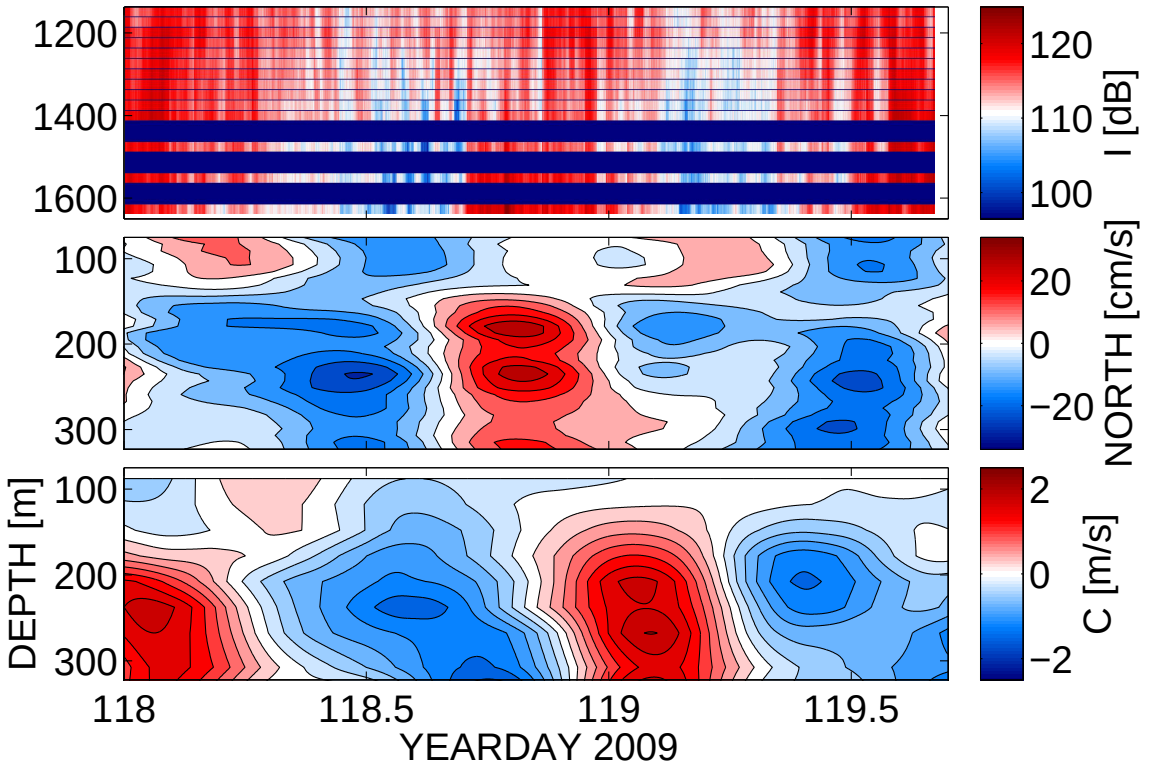

Figure 4.18: Comparison of ID-3 intensities with the northward current and sound-speed fluctuations measured at the DVLA. Shown in the top panel are intensity time-series of ID-3 at depths and times that fades were observed. The middle and bottom panels show the northward component of current velocity and the sound speed measured at the DVLA for the same time period; both were band-passed for periods from 12 h to 24 h.

its translational speed (Fu et al., 2010). The strength of the non-linearity determines whether the particular feature could be classified as a coherent vortex that could trap and transport water (Samelson and Wiggins, 2006) from another location (thereby providing a potential large-scale inhomogeneity in the sound-speed field), or as some transient event which may not have as significant of an effect on the sound-speed field. While one might attempt to calculate this metric for the features seen in the SSH measurements, the point seems moot; whether or not the features are *actually* propagating, coherent eddies would not affect the fact that substantial changes in the measured properties of temperature and salinity (and therefore sound speed) do appear to be associated with them.

What is clear is that a mass of warmer, saltier water passed by the upper few hundred meters of the DVLA position at the same time as an increase in elevation of the SSH was observed. This was followed by a nearly 10 d-long period during which the vertical gradient in sound speed was observed to be much weaker than it had been previously. It was during this time that the acoustic transmissions were made, and path ID-3 was seen to experience intensity fading of around 10 dB. Associated with the decreased vertical gradient (or, alternatively, with the slower sound speed) intensity predictions for individual profiles were decreased by 10 dB relative to the prediction for the smooth, average profile. The temporal modulation that is observed in the ID-3 time-series could be caused by vertical displacements by internal tides resulting in changes in the sound speed profile.

With regard to the predictions of intensity vs. mixed-layer depth, the predicted decrease in intensity seen in figure 4.14 is of somewhat lesser magnitude than the observed fades, given the deepest observed mixed-layer depth of 80 m from 2009. Of course, there is significant range-dependence in the actual ocean, which would change the received intensity in some unknown way. Unfortunately, this range-dependence is

not known well enough to build a corresponding model. A major problem with the hypothesis that interaction with the mixed layer alone could have caused the fades is that the mixed layer should be deepest in the early morning hours before the sun rises, but the fades occurred during local daylight hours. Shipboard measurements of wind speed, short- and long-wave radiation, precipitation, surface temperature, and currents were also examined (shown in appendix E). Nothing in these records seemed to correlate well in time with the fades, or otherwise suggest any reason to expect that the (strictly-defined) mixed layer depth deepened beyond 80 m during the acoustic transmissions.

An ocean model that contained a mixed layer with forcing due solely to random "background" internal waves would be missing the great majority of the physics that are known to drive changes in the mixed layer depth. Internal waves are known to perturb the base of the mixed layer, but a model in which diffuse internal waves provided the only forcing would be unrealistic compared to a more complete model that included, for example, surface heat fluxes. The processes that force the mixed layer are quite different than those causing sound speed inhomogeneities at deeper depths. The primary physics behind those changes is the diurnal pattern of heat input from solar radiation, which in turn causes stratification, followed by mixing through convective overturning when the heat input ceases at night. Also important could be wind stress. Inclusion of these would involve construction of a much more complicated model than the one used in this work.

Similarity between the spectra of vertical displacement and current spectra (not shown) suggests that the internal tides explain the (tidal-timescale) currents: the vertical displacement would not be present if the currents were caused by the barotropic tides. The angle of orientation of the semimajor axes from the ellipse fits to the diurnal currents varied by less than 20° from YD 116 to YD 119, and for the semidurnal

by less than 40°. The internal-tide model makes several approximations. The first approximation is to assume plane waves, which is not an unreasonable starting point, given that the unknown refractive effect of mesoscale variability on internal tides is a current research topic, and given a lack of detailed information regarding this variability. Rainville and Pinkel (2006) developed a ray model to study the refractive effect of mesoscale currents on internal-tide propagation, and found that mode one was only slightly affected, but the phases of higher modes (three and above) were randomized. Colosi et al. (2013) found evidence of spatial dependence of the internal tides in the Philippine Sea while comparing the DVLA measurements to measurements made at the T1 mooring mentioned earlier, pictured in figure 2.1.

The internal-tide modeling presented in this thesis predicted that the correlation between sound-speed perturbations from internal tides at the positions of the DVLA and ID-3 UTP should be high. Therefore, the measurements at the DVLA should be good predictors of what happened at the ID-3 UTP. However, the model also showed that a lag of up to half a day would be possible, given uncertainties in the model parameters. The strongest effect on correlation between sound-speed perturbations at the two positions was the relative strengths of the diurnal vs. semidiurnal components. The lag between high correlation values at the two positions depended mostly on the direction of the waves. The timescale of the fades compares well with that of the tidal current and sound-speed fluctuations measured at the DVLA. The possibility of a lag between the two positions does not allow elimination of the hypothesis that the internal tides caused the fades, based on the comparison of the timing of the measured environmental fluctuations to the timing of the fades.

Current shear may become important to acoustic propagation where the vertical gradient of sound speed is smaller than the vertical current shear. This effect could become important when the ratio of the vertical sound-speed gradient over the buoy-

ancy frequency is of order one (Sanford, 1974). This criterion is met by the smooth, averaged profile used in propagation calculations in this thesis. Clearly, in the upper ocean (where the buoyancy frequency is greatest), several of the profiles taken during PhilSea09 exhibited regions in the vertical with little or no change in sound speed. The internal-tide currents then give an effective reduction or augmentation in sound speed, causing ducting. Ducting may alternatively occur when the internal-tide-related sound-speed perturbation causes the already weak vertical gradient to become very small or slightly positive with increasing depth; the acoustic path then changes such that some energy is ducted, yielding a reduction in intensity.

Acoustic propagation as modeled in this thesis has all been restricted to a vertical plane. In the case of the background internal waves, this seems reasonable for the following reason: the vertical correlation length for vertical displacements (which provide the greatest part of sound-speed perturbations) is on the order of 100 m, while the horizontal correlation length scale is closer to a few km. In the presence of strong local internal tides, it seems likely that the horizontal correlation function would be anisotropic. The direction of acoustic propagation relative to the direction of the internal tides could then become important—though it is difficult to see how this might *decrease* the correlation length in the horizontal. The possibility remains that the internal tides imparted some (deterministic, strong—relative to the diffuse internal waves) range- and un-modeled time-dependence to the sound-speed field.

4.7 Conclusions

The depth-dependence of the intensity fades (increasing with depth over the span of the upper array) predicted by the mixed-layer modeling is consistent with the observations, though the magnitude is a few dB less than the observations. A model of mixed-layer depth driven primarily by diurnal heating would be inconsistent with

the timing of the observed fades. The sound-speed perturbations at the DVLA are observed to be smaller in the depth range from 90 m to 150 m after the warm-water mesoscale feature passes over the DVLA, while the vertical gradient in sound-speed is observed to also be smaller during the same period.

A simple plane-wave internal-tide model predicts high correlation between tidally-induced sound-speed perturbations at the DVLA and at the ID-3 UTP, along with a possible time lag—depending mostly on the horizontal directions of the diurnal and semidiurnal tidal components. Modeling of acoustic mode propagation through range-independent individual measured sound-speed profiles suggests that profiles with slower sound speed near the ocean's surface, or with diminished vertical gradients would be susceptible to intensity fading through ducting or focusing/de-focusing of acoustic energy. Internal-tide currents could possibly play a role in the process if the direction has a strong component in the direction of acoustic propagation—though it seems possible that the sound-speed perturbations due to internal-tide vertical displacements alone could provide the observed temporal modulation in the measured intensity time-series for path ID-3.

Chapter 5

CONCLUSIONS

5.1 Conclusion

One of the goals of the PhilSea09 pilot study/engineering test was to test the viability of a Monte Carlo method with random GM internal waves for predicting intensity fluctuations. The model was to be tested for time-independent (SI and variance of log-intensity) and time-dependent measures (the power spectral density and temporal autocorrelation function of intensity). The first test was passed for paths ID+4, ID-4, and ID+5 at all hydrophone depths considered in the analysis—and for path ID-3 for about half of the depths. The second test was complicated by gaps in transmission due to equipment failure and due to interfering signals in the water, of unknown origin. MCPE predictions for the power spectrum and temporal autocorrelation function have been computed (shown in appendix D). Attempts to understand the gaps' effect on these quantities were made, but a more-satisfactory solution to the "gappy-data" problem is left as future work. A cumulative effect of UTP number on the time-independent statistics was not observed. Finally, the relation between some effects of un-modeled features of the environment and the intensity fades observed in path ID-3 was explored. These features that were studied included a surface mixed, or weakly-stratified layer and internal tides. Some combination of these features seems a plausible explanation for the fades, though without further measurement the cause cannot be known conclusively.

5.2 Direction for future work

In the near-term, i.e. the next two years, future work will be comprised of two parallel efforts: to further study the possible effects of the strong local internal tides on the intensity, and to explore the effect of the range-dependence due to the energetic mesoscale in the Philippine Sea. In 2010, a 510 km-long transect of vertical CTD casts was made as part of the full experiment conducted there, with casts taken

every 10 km. This set of measurements will provide a more-complete picture of the range-dependence than was available from PhilSea09. Simulation of broadband propagation through an ocean with and without this range-dependence may be compared with measurements made in 2010 of acoustic transmissions over a 500 km path. The GM model makes an assumption of horizontal isotropy; internal tides radiating from the Luzon Strait, the Mariana Island Arc, and the Kyukyu Islands could violate this assumption. A final question is whether propagation in the horizontal would need to be considered in this region with such strong mesoscale and possible horizontal anisotropy. The Office of Naval Research has funded a two-year post-doctoral appointment for me to carry out work focusing on the effects of range-dependence and internal tides on acoustic propagation in the Philippine Sea.

It is interesting that the TD MCPE spectra fall increasingly rapidly with increasing frequency, as was shown in figure 3.13 and 3.14. If the problem of bias in the spectrum due to gaps in the transmission schedule can be overcome, it would be perhaps surprising if the measured spectrum agrees with this prediction. An attempt to either piece together a spectrum using subsets of the PhilSea09 intensity data, or to implement the method suggested by Bronez (1988) should definitely be attempted, given the time-investment that was already made. A solution of the gappy-data problem would turn chapter 3 into a packaged, complete study, ready for submission to a journal.

It is apparent in figures 3.1–3.4 that there is correlation in the vertical direction between the records of intensity at various depths. It will be possible to compute predictions and estimates of the vertical correlation function of intensity from the simulated and measured data-sets that were contributed by this thesis work.

In the longer-term, more experiments will be necessary to understand the larger questions about how intensity is affected by the ocean's variability. Those larger ques-

tions include: How do intensity fluctuations develop with range? E.g. Are shadow-zone arrivals a cumulative effect with increasing propagation range, or number of UTP?; How does the sound-speed profile affect the depth-dependence of intensity fluctuations (as in the deep fades, for example)? What exactly causes deep fades at short range, such as 107 km? The idea of PhilSea09 was to compare the amounts of fluctuation induced by one or a few UTP; with more resources, this experiment could easily and cheaply be improved upon. Probably the greatest improvement in the experiment would be to have one or two vertical moorings positioned at the ranges of UTP for a couple of the acoustic paths. These moorings would be approximately 5 km tall and the UTP are further apart than this distance so there wouldn't be a danger of them tangling. The moorings should make measurements of the same type and of the same temporal and spatial frequency as those taken with the sensors on the DVLA: temperature, salinity, and pressure— combined with ADCP measurements of current velocity. A lack of knowledge of what was happening at the UTP was probably the obstacle to understanding the deep fades. These measurements, along with enough CTD stations to quantify the range-dependence and a similar propagation range to that used in PhilSea09 should help to unravel specifically the question of the depth-dependence of intensity fluctuations, of which the deep fades were a perfect example.

BIBLIOGRAPHY

M.A. Ainslie. *Principles of Sonar Performance Modelling*. Springer-Praxis books in geophysical sciences. Springer Berlin Heidelberg, 2010.

M. H. Alford, J. A. MacKinnon, J. D. Nash, H. Simmons, A. Pickering, J. M. Klymak, R. Pinkel, O. Sun, L. Rainville, R. Musgrave, T. Beitzel, K. Fu, and C. Lu. Energy flux and dissipation in Luzon Strait: Two tales of two ridges. *J. Phys. Oceanogr.*, 41(11):2211–2222, 2011.

Matthew H. Alford. Improved global maps and 54-year history of wind-work on ocean inertial motions. *Geophysical Research Letters*, 30(8):n/a–n/a, 2003.

R. K. Andrew. The APL/UW multiport acoustic projector system. Technical Report APL/UW TR-0902, Applied Physics Laboratory, University of Washington, Seattle WA, 2009.

R. K. Andrew, B. M. Howe, J. A. Mercer, The NPAL Group (J. A. Colosi, B. D. Cornuelle, B. D. Dushaw, M. A. Dzieciuch, B. M. Howe, J. A. Mercer, W. H. Munk, R. C. Spindel, and P. F. Worcester). Transverse horizontal spatial coherence of deep arrivals at megameter ranges. *J. Acoust. Soc. Am.*, 117(3): 1511–1526, 2005.

R. K. Andrew, A. W. White, J. A. Mercer, P. F. Worcester, M. A. Dzieciuch, and J. A. Colosi. Theoretical fluctuation predictions for low-frequency acoustical propagation ranges of 25 to 107 km in the 2009-2010 Philippine Sea experiment. *J. Acoustic. Soc. Am.*, 131:3354–3354, 2012.

R.K. Andrew, M.R. Zarnetske, B.M. Howe, and J.A. Mercer. Ship-suspended acoustical transmitter position estimation and motion compensation. *Oceanic Engineering, IEEE Journal of*, 35(4):797–810, 2010.

J.R. Apel. *Principles of Ocean Physics*. International Geophysics. Elsevier Science, 1987.

Aviso and support from Cnes. Ssalto and Duacs products. http://www.aviso.oceanobs.com/duacs, 2012. last accessed March 24, 2012.

J. S. Bendat and A. G. Piersol. *Random Data, Analysis and Measurement Procedures*. John Wiley & Sons, Inc., 1986.

T. G. Birdsall. Signals and signal processing for acoustic monitoring of ocean processes. In *1995 International Conf. on Acoustics, Speech, and Signal Processing*, pages 2767–2770. IEEE, Detroit MI, 1995.

T. G. Birdsall and K. Metzger. Factor inverse matched filtering. *J. Acoust. Soc. Am.*, 79(1):91–99, 1986.

T. G. Birdsall and K. Metzger. M-sequence signal tutorial. In *Naval Oceanographic Office presentation*. Communications and Signal Processing Laboratory, EECS Department, University of Michigan, Ann Arbor MI, 1988.

James B. Bowlin, John L. Spiesberger, Timothy F. Duda, and Lee F. Freitag. Ocean acoustical ray-tracing software ray. Technical Report WHOI-93-10, October 1992.

T.P. Bronez. Spectral estimation of irregularly sampled multidimensional processes by generalized prolate spheroidal sequences. *Acoustics, Speech and Signal Processing, IEEE Transactions on*, 36(12):1862–1873, 1988.

George M. Bryan, Marek Truchan, and John I. Ewing. Long-range sofar studies in the south atlantic ocean. *The Journal of the Acoustical Society of America*, 35(3):273–278, 1963.

V. Cojbasic and A. Tomovic. Nonparametric confidence intervals for population variance of one sample and the difference of variances of two samples. *Comp. Stat. Data Anal.*, 51(12):5562–5578, 2007.

M. D. Collins. A split-step padé solution for the parabolic equation method. *J. Acoust. Soc. Am.*, 93:1736–1742, 1993.

J. A. Colosi and M. G. Brown. Efficient numerical simulation of stochastic internal-wave-induced sound-speed perturbation fields. *J. Acoust. Soc. Am.*, 103 (4):2232–2235, 1998.

J. A. Colosi, S. M. Flatté, and C. Bracher. Internal wave effects on 1000 km oceanic acoustic pulse propagation: Simulation and comparison with experiment. *J. Acoust. Soc. Am.*, 96(1):452–468, 1994.

J. A. Colosi, J. Xu, P. F. Worcester, M. A. Dzieciuch, B. M. Howe, and J. A. Mercer. Temporal and vertical scales of acoustic fluctuations for 75-Hz, broadband transmissions to 87-km range in the eastern North Pacific Ocean. *J. Acoust. Soc. Am.*, 126(3):1069–1083, 2009.

J. A. Colosi, B. D. Dushaw, L. J. Van Uffelen, B. D. Cornuelle, M. A. Dzieciuch, P. F. Worcester, S. R. Ramp, and F. Bahr. Observed sound speed structure during the Phil Sea 2009-2011 field years. *J. Acoust. Soc. Am.*, 131:3353(A), 2012.

J. A. Colosi, L. J. Van Uffelen, B. D. Cornuelle, M. A. Dzieciuch, P. F. Worcester, B. D. Dushaw, and S. R. Ramp. Observations of sound-speed fluctuations in the western Philippine Sea in the spring of 2009. *J. Acoust. Soc. Am.*, special issue (special issue), 2013.

A. C. Davison and D. V. Hinkley. *Bootstrap Methods and their Applications*, chapter 8, pages 385–436. Cambridge Series in Statistical and Probabilistic Mathematics, Cambridge University Press, Cambridge UK, 1997.

T. F. Duda, S. M. Flatte, J. A. Colosi, B. D. Cornuelle, J. A. Hildebrand, Jr. W. S. Hodgkiss, P. F. Worcester, B. M. Howe, J. A. Mercer, and R. C. Spindel. Measured wave-front fluctuations in 1000-km pulse propagation in the pacific ocean. *The Journal of the Acoustical Society of America*, 92(2):939–955, 1992.

B. D. Dushaw. Multimegameter-range acoustic data obtained by bottom-mounted hydrophone arrays for measurement of ocean temperature. *J. Ocean. Eng.*, 24(2):202–214, 1999.

G. D. Egbert and R. D. Ray. Significant dissipation of tidal energy in the deep ocean inferred from satellite altimeter data. *Nature*, 405(6788):775–778, 2000.

C.C. Eriksen, T.J. Osse, R.D. Light, T. Wen, T.W. Lehman, P.L. Sabin, J.W. Ballard, and A.M. Chiodi. Seaglider: a long-range autonomous underwater vehicle for oceanographic research. *Oceanic Engineering, IEEE Journal of*, 26(4): 424–436, 2001.

T. E. Ewart. Acoustic fluctuations in the open ocean—a measurement using a fixed refracted path. *J. Acoust. Soc. Am.*, 60(1):46–59, 1976.

T. E. Ewart and S. A. Reynolds. The mid-ocean acoustic transmission experiment, MATE. *J. Acoust. Soc. Am.*, 75(3):785–802, 1984.

M. Ewing and J. L. Worzel. *Long-range sound transmission*, volume 27, part III of *Geological Society of America Memoir*. GSA, 1948.

R. P. Feynman. Forces in Molecules. *Phys. Rev.*, 56(4):340–343, 1939.

S. M. Flatté, R. Dashen, W. H. Munk, K. Watson, and F. Zachariasen. *Sound Transmission through a Fluctuating Ocean*. Cambridge University Press, Cambridge UK, 1979.

K. M. Freitas. Improving accuracy of acoustic prediction in the Philippine Sea through incorporation of mesoscale environmental effects. Master's thesis, Naval Postgraduate School, Monterey CA, 2008.

L.-L. Fu, D.B. Chelton, P.-Y. Le Traon, and R. Morrow. Eddy dynamics from satellite altimetry. *Oceanography*, 23(4):14–25, 2010.

Tom Garrison. *Oceanography: An Invitation to Marine Science*. Brooks/Cole—Thomson Learning, 5 edition, 2005.

S. A. L. Glegg. The de-dopplerization of acoustic signals using digital filters. *Journal of Sound and Vibration*, 116(2):384–387, 1987.

Allan R. Gondeck. Doppler time mapping. *The Journal of the Acoustical Society of America*, 73(5):1863–1864, 1983.

K. C. Hegewisch, N. R. Cerruti, and S. Tomsovic. Ocean acoustic wave propagation and ray method correspondence: Internal wave fine structure. *J. Acoust. Soc. Am.*, 117(3):1582–1594, 2005.

F. S. Henyey. Vertical CTD analysis. *J. Acoust. Soc. Am.*, special issue(special issue), 2012.

F. S. Henyey and S. A. Reynolds. A Numerical Simulator of Ocean Internal Waves for Long-Range Acoustics. Technical Report APL-UW TM 1-13, Applied Physics Laboratory, University of Washington, Seattle WA, 2013.

F. S. Henyey, D. Rouseff, J. M. Grochocinski, S. A. Reynolds, K. L. Williams, and T. E. Ewart. Effects of internal waves and turbulence on a horizontal aperture sonar. *J. Ocean. Eng.*, 22(2):270–280, 1997.

Bruce M. Howe, Peter F. Worcester, and Robert C. Spindel. Ocean acoustic tomography: Mesoscale velocity. *Journal of Geophysical Research: Oceans*, 92 (C4):3785–3805, 1987.

Finn Bruun Jensen. *Computational Ocean Acoustics*. AIP series in modern acoustics and signal processing. American Institute of Physics, 1994.

F. Kobashi and H. Kawamura. Variation of sea surface height at periods of 65-220 days in the subtropical gyre of the North Pacific. *J. Geophys. Res.*, 106 (C11):26817–26831, 2001.

M. D. Levine. A modification of the garrettmunk internal wave spectrum. *Journal of Physical Oceanography*, 32(11):3166–3181, 2002.

J. A. Mercer and J. R. Booker. Long-range propagation of sound through oceanic mesoscale structures. *J. Geophys. Res.*, 88(C1):689–699, 1983.

J. A. Mercer, R. K. Andrew, B. M. Howe, and J. A. Colosi. Cruise report: Long-range ocean acoustic propagation experiment (LOAPEX). Technical Report APL-UW TR-0501, Applied Physics Laboratory, University of Washington, Seattle WA, 2005.

J. A. Mercer, J. A. Colosi, B. M. Howe, M. A. Dzieciuch, R. Stephen, and P. F. Worcester. LOAPEX: the long-range ocean acoustic propagation experiment. *J. Ocean. Eng.*, 34(1):1–11, 2009.

R. Morrow and P.-Y. Le Traon. 15 years of satellite alimetry and mesoscale ocean dynamics. In *ESA Special Publication*, volume 614 of *ESA Special Publication*, jul 2006.

W. H. Munk. Internal waves and small-scale processes. In C. Wunsch and B. Warren, editors, *The Evolution of Physical Oceanography*, pages 264–291. MIT Press, Cambridge MA, 1981.

W. H. Munk and F. Zachariasen. Sound propagation through a fluctuating stratified ocean: Theory and observation. *The Journal of the Acoustical Society of America*, 59(4):818–838, 1976.

W. H. Munk, P. F. Worcester, and C. Wunsch. *Ocean Acoustic Tomography*, pages 190–195. Cambridge University Press, Cambridge UK, 1995.

J. A. Nystuen. Listening to raindrops from underwater: an acoustic disdrometer. *J. Atmos. Oceanic Technol.*, 18(10):1640–1657, 2001.

D. B. Percival and A. T. Walden. *Spectral Analysis for Physical Applications: Multitaper and Conventional Univariate Techniques*. Cambridge University Press, Cambridge UK, 1993.

E. C. Pettit, J. A. Nystuen, and S. O'Neel. Listening to glaciers: Passive hydroacoustics near marine-terminating glaciers. *Oceanography*, 25(3):104–105, 2012.

G.L.A. Pickard and W.J. Emery. *Descriptive Physical Oceanography: An Introduction*. Butterworth-Heinemann, 1990.

R. Pinkel. Doppler sonar observations of internal waves: The wavenumber-frequency spectrum. *Journal of Physical Oceanography*, 14(8):1249–1270, 1984.

S.A. Pond and G.L.A. Pickard. *Introductory Dynamical Oceanography*. Pergamon international library of science, technology, engineering and social studies. Elsevier Butterworth-Heinemann, 1983.

M. B. Porter and E. L. Reiss. A numerical method for ocean-acoustic normal modes. *J. Acoust. Soc. Am.*, 76(1):244–252, 1984.

M. B. Porter and E. L. Reiss. A numerical method for bottom interacting ocean acoustic normal modes. *J. Acoust. Soc. Am.*, 77(5):1760–1767, 1985.

L. Rabiner, R.W. Schafer, and C.M. Rader. The chirp z-transform algorithm. *Audio and Electroacoustics, IEEE Transactions on*, 17(2):86–92, 1969.

L. Rainville and R. Pinkel. Propagation of low-mode internal waves through the ocean. *J. Phys. Oceanogr.*, 36(6):1220–1236, 2006.

S. A. Reynolds, S. M. Flatté, R. Dashen, B. Buehler, and P. Maciejewski. AFAR measurements of acoustic mutual coherence functions of time and frequency. *J. Acoust. Soc. Am.*, 77(5):1723–1731, 1985.

S. M. Rytov, Y. A. Kravtsov, and V. I. Tatarskii. *Principles of statistical radiophysics. 4. Wave propagation through random media.* 1989.

R.R.M. Samelson and S. Wiggins. *Lagrangian Transport in Geophysical Jets and Waves: The Dynamical Systems Approach.* Interdisciplinary Applied Mathematics. Springer Science+Business Media, LLC, 2006.

T. B. Sanford. Observations of strong current shears in the deep ocean and some implications on sound rays. *J. Acoust. Soc. Am.*, 56(4):1118–1121, 1974.

E. K. Skarsoulis and B. D. Cornuelle. Travel-time sensitivity kernels in ocean acoustic tomography. *The Journal of the Acoustical Society of America*, 116(1): 227–238, 2004.

A. Soloviev and R. Lukas. *The Near-Surface Layer of the Ocean, Structure, Dynamics and Applications*, chapter 1, page 63. Springer, 2006.

John Spiesberger. Regions where transient signals are influenced between a source and receiver. *The Journal of the Acoustical Society of America*, 119(5):3345–3345, 2006.

John L. Spiesberger. Where the ocean influences the impulse response and its effect on synchronous changes of acoustic travel time. *The Journal of the Acoustical Society of America*, 130(6):3642–3650, 2011.

Detlef Stammer and Carl Wunsch. Temporal changes in eddy energy of the oceans. *Deep Sea Research Part II: Topical Studies in Oceanography*, 46(1–2): 77–108, 1999.

P. J. Sutton, P. F. Worcester, G. Masters, B. D. Cornuelle, and J. F. Lynch. Ocean mixed layers and acoustic pulse propagation in the greenland sea. *The Journal of the Acoustical Society of America*, 94(3):1517–1526, 1993.

Philip J. Sutton, Werner M. L. Morawitz, Peter F. Worcester, and Bruce D. Cornuelle. Temperature evolution of the upper ocean in the greenland sea january to march 1989. *Journal of Geophysical Research: Oceans*, 102(C13):27861–27874, 1997.

Frederick D. Tappert. The parabolic approximation method. In J. B. Keller and J. S. Papadakis, editors, *Lecture Notes in Physics No. 70*, pages 224–287. Springer-Verlag, New York, 1977.

TEOS-10. Thermodynamic equation of state - 2010. `http://www.teos-10.org`, 2010. last accessed March 24, 2012.

L. J. Van Uffelen, Peter F. Worcester, Matthew A. Dzieciuch, Daniel L. Rudnick, and John A. Colosi. Effects of upper ocean sound-speed structure on deep acoustic shadow-zone arrivals at 500- and 1000-km range. *The Journal of the Acoustical Society of America*, 127(4):2169–2181, 2010.

Lora J. Van Uffelen, Peter F. Worcester, Matthew A. Dzieciuch, and Daniel L. Rudnick. The vertical structure of shadow-zone arrivals at long range in the ocean. *The Journal of the Acoustical Society of America*, 125(6):3569–3588, 2009.

R. J. Urick. *Principles Of Underwater Sound*, page 103. McGraw-Hill, Inc., 1975.

L. J. Van Uffelen. *Acoustic shadow-zone arrivals at long range in the North Pacific Ocean*. PhD thesis, Scripps Institution of Oceanography, UC San Diego, San Diego CA, 2009.

L. J. Van Uffelen, E. M. Nosal, B. M. Howe, G. S. Carter, P. F. Worcester, M. A. Dzieciuch, K. D. Heaney, R. L. Campbell, and P. S. Cross. Estimating uncertainty in subsurface glider position using transmissions from fixed acoustic tomography sources. *The Journal of the Acoustical Society of America*, 2013. accepted April 2013.

K. B. Winters and E. A. D'Asaro. Direct simulation of internal wave energy transfer. *J. Phys. Oceanog.*, 27:1937–1945, 1997.

M. A. Wolfson and J. L. Spiesberger. Full-wave simulation of the forward scattering of sound in a structured ocean: A comparison with observations. *J. Acoust. Soc. Am.*, 106(3):1293–1306, 1999.

P. F. Worcester. Reciprocal acoustic transmission in a midocean environment: Fluctuations. *J. Acoust. Soc. Am.*, 66(4):1173–1181, 1979.

P. F. Worcester and R. C. Spindel. North Pacific Acoustic Laboratory. *J. Acoust. Soc. Am.*, 117:1499–1510, 2005.

P. F. Worcester, B. D. Cornuelle, M. A. Dzieciuch, W. H. Munk, B. M. Howe, J. A. Mercer, R. C. Spindel, J. A. Colosi, K. Metzger, T. G. Birdsall, and A. B.

Baggeroer. A test of basin-scale acoustic thermometry using a large-aperture vertical array at 3250-km range in the eastern North Pacific Ocean. *J. Acoust. Soc. Am.*, 105(6):3185–3201, 1999.

P. F. Worcester, S. Carey, M. A. Dzieciuch, L. L. Green, D. Horwitt, J. C. Lemire, and M. Norenberg. Distributed vertical line array (DVLA) acoustic receiver. In J. S. Papadakis and L. Bjørnø, editors, *Proc. 3rd International Conf. on Underwater Acoustic Measurements*, pages 113–118. Foundation for Research and Technology Hellas, Nafplion Greece, 2009.

P. F. Worcester, R. K. Andrew, A. B. Baggeroer, J. A. Colosi, G. L. D'Spain, M. A. Dzieciuch, K. D. Heaney, B. M. Howe, J. N. Kemp, J. A. Mercer, R. A. Stephen, and L. J. Van Uffelen. The North Pacific Acoustic Laboratory (NPAL) deep-water acoustic propagation experiments in the Philippine Sea. *J. Acoust. Soc. Am.*, 131(4):3352(A), 2012.

J. Xu. *Effects of Internal Waves on Low Frequency, Long Range, Acoustic Propagation in the Deep Ocean*. PhD thesis, Massachusetts Institute of Technology, Cambridge MA, 2007.

Z. Zhao, M. H. Alford, and J.B. Girton. Mapping low-mode internal tides from multisatellite altimetry. *Oceanography*, 25(2):42–51, 2012.

A Pulse-compression

It will be helpful to model the transmitted m-sequence signal mathematically for the discussion of pulse-compression that follows. Fourier transforms of time-domain variables will be denoted by corresponding upper-case versions of each particular symbol.

Consider the base-banded continuous m-sequence $y(t)$, consisting of a square pulse p convolved with the series of delta functions m. $y(t)$ is given by

$$y(t) = p(t) * m(t) = p(t) * \sum_j a_j \delta(t - \tau_j) e^{\phi_j}$$

where the time between delta function positions τ_j is equal to the width of the square pulse, thus mapping the discrete m-sequence onto continuous time. The constants a_j are all equal to one in this case and ϕ_j are the phase jumps forward or backward by the angle ϕ_0. The base-banded m-sequence can then be represented in the Fourier domain as $Y = PM$, where P is a sinc function and the amplitude of the spectrum M of the continuous-time m-sequence is white. The amplitude spectrum of their product Y looks, then, like the sinc function—though the phase information describing the delta function positions and associated phase shifts is included in Y. Now consider a carrier at $f_0 = 284.166\,666\,\mathrm{Hz} = \omega_0/2\pi\ \mathrm{rad\,s^{-1}}$ which is a delta function at f_0 in the Fourier domain; convolution of the carrier with Y in the Fourier domain is equivalent to multiplication of its corresponding time-domain exponential $e^{i\omega_0 t}$ by y: $y_c(t) = y(t)e^{i\omega_0 t}$ and the amplitude spectrum of $y_c(t)$ is then the sinc function whose center has been shifted to frequency f_0.

M-sequences in this case are pulse-compressed using factor-inverse matched-filtering (FIMF) (Birdsall and Metzger, 1986); a description of this processing follows. Each hour-long recorded time-series of acoustic pressure is first resampled to a sample-rate

that is $f_{design} = 4f_0$. This sample-rate is required by the particular pulse-compression software that was used, and allows some computational short-cuts to be used. The resampled record is pulse-compressed in segments with length equal to the duration of one m-sequence. A given segment is first transformed to the spectral domain and base-banded $y_c \rightarrow y$. Next, a low-pass filter is applied to remove the upper sideband. An m-sequence is generated, then transformed to get its spectrum M. The transform Y of the heterodyned, filtered segment is then multiplied by M^{-1}. This operation is equivalent to deconvolution, and is the "factor-inverse" step in the processing.

Next, a square pulse is generated and transformed, yielding a sinc function P. Finally, the spectrum of the deconvolved segment of data is multiplied by the sinc function, giving (in the ideal case) a sinc^2 function. Since the product of two sinc functions in the spectral domain is equivalent to the convolution of two square pulses in the time domain, we obtain a triangle-shaped pulse in the time domain after performing an inverse Fourier transform. This final step of multiplication by a sinc function is not a necessary part of the pulse-compression; this step is only necessary if one prefers a triangular to a square pulse. The width of the triangle at its base is equal to twice the pulse width. Multiplication by P^* is the matched-filtering operation. This step was included because the pulse-compression software used in this thesis was developed previously for tomographic applications, where precise determination of travel-time is important, and it is easier to find the peak of a triangle than to find the leading edge of a band-limited (not square after the source response is considered—a detail here omitted for simplicity) pulse.

Mathematically, the pulse-compression applied to the PhilSea09 data may be represented as $Z = YP^*M^{-1}$, where P^* is the conjugate spectrum of a square pulse. Z is the spectrum of the deconvolved, matched-filtered m-sequence. Its inverse transform z is the pulse-compressed time-series with length equal to that of one m-sequence. z

is generally complex.

In the case of actual data, Y is the spectrum of the received signal, and has been affected by propagation through the ocean. Effects of propagation include: multi-path (a geometry-dependent feature), distortion of the pulse due to scattering, and Doppler effects due to motion of the ocean medium. Ambient noise at the receiving hydrophone is also present in the data. In PhilSea09 the source and receiver were not held perfectly stationary, and there was a concern that additional unwanted Doppler effects caused by equipment motion may be present in the received signal and may affect the pulse-compression. If the effect on the pulse-compression is large enough these equipment-caused Doppler effects could obscure the fluctuations that the experiment aimed to measure. An analysis of those effects is the topic of appendix B and reveals that in this case Doppler is insignificant.

B Doppler effects

B.1 Transmitter and receiver motion

The DVLA position was estimated once per hour using a surveyed long-baseline bottom-mounted transponder network. STAR controller modules (Worcester et al., 2009) that were positioned at the top of each of the two sub-arrays of the DVLA emitted high-frequency chirps; the bottom-mounted transponders replied and the travel-time was used to compute a solution for the STAR controller at each hour throughout the duration of the DVLA's deployment. The horizontal position of the DVLA varied by up to several hundred m and in the vertical by up to 90 m.

As was mentioned in section 2.2.1, the acoustic transmitter MP200/TR1446 that was deployed over the stern of the R/V *Melville* was tracked by a similar surveyed bottom-mounted long-baseline transponder network, except that only two transponders were used at SS107. The transponders were located along the geodesic connecting the position SS107 with the DVLA's position. The estimated track of the MP200/TR1446's position is not well-constrained in the direction orthogonal to the vertical plane through that geodesic. Nevertheless, velocities computed from the position estimate of the MP200/TR1446 may be used to put a bound on the amount of expected degradation in pulse-compression for PhilSea09 due to the associated Doppler effect. The time-series of the projection onto the ID-3 direction vector was made from an approximately 40 h-long source velocity estimate.

DVLA velocities estimated from the track of the STAR controller for the upper sub-array were seen to be much smaller in magnitude than the velocities experienced by the MP200/TR1446. Ocean currents associated with local internal tides are implicated in the DVLA motion; motion of the ship due to passing waves and to near-surface currents contributed to the relatively higher speeds of the acoustic trans-

mitter. Motions of the DVLA are therefore ignored for the purposes of this study, and only motion of the MP200/TR1446 will be considered.

First, a general idea about how the pulse-compressor performance degrades due to Doppler effects is studied. Next, a 40 h-long estimate of the MP200/TR1446 velocity is used to generate some statistical measure of the percent of data that is expected to be affected by Doppler effects from transmitter motion, to within a threshold value in dB. A short discussion of how to compute SNR is included in the chapter, followed by some investigation into maximizing SNR via a Doppler-search. Finally, cross-correlations of speeds inferred from a Doppler-search which maximize SNR for individual paths are described.

B.2 Pulse-compressor performance: approach

Two approaches were taken to make a statistical description of the expected degradation in pulse-compression due to Doppler effects. The first approach involves making the assumption that each velocity estimated from the 40 h-long track was constant over the duration of an m-sequence. This is not a valid assumption, given that the length of the m-sequences was 7.2 s—compared to transmitter motions in the vertical on timescales of under ten seconds due to heave and in the horizontal on timescales of tens of seconds due to surface currents. Such a model is easy to make, however, and may be compared to a more complicated model, considered in the second approach.

In the first approach, speed v is computed with the equation $df/f_0 = v/C$, where v/C is the local Mach number, and df/f_0 is the fractional change in frequency due to the Doppler effect. The transmitter is free to move in any direction, but the projection of the transmitter's velocity onto the unit vector in the direction of a particular acoustic path leaving the transmitter is used. The projection is onto the direction vector for path ID-3 , since this path makes the greatest angle to the horizontal and

the greatest speeds of the source were in the vertical direction; the aim is to establish an upper bound on the effect. The projection will be denoted v.

Next, a range of frequencies f_{test} near the PhilSea09 carrier frequency of f_0 was chosen, a continuous m-sequence generated for each frequency in that range (sampled at $f_{design} = 4f_0$), and then each m-sequence was pulse-compressed. A curve relating pulse-compressed intensity (intensity of the peak) to projected transmitter speed v was thus made. This curve was then interpolated at each of the values of v computed from the 40 h transmitter position estimate to find the distribution of pulse-compressed intensities. In this case, nothing is done to correct or account for equipment-caused Doppler effects; the Doppler effect is modeled as a signal with a slightly different carrier, but the pulse-compression algorithm is not adapted in any way. This approach is meant to quantify the effect of simply ignoring equipment motion.

The second approach involved a model that was used in Andrew et al. (2010) and that had been proposed earlier in Gondeck (1983). In this approach, a time-base mapping is computed between the time at the transmitter and the time at the receiver. The mapping describes the change in source-receiver distance R (measured in units of s, calculated by R/c_0, where $c_0 = 1500\,\mathrm{m\,s^{-1}}$) from the position estimates of a transmitter and receiver. The inverse mapping is computed, and samples at the appropriate times computed from the received signal using an FIR filter (as described in Glegg (1987)). This process is known as "de-Dopplerization". The de-Dopplerized signal is then pulse-compressed and the results are compared with those from the first approach. This approach does not make the simplifying assumption of constant velocity over the duration of the m-sequence.

B.3 Pulse-compressor performance: results

In figure 1, we show the intensity ($20\log_{10}(|z(t_i)|)$, where z is the complex pulse-compressed m-sequence that was sampled at times t_i for m-sequences with carriers at two frequencies near f_0. It can be seen that the side-lobes of the peak rise quickly for a small change in the carrier frequency of the m-sequence. In the bottom panel of figure 1 note that the peak intensity is also degraded. These observations will be referred to later in section B.4, where they will be further explored in calculation of the signal-to-noise ratio (SNR) of the received pulse-compressed signal. Figures 1 and 2 show results from the first approach described in the last section; the bottom panel of 2 also shows a comparison between the first and second approaches.

The top panel in figure 2 shows the peak pulse-compressed intensity for the frequencies considered. In all cases, the m-sequence was sampled at the ideal sample rate of $4f_0$. This is the degradation in intensity we may expect for the estimated transmitter speeds if we sample according to the design carrier frequency.

In the bottom panel are shown the cumulative density function (CDF) of intensity computed using the first and second approaches. A three dB down threshold is shown, this time as a vertical line. Speeds smaller than $0.325\,\mathrm{m\,s^{-1}}$ cause a degradation of less than the three dB threshold. 93.66 % of the projected velocity estimates fall below this $0.325\,\mathrm{m\,s^{-1}}$ threshold, as calculated from the first approach. Therefore 6.33 % of the velocities exceed this threshold. The result from the second approach is that 3.13 % of the data examined during the 40 h track exceed the three dB threshold.

B.4 A note on the calculation of SNR

In this section the calculation of SNR in the context of the pulse-compression used in PhilSea09 will be discussed. While exploring Doppler effects on pulse-compression, it seemed reasonable to consider SNR as another measure of the pulse-compressor's

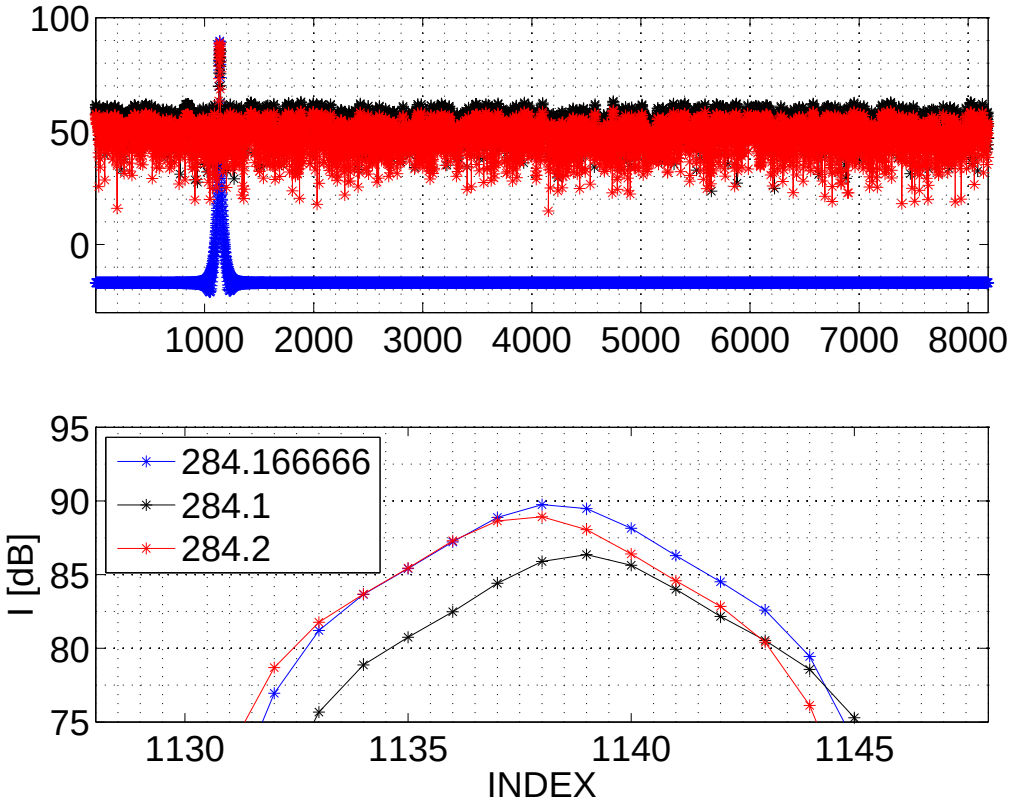

Figure 1: Pulse-compressor performance when the actual and assumed carrier frequencies of a signal differ slightly. Top panel: Intensity of pulse-compressed pure m-sequences with carrier frequencies at (blue) and near (black, red) the design carrier frequency of $f_0 = 284.166\,666\,\mathrm{Hz}$—but for which the sampling and pulse-compression have assumed the design signal. Notice that the side-lobes of the m-sequence spread across the output when the sequence is sampled at the design sample rate instead of at the ideal rate for a particular m-sequence. Bottom panel: same as above, focusing in on sample times near the peak intensity. Note that the peak intensity is degraded and time-shifted in addition to the raised side-lobes.

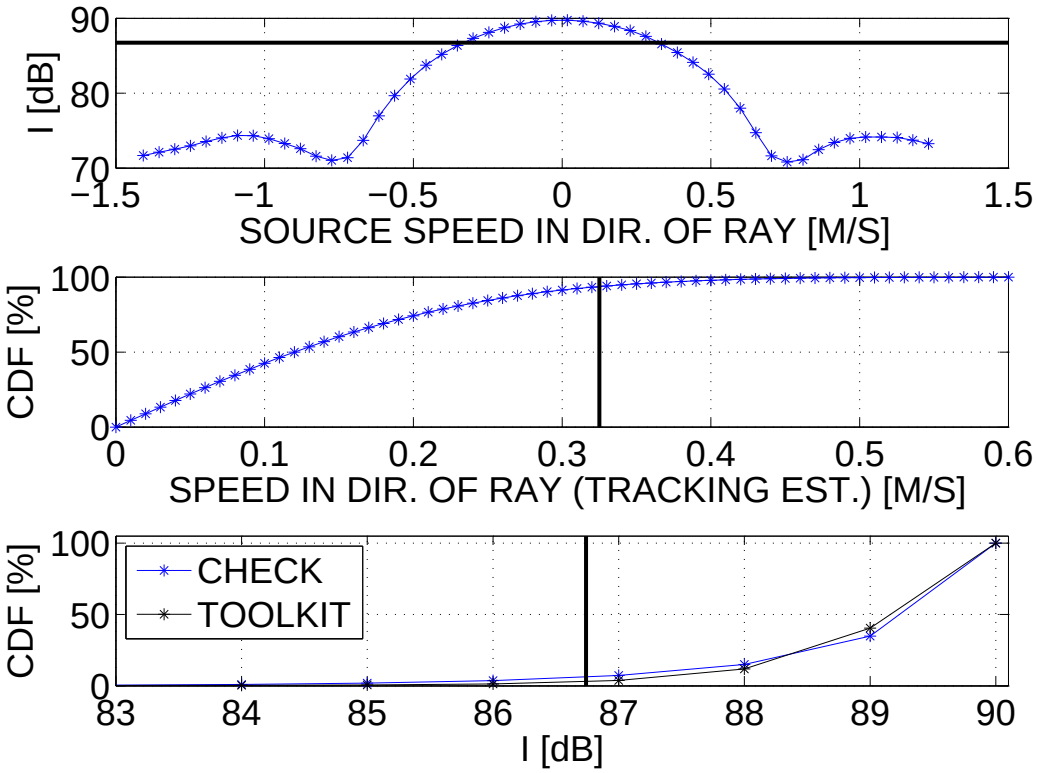

Figure 2: Predicted reduction in intensity due to degradation in pulse-compressor performance for source motion during PhilSea09. Top panel: peak intensity in decibel for m-sequences of carrier frequencies which are Doppler-shifted according to the source speed projection v, indicated on the abscissa. The horizontal line indicates a threshold of 3 dB down (arbitrarily chosen, for the purpose of illustration) from the case when the carrier frequency is equal to the design frequency, $f_0 = 284.166\,666$ Hz. Center panel: CDF of source speed v, computed from the 40 h-long estimate of source position. The vertical line shows the speed that corresponds to the 3 dB loss in peak intensity from the design frequency case. Bottom panel, the black curve labeled "CHECK" refers to the first approach described in the previous section. The blue curve labeled "TOOLKIT" refers to the result from second approach.

performance. It is shown in this section that one possible formulation of SNR overestimates the reduction in gain suffered due to Doppler effects, and a more appropriate formulation is presented.

The pulse-compression software calculated the SNR as the maximum value of the pulse-compressed intensity divided by the median level of intensity for a single pulse-compressed m-sequence. Although the signal in the water is present at all times during the transmission of an m-sequence, pulse-compression causes the energy to appear to arrive at particular times —to be concentrated in the pulse or pulses. At times not associated with large peaks in amplitude, there is a nearly constant background level (the pulse side-lobes). The median value is then this background level since times containing arrivals are far outnumbered by times at which no transmitted energy appears to arrive.

When the pulse compression algorithm is working well, this median level is close to the noise level, as will be shown for a real example. The complication to calculating SNR as was just described is that the median level changes with Doppler-compensation. Recall from figure 1 that when an m-sequence at a given carrier frequency is pulse-compressed assuming a slightly different carrier, the pulse-compression is affected in two ways: a decreased maximum intensity and increased side-lobes, and therefore an increased median value.

This median level could be thought of as the background ambient noise level, though one clue that this is not an accurate measure is that the ambient noise level should not change with Doppler-compensation. This would not be true if the ambient noise were dominated by a single source, such as a ship moving toward or away from the receiver. Noise that is not filtered out in the process of pulse-compression (that within the band of the transmitted signal) remains in the pulse-compressed signal. One would like to estimate that noise n, but the signal is in the water as well so we

cannot help but measure $s + n$ at that time. The only recourse is to measure the ambient noise level in the band at a time preceding or following the transmission, and to use this level as a proxy. The median level for one segment of pulse-compressed data taken before the transmission will be used to estimate n.

The top panel in figure 3 shows the median intensity for a single transmitted m-sequence, along with the median intensity of a segment of recorded ambient noise recorded less than an hour earlier. Both median values are plotted for various resample rates, which is equivalent to a Doppler search. It is apparent from the figure that the median value does approach the noise level that was recorded a few minutes before the transmitted m-sequence. Thus, when Doppler effects are not a concern, the measure seems to be accurate. Also, the level n from the segment preceding the transmission is not affected by Doppler-compensation.

The effect of measuring SNR using this median level is further shown in the bottom panel of figure 3. Also shown is the result of calculating SNR using a record immediately preceding reception of the transmitted signal, i.e. a time when only noise n is present. As was mentioned earlier, calculating SNR using the median level while the signal is in the water over-estimates the degradation in gain achieved by pulse-compression due to Doppler effects.

B.5 Doppler search

A final topic that will be addressed in this chapter is the idea of a Doppler search. During PhilSea09 the positions of the transmitter and receiver were tracked—but during one exercise performed as part of an experiment conducted the following year, the ship was allowed to drift toward the receiving array during transmissions. The transmitter position was not tracked during this exercise. At one point the during the drift the ship's velocity in the direction of the receiver became small, and it was noticed

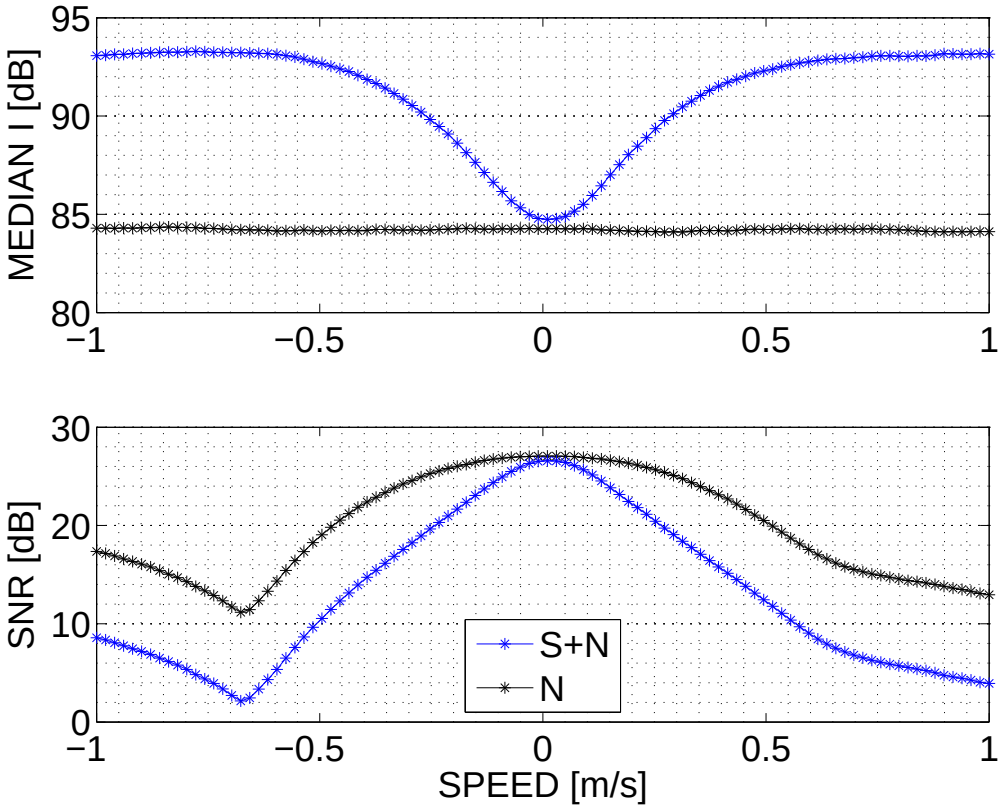

Figure 3: Comparison of estimates of SNR for various Doppler shifts using the median pulse-compressed intensity when the signal is in the water vs. using the pulse-compressed intensity from a time immediately preceding the acoustic transmission. Top panel: Median pulse-compressed intensity for a segment of data one m-sequence in length. The blue curve is the median value during transmission and the black curve is ambient noise recorded earlier in the same hour. Median intensity is plotted for various Doppler- compensations. Bottom panel: Two of the possible ways one might compute the SNR are shown here, at various Doppler compensations. The blue curve shows the SNR as computed using the median level during the transmission, while the black curve shows the SNR using the median level when our signal was not in the water. The SNR *appears* to fall much more quickly using the median level during transmission. The labels $S + N$ and N refer to the fact that the median level during transmissions contains both signal and noise.

that the SNR (as calculated using the median value of $s + n$) improved significantly during that time. This observation led to the idea of performing a Doppler search in order to maximize the SNR.

A Doppler search is done by simply resampling the acoustic pressure time-series at rates near the design sample rate, until a local maximum in SNR is found. The chirp-z transform (Rabiner et al., 1969) provides this capability. For example, we may resample a pure m-sequence at arbitrary sample rates corresponding to a range of source speeds and pulse-compress the resulting sequences. This is similar to what we've done in section B.2, except that instead of varying the carrier and sampling at the design rate, the signal recorded at the receiver was sampled at various rates.

The results of a Doppler search for an actual received m-sequence are shown in figures 4 and 5. Figure 4 shows the pulse-compressed intensity for various resamplings (corresponding to various transmitter speeds v) of the received signal. In this case the maximum pulse-compressed intensity is found at the design sample-rate, or for a negligible transmitter speed. Figure 5 shows the SNR for paths ID-3, ID+4, and ID-4, in panels A, B, and C, respectively, for another received m-sequence at various resample-rates. Notice that the best signal compression for energy arriving along a given path occurs at a frequency which may not be optimum for compression of energy taking another path. This is because energy taking different paths leaves the source at different angles; the projection of the source velocity vector onto the ray varies by arrival. The sign of the transmitter speed is the same for paths ID-3 and ID-4, as would be expected, since both paths leave the transmitter at a negative angle and the projection of the transmitter's velocity should be similar. Given that the transmitter motions in the vertical were on the order of the length of an m-sequence, and that this Doppler-search method resamples the whole sequence at a single rate, this observation was not guaranteed.

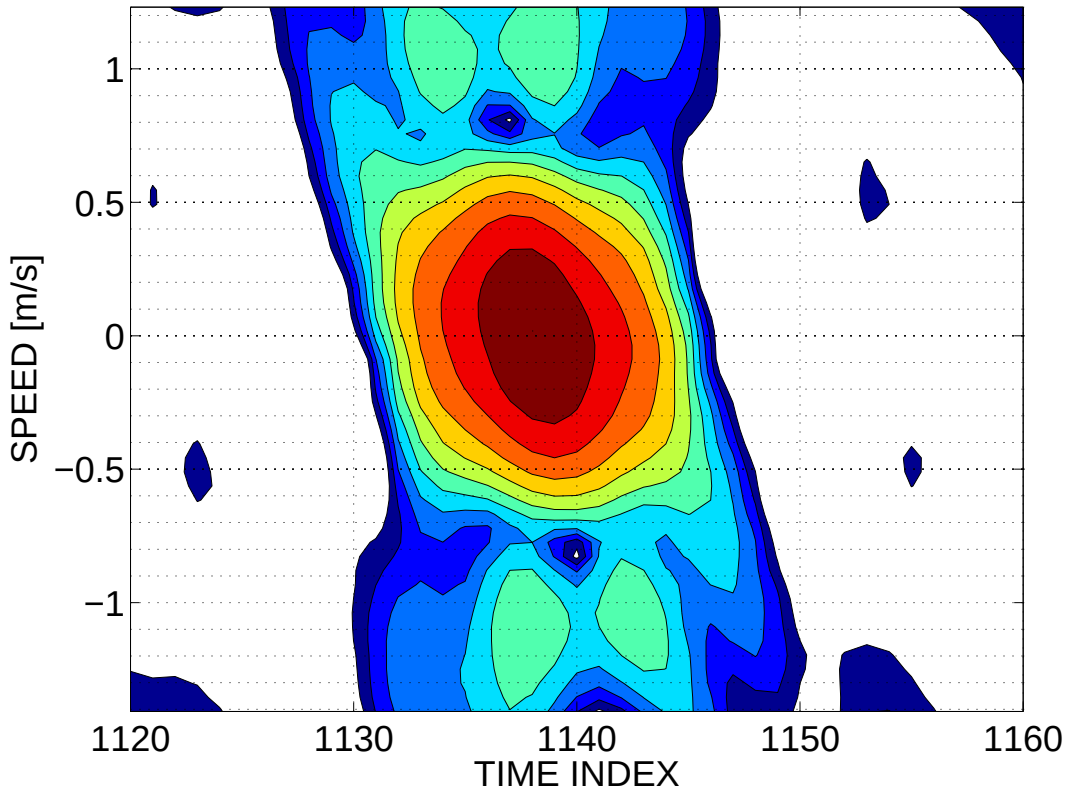

Figure 4: Shown is the pulse-compressed intensity of an m-sequence with the design carrier which has been resampled at various rates. As in figure 1, we see that the peak intensity and associated time vary with sample rate. Intensity contours of 3 dB are shown.

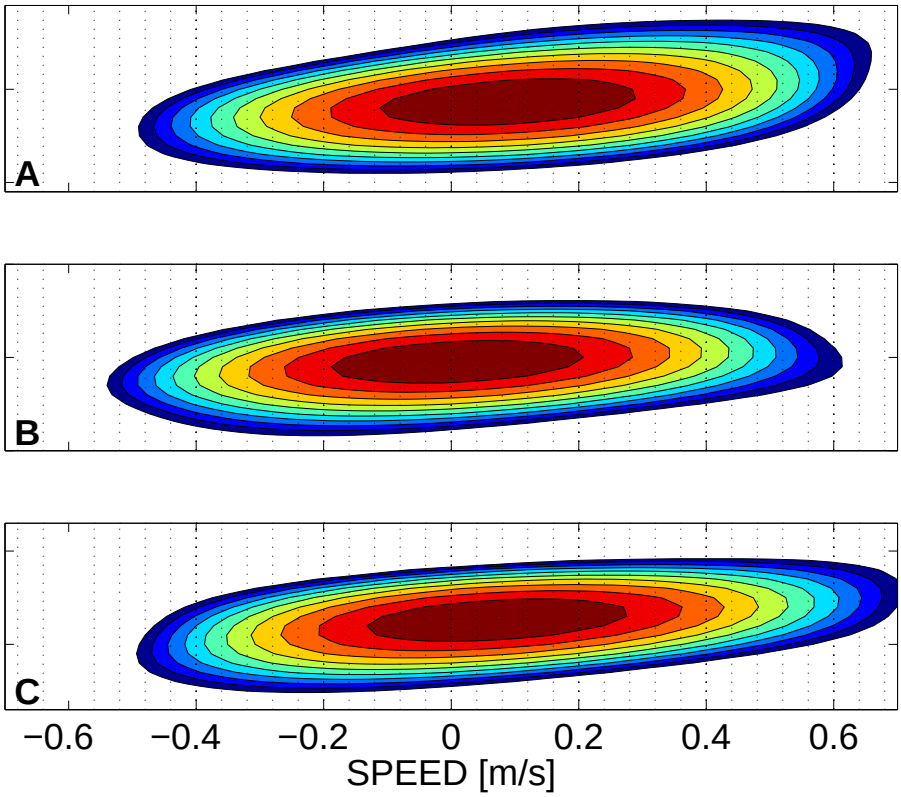

Figure 5: Shown here is the SNR for a single m-sequence reception computed using the median level during a time when our signal was not in the water, at various Doppler compensations. A reasonable requirement for a good measure of intensity is that the SNR be at least 10 dB above the ambient noise level. 1 dB contours are shown. The lowest contour 10 dB down from the peak value in order to explore how large a Doppler effect would be necessary to bring the signal strength below this required level.

A Doppler search as described above lumps together Doppler effects due to equipment motions with those imparted by the ocean medium. An idea about how large the degradation in pulse-compression due to motion of the ocean medium might be gotten by comparing the results of a Doppler search to those found using the second approach from section B.2. If the differences between the Doppler search and the second approach were noticeable, one would conclude that the ocean's effect was significant.

Time-series of intensity for paths ID-3, ID+4, and ID-4 were computed from an hour-long record from the 1550 m depth hydrophone with and without a Doppler search. The intensity of each arrival was maximized using a Doppler search, and the difference at each time between the Doppler-compensated and non-Doppler-compensated intensities was calculated.

Results are shown in figures 6 and 7. The transmitter speed v which maximized each individual arrival was saved for the three paths as well. The correlation function coefficient between the maximizing speed v for pairs of arrivals was also calculated, and is shown in figure 8.

It is apparent from the figures that a Doppler search doesn't cause much improvement in the pulse-compression for this case. The speeds v are seen to de-correlate after a length of time approximately equal to the duration of an m-sequence; this suggests that the equipment-caused Doppler effect is greater than that caused by the ocean for the hour examined here.

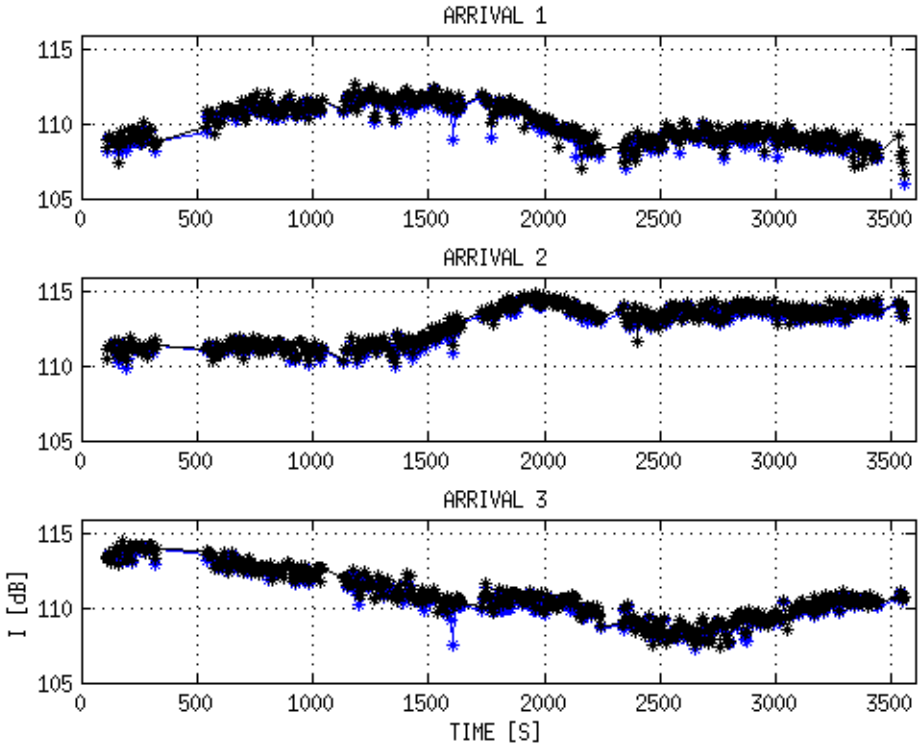

Figure 6: Intensity gain via Doppler-compensation. Top panel: blue curve is the maximum intensity of path ID-3, and the black curve is the Doppler-compensated maximum intensity. Paths ID+4 and ID-4 are shown in the middle and bottom panels, respectively.

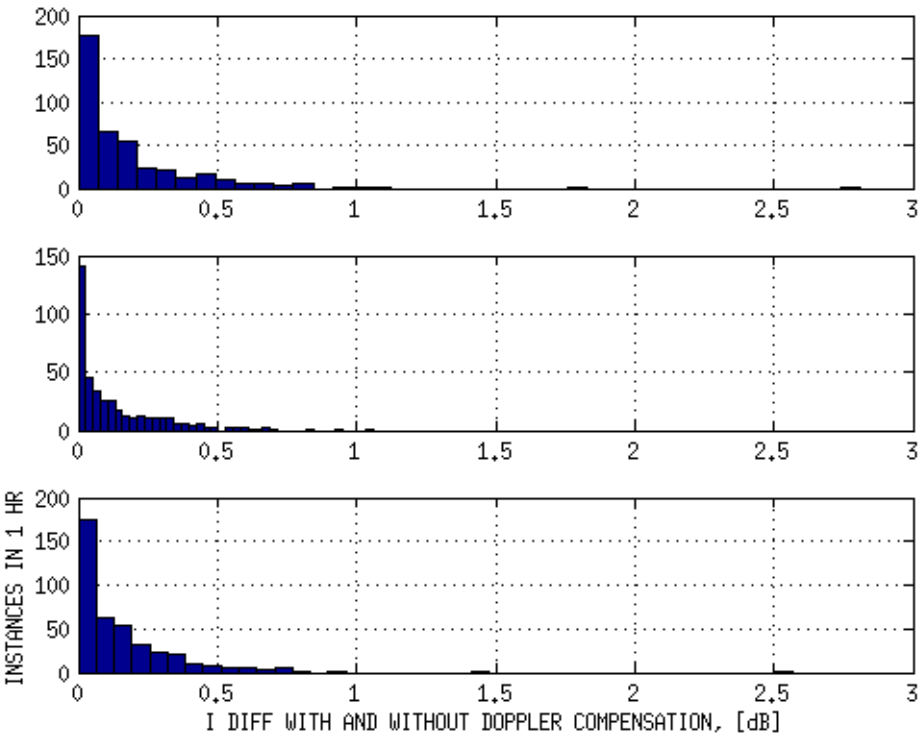

Figure 7: Shown in the top panel is the histogram of the difference between the time-series for path ID-3 with, and without, Doppler compensation. The center and bottom panels show the same for paths ID+4 and ID-4. In all cases, Doppler compensation was optimized for the particular arrival under consideration.

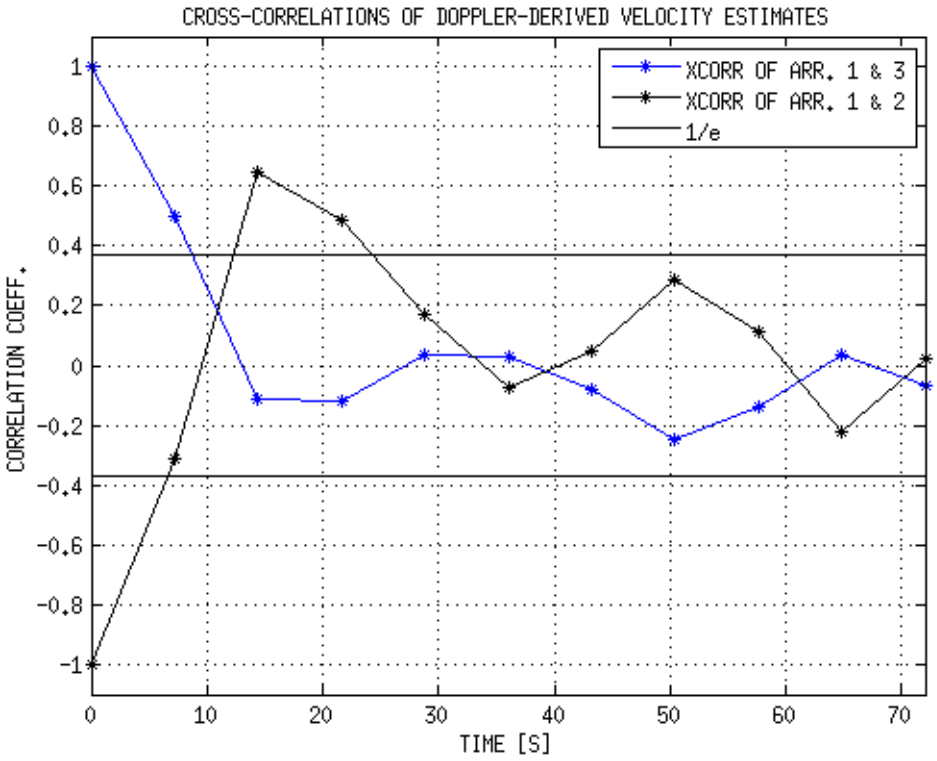

Figure 8: Shown is the correlation coefficient of velocities estimated via a Doppler search which optimized SNR by arrival. The correlation coefficient between two down-going arrivals (paths ID-3 and ID-4, which are arrivals 1 and 3 at this hydrophone depth) shows a positive value at zero lag, while the correlation coefficient between arrivals one and two has a negative value at zero lag. This indicates that most of the Doppler effect was caused by vertical motion. The fact that the estimated velocities de-correlate on a timescale similar to the period of the swell supports this idea. One might further conclude that any frequency shift caused by propagation through the ocean is outweighed by the motion of the source, since ocean properties affecting refracted-only propagation are not expected to change on such short timescales.

C Random internal wave model

This section introduces a Garrett-Munk (GM) internal-wave simulator that was developed by Frank S. Henyey and Stephen A. Reynolds of the APL/UW. The formalism comes from (Henyey et al., 1997) and the presentation follows (Winters and D'Asaro, 1997) (WD97). The general idea is to generate a displacement field by sampling an internal-wave spectral model over a uniform grid in horizontal wavenumber space, and assign a random amplitude to each vertical eigenfunction associated with that grid point. The random amplitudes have variance equal to the value of the spectrum times the area surrounding each grid point. (Throughout this discussion we will refer to the "element" rather than the more familiar "differential element" because in the implementation the element is, of course, finite. We will add up contributions from the whole wavenumber space within our bounds, leaving no spaces; the variance should therefore be in agreement with the chosen spectral model.) Finally, we compute the inverse Fourier transform to obtain the displacement field in 3-D.

We solve

$$\frac{\partial^2 \hat{\zeta}_{jk}}{\partial z^2} + k \frac{N^2(z) - \omega_{jk}^2}{\omega_{jk}^2 - \omega_i^2} \hat{\zeta}_{jk} = 0 \tag{1}$$

$$\hat{\zeta}_{jk}(0) = \hat{\zeta}_{jk}(-L_z) = 0 \tag{2}$$

for eigenfrequencies and vertical eigenfunctions, where $\hat{\zeta}_{jk}(z)$ are the vertical eigenfunctions, $N(z)$ is the buoyancy frequency, ω_{jk} the eigenfrequencies, ω_i the local inertial frequency, k the horizontal wavenumber, and j is the discrete eigenfunction number. The vertical eigenfunctions, or more colloquially, modes, are the modes that solve this equation instead of the WKB modes used by some internal-wave simulators.

In this case we will describe the internal-wave field with the GM spectrum, which

is horizontally isotropic. It was realized that this allows sampling in k and k_x, and would require only logarithmic sampling in k and the usual uniform spacing in k_x, thus admitting computation of a larger range of horizontal scales. The trade-off here is that we will only obtain the field in one horizontal direction–but for many propagation modeling problems in deep-water ocean acoustics, a 2-D approximation to a 3-D environment is appropriate.

The group speeds may be calculated by exploiting the Hellmann-Feynman theorem (Feynman, 1939)

$$v_g = \frac{\mathrm{d}\omega}{\mathrm{d}k} = \frac{(\omega^2 - \omega_i^2)^2}{k\omega} \left[(\omega^2 - \omega_i^2)^{-1} - \int |\hat{\zeta}_{jk}(z)|^2 \mathrm{d}z \right] \tag{3}$$

and are used in formulating the Jacobian of transformation to convert the GM spectrum from (ω, j) to (k, j) dependence. The GM spectrum $F_\zeta(\omega, j)$ is an angular average, so because each element subtends an angle $\mathrm{d}\theta$, we should include a factor of $(2\pi)^{-1}$ as we consider contributions from all horizontal directions. The displacement variance in frequency, mode number, and horizontal wavenumber associated with the element is then:

$$F_\zeta(\omega, j)\,\mathrm{d}\omega\,\mathrm{d}j\frac{\mathrm{d}\theta}{2\pi} = \frac{F_\zeta(\omega, j)\,\mathrm{d}\omega}{2\pi k\,\mathrm{d}k}\mathrm{d}j\,\mathrm{d}k_x\,\mathrm{d}k_y \tag{4}$$

$\mathrm{d}j$, the mode number increment is 1, but is left in for completeness. We count contributions only in the first quadrant, where k_x and k_y are both positive, taking advantage, again, of the horizontal symmetry. We include a pair of waves for each k_x, one from each x-direction, which accounts for the contribution to the variance due to the spectrum at negative k_x's. To account for the variance from the spectrum at negative k_y values, we double the size of the element in equation 4.

Our displacement field in terms of k_x is calculated as

$$\zeta(k_x, y = y_0, z; t) = \int e^{ik_y y} \sum_{j=1}^{M} \{G_- e^{-i\omega_{jk} t} + \cdots \\ G_+ e^{i\omega_{jk} t}\} \hat{\zeta}_{jk}(z)\, \mathrm{d}k_y \tag{5}$$

where we have set $y = y_0$ to indicate that we will compute a range-depth slice of the displacement field. The expected value of the squared complex random amplitudes, G_+ and G_- sums to the variance for the element, or the element's area times the spectral level:

$$\left\langle G_+^2 \right\rangle + \left\langle G_-^2 \right\rangle = \frac{F(\omega, j)\, v_g}{\pi k} \mathrm{d}j\, \mathrm{d}k_x \mathrm{d}k_y \tag{6}$$

Time is a parameter in equation 5; the displacement field may be evolved in time by recomputing the field at a later time t. The displacement is then the 1-D inverse Fourier transfom of 5, where x and k_x are transform pairs

$$\zeta(x, y = y_0, z; t) = \mathcal{F}^{-1} \left\{ \zeta(k_x, y = y_0, z; t) \right\} \tag{7}$$

We will lastly give the details of the GM vertical displacement spectrum that are pertinent to our discussion. The vertical mode normalization is given by

$$\int_{-L_z}^{0} \left(N^2 - \omega_i^2 \right) \hat{\zeta}_{j,k}(z) \hat{\zeta}_{j',k}(z)\, \mathrm{d}z = \delta_{jj'} \tag{8}$$

The GM spectrum of vertical displacement is given by

$$F_\zeta(\omega, j) = b E_{GM} \frac{N_0 b}{N(z)} \frac{\omega^2 - \omega_i^2}{\omega^2} H(j) B(\omega) \tag{9}$$

where

$$H(j) = \frac{H_0}{j^2 + j_*^2} \tag{10}$$

and

$$B(\omega) = \frac{2}{\pi}\frac{\omega_i}{\omega}\frac{1}{\sqrt{\omega^2 - \omega_i^2}} \tag{11}$$

H_0 normalizes to unity the summation over modes of $H(j)$ and $B(\omega)$ integrates to 1 over the frequencies where internal waves exist, ω_i to N. j_* is the modal bandwidth; in the work presented in this paper, a value of $j_* = 3$ has been used, as was given in GM81.

The variance given by GM81 (Munk, 1981) was

$$\left\langle \zeta^2 \right\rangle = \int \mathrm{d}\omega \sum_{j=1}^{M} F_{\zeta\zeta}(\omega, j) = \frac{1}{2} b E_{GM} N_0 b N(z)^{-1} \tag{12}$$

but here we calculate $N_0 b$ from the background buoyancy frequency $N_0 b = \int N(z)\,\mathrm{d}z$; the product bE_{GM} is then adjusted accordingly to preserve the variance.

The environment is computed on a domain of 1 Mm with 8192 points $\approx$ 122 m range-step. The water depth is 5505 m with 5506 points giving a sample at each meter of depth.

D PSD/temporal autocorrelation function: TD MCPE

D.1 Results

Predictions of the PSD for ID-3, ID+4, ID-4, and ID+5 for the hydrophone depths used in PhilSea09 are shown in figure 9. The plots show only a subset of frequencies around a peak in the spectrum to make visible the structure in depth and time. The spectral peak around a frequency of 1 cpd appears in the predicted PSD for all paths.

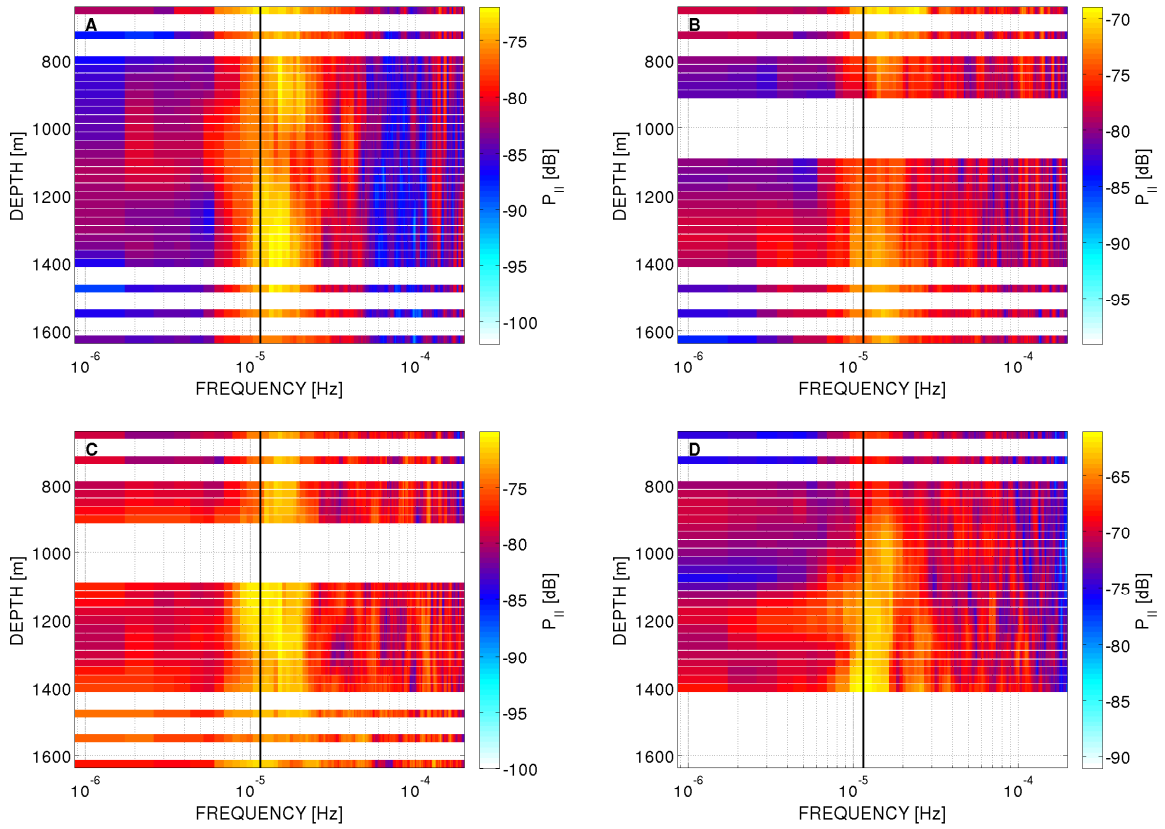

Figure 9: PSD predictions for a subset of frequencies around 1 cpd at the hydrophone depths used in PhilSea09.

Predictions of the autocorrelation function $R_{II}(\tau)$ (normalized to a maximum

value of one at zero lag) for the four paths appear in figure 10. From these predictions, the "correlation time", defined as the minimum lag for which the correlation falls below a value of $1/e$, is computed; this quantity is shown in figure 11. The predicted correlation times for paths ID-3, ID+4, and ID-4 are all around 22 min, while the correlation time for path ID+5 is somewhat longer and more variable in depth.

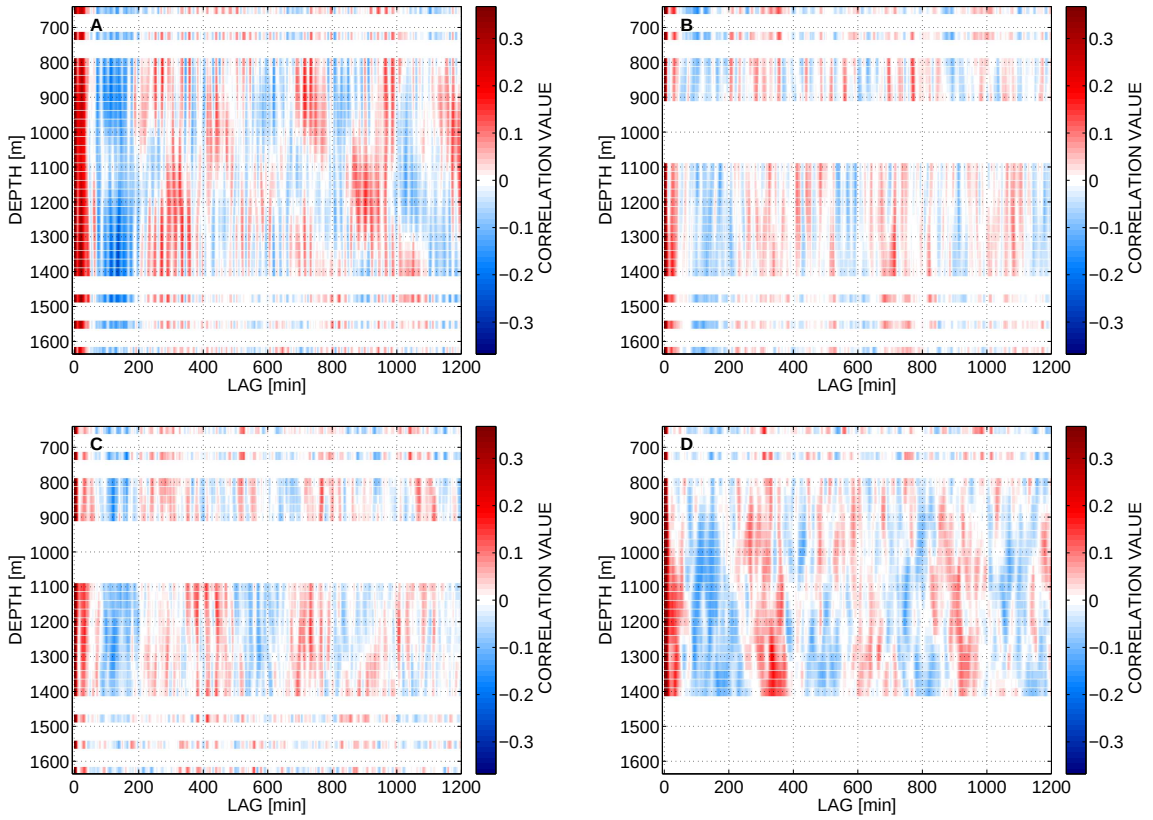

Figure 10: Autocorrelation function predictions for the hydrophone depths used in PhilSea09. The autocorrelation function is normalized to a maximum value of one at zero lag. The color-scale shows correlations from $\pm 1/e$ to make visible the structure in depth and time.

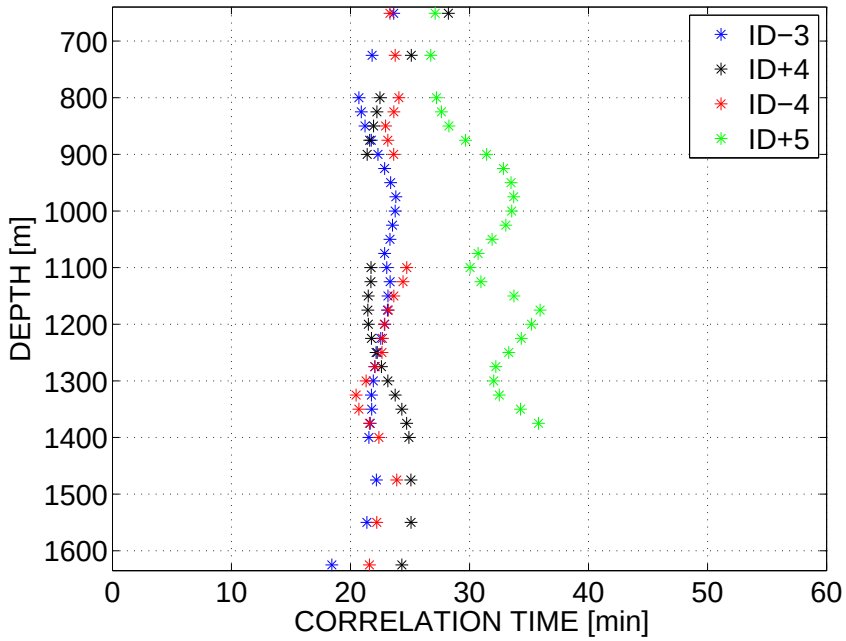

Figure 11: Shown are the predictions of the minimum lag for which the normalized autocorrelation function falls below a value of $1/e$, or the "correlation time", for all paths at PhilSea09 hydrophone depths.

E AuxiliaryData

This appendix contains some of the shipboard measurements taken during the APL-UW's transmission cruise. Bathymetry was measured with a multi-beam sonar, and is shown along the SS107–DVLA transect in figure 12. Photosynthetically available radiation (PAR) and long- and short-wave radiation are shown in figure 13. Figure 14 shows the measured precipitation. Figure 15 shows the air and surface water temperature, along with the relative humidity. Finally, the wind speed and direction are shown in figure 16. Water velocities near the surface were also measured during the cruise using an ADCP with frequencies of 75 kHz and 150 kHz, but are not shown here.

Figure 12 *(facing page)*: Bathymetry measured on the propagation track between SS107 and the DVLA during PhilSea09. The triangle symbol that is located between the two circle symbols is the position of SS107; the two circles are the positions of the bottom-mounted transponders that were used to track the source position during transmissions. The triangle symbol in the bottom half of the figure is the position of the DVLA.

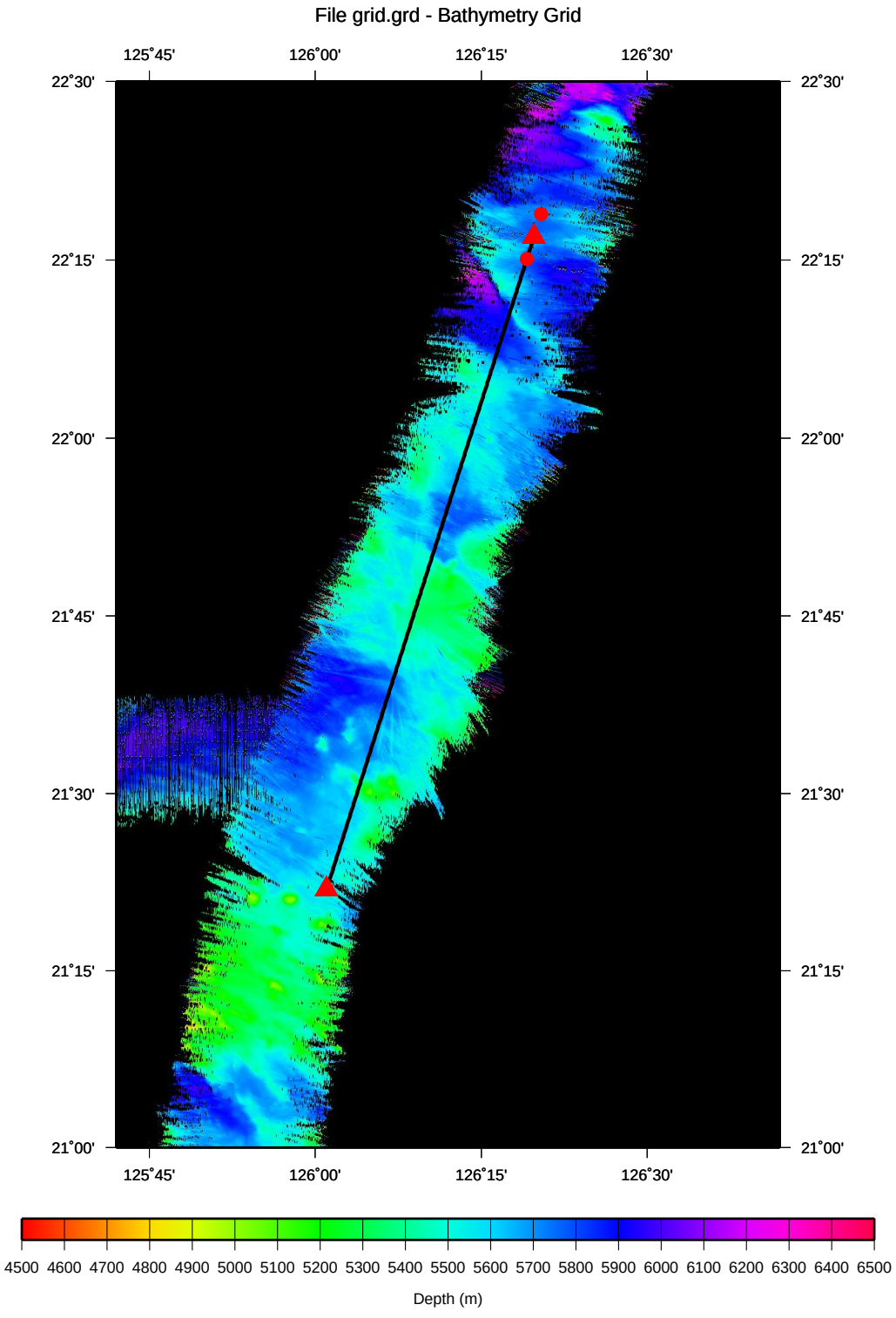
File grid.grd - Bathymetry Grid
125˚45'
126˚00'
126˚15'
126˚30'
22˚30'
22˚15'
22˚00'
21˚45'
21˚30'
21˚15'
21˚00'
4500 4600 4700 4800 4900 5000 5100 5200 5300 5400 5500 5600 5700 5800 5900 6000 6100 6200 6300 6400 6500
Depth (m)

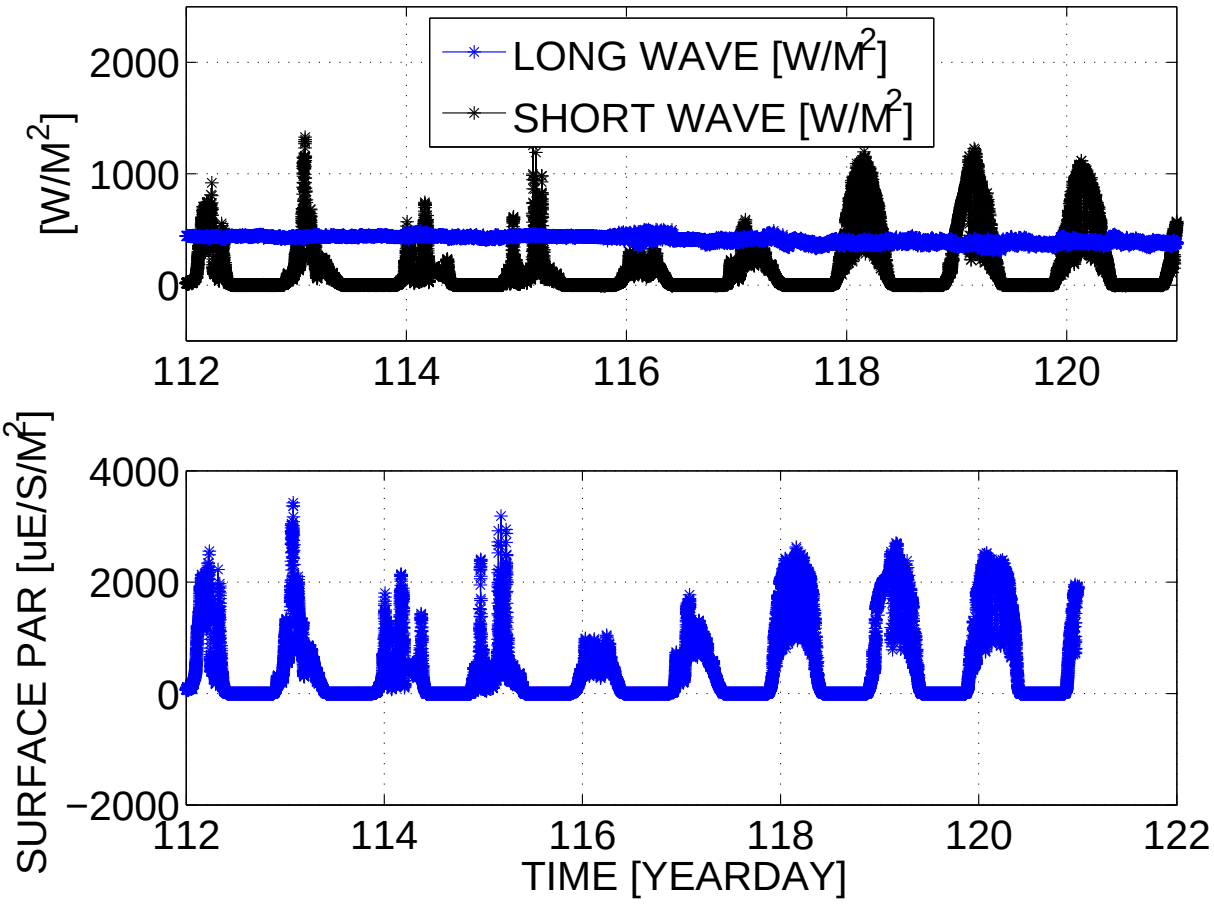

Figure 13: Shown in the top panel are the long- and short-wave radiation measured during the APL/UW signal transmission cruise. The bottom panel shows the surface photosynthetically available radiation measured during the same cruise.

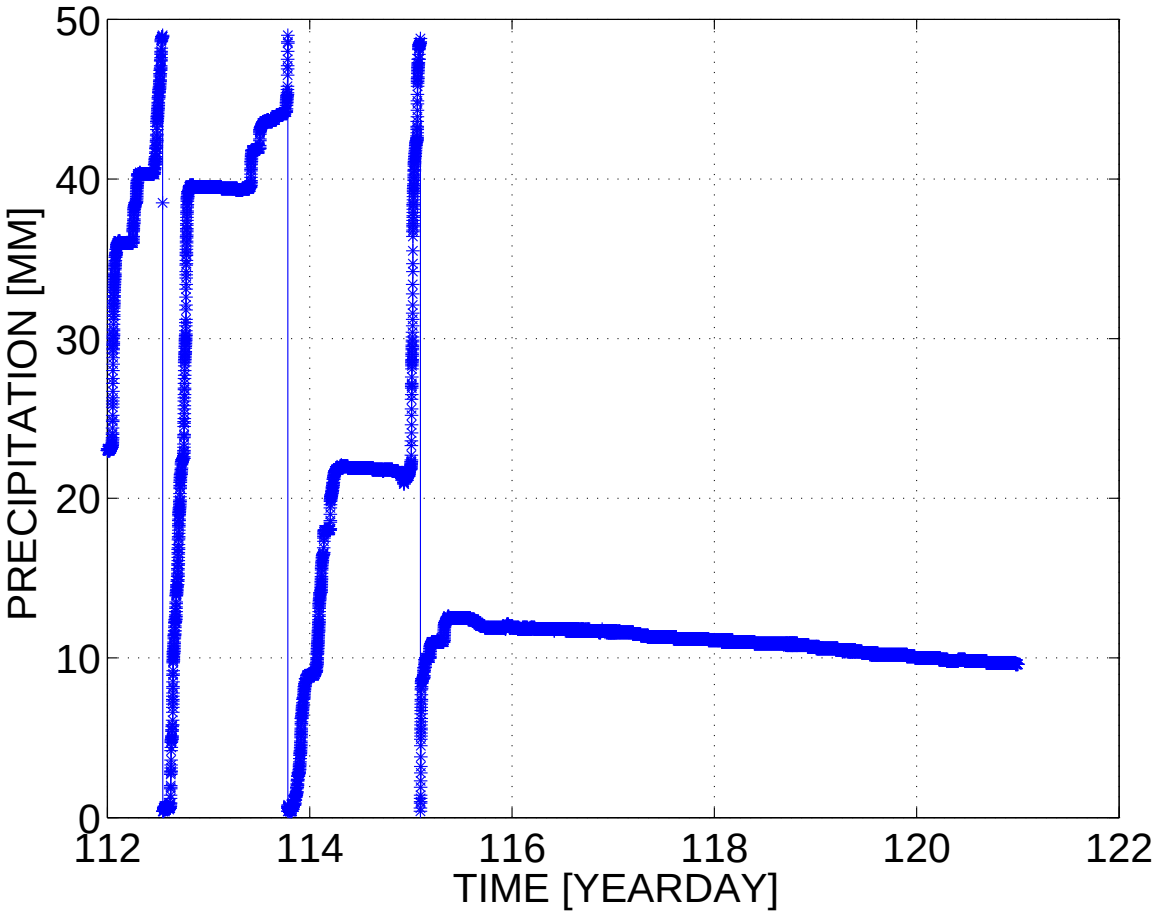

Figure 14: The precipitation measured during the APL/UW signal transmission cruise.

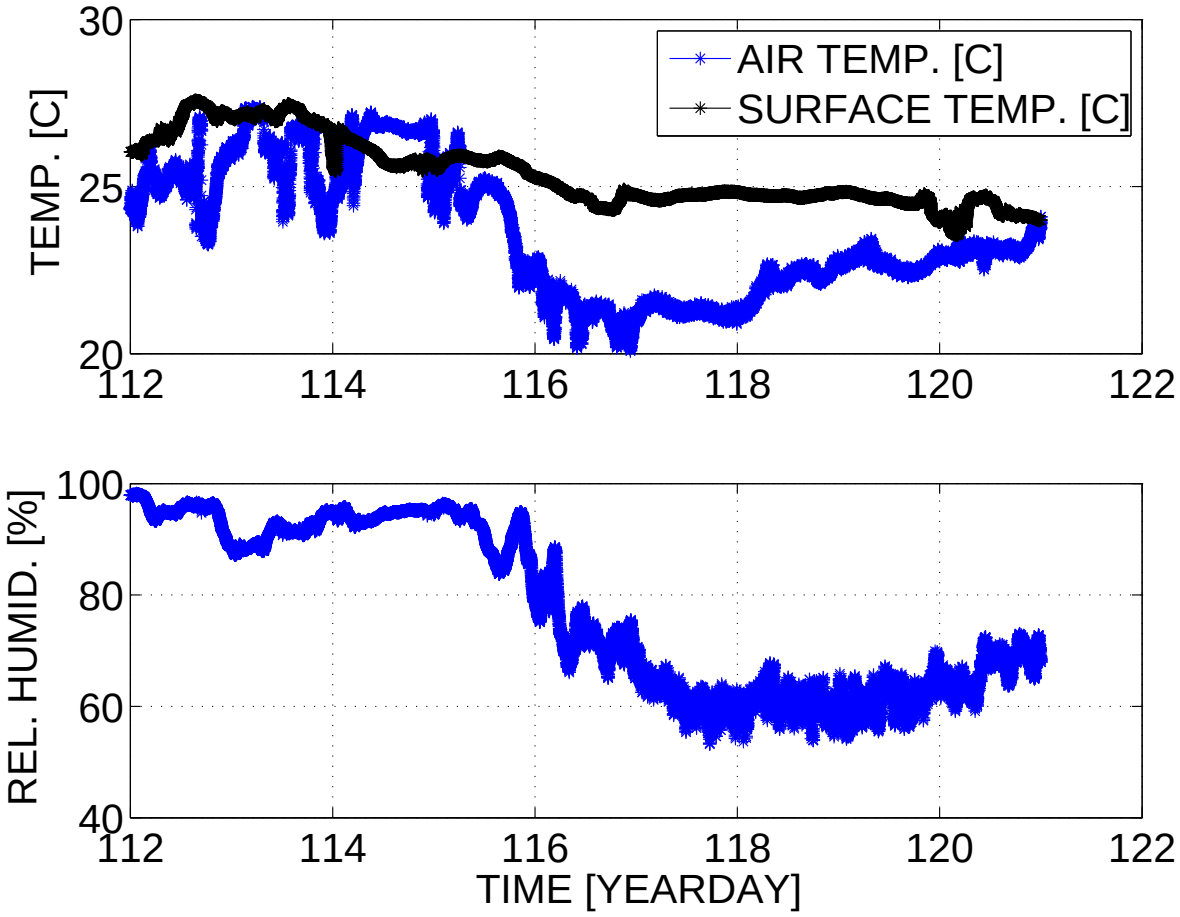

Figure 15: The air and surface water temperature (top panel) and humidity (bottom panel) measured during the APL/UW signal transmission cruise.

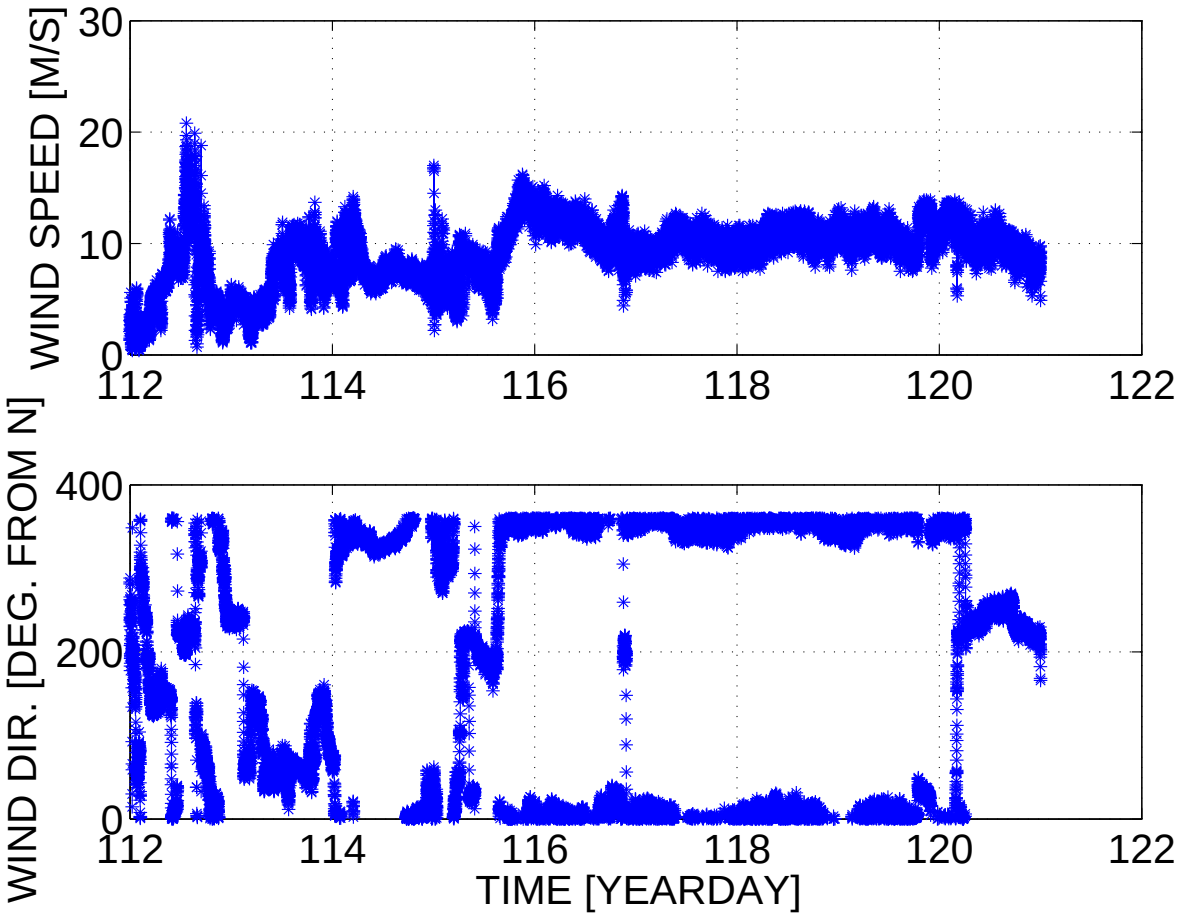

Figure 16: The wind speed (top panel) and direction (bottom panel) measured during the APL/UW signal transmission cruise. The measurement is not made near the ocean surface, but instead at some elevated position—possibly above the ship's wheelhouse. A correction must be applied in order to estimate the wind speed at the ocean surface.